Doctoral Dissertation
博士論文（要約）

Scanning Tunneling Microscopy and Spectroscopy Studies of Graphene Zigzag Edges Fabricated by Hydrogen Plasma Etching

（水素プラズマエッチングで作成したグラフェンジグザグ端の
走査トンネル顕微法および分光法による研究）

A Dissertation Submitted for the Degree of Doctor of Philosophy

July 2020
令和2年７月博士（理学）申請

Department of Physics, Graduate School of Science,
University of Tokyo
東京大学大学院理学系研究科
物理学専攻

André E. B. Amend
アメンド　アンドレ　オイゲン　ベンハード

Abstract

The unique physical properties of the two-dimensional carbon crystal graphene may lead to technological advancements in many fields, thus they garner attention beyond the scientific community from industry and public. Since graphene is predicted to host magnetic edge states, while supporting long spin coherence lengths, graphene based spintronic devices may enable a revolution in computer performance. Such spin-polarization on graphene nanoribbons with zigzag edges (zGNR) is theoretically well established, but there is a lack of clear experimental evidence. The aim of this work is to clarify the existence of spin-splitted edge states and thereby contribute to the development of novel spintronic devices by understanding graphene zigzag edge states and the necessary conditions for them to become spin-polarized.

In this work, graphite and epitaxial graphene samples on the C-terminated (SiC(0001)) and the Si-terminated ($\mathrm{SiC}(000\bar{1})$) faces of SiC were anisotropically etched by hydrogen plasma, creating hexagonal nanopits with monolayer depth. These edges, which are aligned in zigzag directions and for which termination by hydrogen is ensured, were studied by scanning tunneling microscopy and spectroscopy. In addition to nanopits, the etching was found to produce quasi-free-standing graphene on SiC(0001). On the surface of graphite and epitaxial graphene on $\mathrm{SiC}(000\bar{1})$, the edges were found to host localized electronic zigzag edge states. Thus, zGNRs synthesized in between two hexagonal nanopits were investigated. On graphite, a splitting on the order of 50 meV of the edge state LDOS peak was observed as well as some additional peak structures. The splitting only occurred on parallel zGNRs narrower than 23 nm and is inversely proportional to the nanoribbon width. Since this is in good agreement with a theoretical calculation for edge state spin-splitting considering the interaction, with a graphene substrate, these results are strong experimental indications of the elusive spin-polarized edge state. At zGNRs on $\mathrm{SiC}(000\bar{1})$, with relatively strong doping, we observed a similar, but slightly different edge state splitting. In accordance with the increased interlayer distance by 3%, and edge state peak width by 70 mV compared to etched graphite, we observed a larger spin-splitting by as much as 220 meV, while some splitting results overlapped. The wider variations of the edge state splitting than on graphite surface we observed, which is probably caused by doping and morphology variations, may be indicative of the theoretically predicted transitions among different magnetic edge states.

These findings conclusively show that zigzag edge states on graphene nanoribbons can become spin-polarized. Furthermore, they show that magnetized states can be modified or prevented by substrate influence. Our experimental results may stimulate further theoretical work, and are an important step towards realizing novel spintronic devices.

Contents

Chapter 1

Introduction

1.1 Graphene

1.1.1 History of graphene

Graphene is a sheet of carbon atoms that form a two-dimensional crystal with a honeycomb lattice structure. It consists purely of carbon, which is an element with a high degree of versatility. Its four valence electrons let it form a great number of different compounds and, famously, it is the building block of life as we know it. Versatility is also a feature found among its allotropes, from insulating and transparent diamond to opaque graphite. Due to their differences it often took a long time to understand that they are made-up from the same element. A. Lavoisier discovered in 1772 that diamond and charcoal consist of the same element and gave it the name carbon. Soon thereafter, at the end of the decade in 1779, C. W. Scheele found that graphite is another allotrope of carbon. However, about a century passed until filaments consisting of carbon were reported in 1889 by T. Hughes and C. Chambers, which have been only identified as carbon nanotubes by L. Radushkevich and V. Lukyanovich as recently as 1952 [1].

After that, it took almost four decades until broad scientific interest in carbon nanotubes was kindled following the publication of S. Iijima's observation of them in 1991 [2]. Fullerenes were discovered more recently in 1985 by R. Curl, H. Kroto and R. Smalley [3] for which they were later awarded the Nobel Prize in chemistry. Graphite, carbon nanotubes and fullerenes are all based on carbon atoms that are arranged in a hexagonal lattice, which is either stacked, rolled, or curled into a ball, respectively (an exception exists in the case of fullerenes, where some hexagons are replaced by pentagons). Conceptually, the most basic form of this arrangement is a single hexagonal lattice sheet that is now called graphene. The electronic band structure of graphene was already calculated as early as 1947 by P. Wallace [4]. However, strong general interest peaked more than five decades later, after it was isolated and identified in a laboratory in 2004 by A. Geim and K. Novoselov via mechanical exfoliation of graphite, the 'scotch tape' method [5]. For this achievement they were awarded a Nobel Prize, too, this time in physics. They found that despite having the thickness of only a single atom, a sheet of graphene is stable even in atmospheric conditions, and can be exfoliated from a stack of graphene layers. Today, these key discoveries over the course of the last thirty-five years have firmly anchored graphene and the carbon materials based on it in the scientific mainstream [2, 3, 5].

1.1.2 Graphene nanoribbons with zigzag edges

Graphene possesses many spectacular electronic and mechanical properties. These include ballistic electronic charge transport and a higher charge mobility than silicon, the half-integer quantum hall effect [5–8], a higher tensile strength than steel and being stable at atmospheric conditions despite consisting of only a single atomic layer, to name a few examples. The extraordinary qualities of graphene have inspired many to conceive of possible applications in future technologies. One of these qualities, that is interesting from both a scientific and an application perspective is the electronic edge state that appears at graphene zigzag-type edges.

The hexagonal lattice of graphene contains two triangular sublattices, where each neighboring atom belongs to a different one. At lower energies the electronic states on graphene possess independent solutions for the electronic states on the sites of the two sublattices, giving rise to the pseudo spin degree of freedom [9]. At graphene edges, depending on edge direction, the atoms near the edge can belong exclusively to one of the two sublattices (zigzag edges) or in equal parts to both sublattices (armchair edges). In the case of zigzag edges, the imbalance of atomic orbitals on the two sublattices was predicted theoretically to rise to localized electronic states with exponential decay lengths within 2 nm, that do not occur on armchair edges [10]. This prediction was experimentally confirmed by scanning tunneling microscopy and spectroscopy (STM/STS) measurements [11–13]. Furthermore, these localized states are theoretically confined on the majority sublattice [9, 14].

The high density of states that exists at the Fermi energy due to zigzag edge states may give rise to magnetic ordering [10]. This has not been found on single edges where it is too unstable, but on graphene nanoribbons with parallel zigzag edges (zGNR) the interaction of different edge states is predicted to stabilize spin-polarization of the edge states [15, 16]. If two zigzag edges terminate on different sublattices, the edge states occupy different sublattices as well and can interpenetrate. For this, the direction of the edges is crucial. Edge states on both sublattices occur on parallel zGNRs, as is shown in Fig. 1.1(a). Inside the nanoribbon, the local density of states (LDOS) from the two edge states on different sublattices are overlapping, since they occupy different sites, enhancing the magnetic interaction between the two edge states. Theoretically, the most stable spin configuration is a ferromagnetic alignment of spins along each edge state, and an anti-ferromagnetic alignment between the two edges, as is shown in (b).

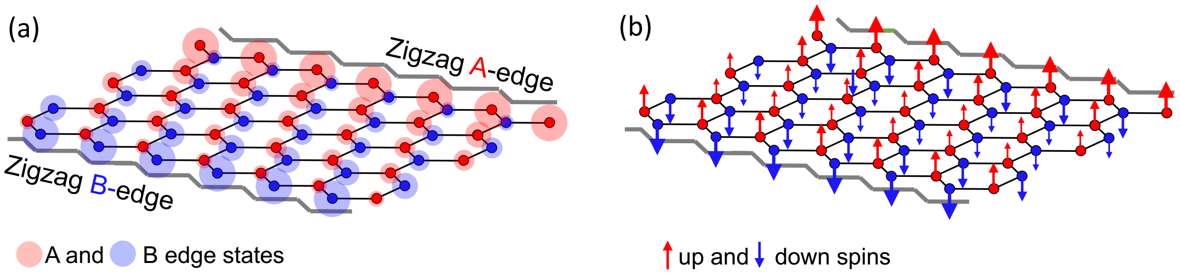

Figure 1.1: Schematic of a zigzag graphene nanoribbon with A- and B-sublattice atoms in red and blue, respectively. Cartoon of edge state (a) LDOS intensity and (b) magnetic moments on the atomic sites. Circle/arrow size is proportional to LDOS/magnetization at each atom.

The magnetic moments on the edge sublattices extend across the zGNR and increase somewhat on the opposite edge, as it is stabilized by the stronger magnetic interaction with the opposite edge state.

This polarized state is interesting from both a scientific and an application perspective. Since these spin-polarized zGNRs are predicted to become half-metallic [17, 18], and since bulk graphene supports long spin coherence lengths, such zGNRs may enable the development of graphene-based spintronic devices, that could lead to revolutionary improvements in computer performance [19, 20]. However, while the spin-polarization is theoretically well-established, the experimental results so far have been inconclusive. Experimental difficulties arise due to the nano-scale at which the edge states occur, which complicates both the measurement and the preparation of atomically precise edges with controlled terminations. Furthermore, the edge states are expected to be changed by the substrate influence, but different experimental results are sometimes conflicting on what effect the substrate has [21–23]. Experiments on graphene edge states have been constrained by the difficulties and limitations to obtain nanoribbons with controlled, atomically precise zigzag edges.

A promising avenue to fabricate zigzag edges is by chemical reactions, particularly, by anisotropic hydrogen (H-) plasma etching. With this technique, graphene is etched layer-by-layer, and hexagonal nanopits with straight zigzag edges are created [24–28], which are terminated by one hydrogen atom per edge atom [29]. In this work, we use H-plasma etching to create hexagonal nanopits with zGNRs between them on graphite, and on the epitaxial graphene on the C-face and Si-face of SiC.

1.2 Motivation

The question whether graphene zigzag edges can become spin-polarized has not been conclusively answered so far. In the case that this can be answered in the affirmative, spin-polarized edge states introduce magnetic order in usually non-magnetic carbon materials. This is of both scientific and practical interest, *e.g.*, for potential application in novel spintronic devices.

Although spin-polarization is theoretically well-established to occur on zigzag graphene nanoribbons, previous experimental studies, for several reasons, have not yielded results that allow reaching a firm conclusion about its existence. In some of these previous studies, the edge shape or termination could not be controlled. This makes it doubtful whether the samples host clean zigzag edge states [21, 23] that can support magnetic order [30]. Some studies used a bottom-up nanoribbon fabrication method to fabricate precise nanoribbons with zigzag edges, which only yielded nanoribbons of one certain width [22]. Unfortunately, this prevents the study of expected width-dependent features. Also, exponential decay of the edge state into the ribbon center, which is an important fingerprint of the edge electronic state, is not reported in this study. Another factor that seems to play an important role for spin-polarized edge states is the interaction with the substrate [18, 31]. In some experimental studies, influence by the substrate modified the edge state results [22] and inconsistent and uncertain sample interactions cast doubts on other results [21, 23]. The influence of the substrate is of particular importance with view to potential technical applications of graphene nanoribbons.

In this work, we tried to avoid the difficulties and limitations of other sample fabrication methods by using an anisotropic etching technique to create graphene zigzag nanoribbons on graphite. This is a well-known substrate, whose interaction with a graphene nanoribbon above it and the magnitude of the sublattice symmetry breaking are both well known and uniformly realized. In addition, we fabricated graphene nanoribbons on epitaxial graphene on the C-face of SiC, where we may expect the variation of the substrate interaction and sublattice symmetry breaking caused by the variation of rotation angle between the nanoribbon and the substrate graphene. By probing different systems, substrate dependent effects will be uncovered, which is important to understand in order to design devices that make use of the exotic properties of graphene nanoribbons. Analyzing the properties of edge states on graphene nanoribbons and proving the existence or absence of spin-polarized edge states in the examined systems provides important experimental evidence for this fascinating phenomenon that remained elusive for so long. Furthermore, conclusive results of graphene zigzag edge states and the necessary conditions for them to become spin-polarized can stimulate further work that may pave a way towards applications, such as novel spintronic devices.

1.3 Outline of the Thesis

In Chapter 2, the theoretically and experimentally established properties known from previous works on graphene are presented. Specifically, the edge states on graphene, and possible spin-polarization of the edge states are discussed. Furthermore, the anisotropic hydrogen plasma etching technique by which graphene zigzag edges can be fabricated is introduced. In Chapter 3, we explain the specific hydrogen plasma etching technique, that is used in this work, as well as the individual etching conditions used to prepare different samples. We also describe the low-temperature STM/STS measurement technique that was mainly used for the experiments in this work. In Chapter 4, we show the measurement results obtained on the etched surface of graphite. The results on bulk terraces, on single edges and on graphene nanoribbons that are formed by two etched edges are discussed. In Chapter 5, we show the results of etching epitaxial few-layer graphene on SiC($000\bar{1}$). We discuss the effects of etching on this sample, including the properties on bulk terraces. The results on single edges and on nanoribbons are discussed as well. In Chapter 6, our results of the effects of hydrogen etching on epitaxial monolayer graphene on SiC(0001) are shown. The effects of etching on the bulk terrace properties of this sample, and the fabricated nanopits are discussed. The main experimental findings of this work and the conclusions are presented in Chapter 7.

Chapter 2

Theoretical and Experimental Knowledge of Graphene

The following Section 2.1 introduces some of the properties of graphene, as well as the specific systems that we studied, epitaxial graphene on SiC($000\bar{1}$) and SiC(0001) and graphite. The main interest of this work are electronic zigzag edge states, some background on them is given in Section 2.2. Afterwards, in Section 2.3, the possibility of magnetism on graphene nanoribbons with zigzag edges is discussed. Finally, Section 2.4 introduces the anisotropic hydrogen plasma etching techniques, that is used to prepare the samples in this work.

2.1 Properties of Graphene

2.1.1 Physical properties of graphene

In the graphene lattice, three of the four valence electrons of each carbon atom are sp^2 hybridized and form covalent σ-bonds with three neighboring carbon atoms. Due to the repulsion between the electrons the three sp^2 orbits arrange themselves in a plane with an angle of 120° between them to maximize the inter-orbit distance at each atomic site. Thus, a flat hexagonal lattice is formed with the shortest distance between covalently bonded carbon atoms being 0.142 nm. The fourth valence electron of each carbon atom occupies a p-orbital that is perpendicular to the plane of the covalent bonds and does not interact with them. The interaction between p-orbitals on different carbon atoms forms π bonds which dominate the electronic properties of graphene at lower-energies.

The Bravais lattice that describes the honeycomb lattice of graphene is a two-dimensional triangular lattice whose unit cell contains two atoms. These are commonly called A and B atoms and form triangular A and B sublattices, respectively. A model graphene lattice with A/B atoms differentiated by color is shown in Fig. 2.1(a). When multiple layers of graphene are stacked on top of each other, their atoms remain sp^2 hybridized in their respective layers and the layers are coupled by van der Waals forces. This interlayer interaction is much weaker than the in-plane covalent bonding, therefore it is possible to exfoliate graphene sheets intact. When two graphene layers are stacked commensurately, which is schematically shown in Fig. 2.1(b), then all atoms in one

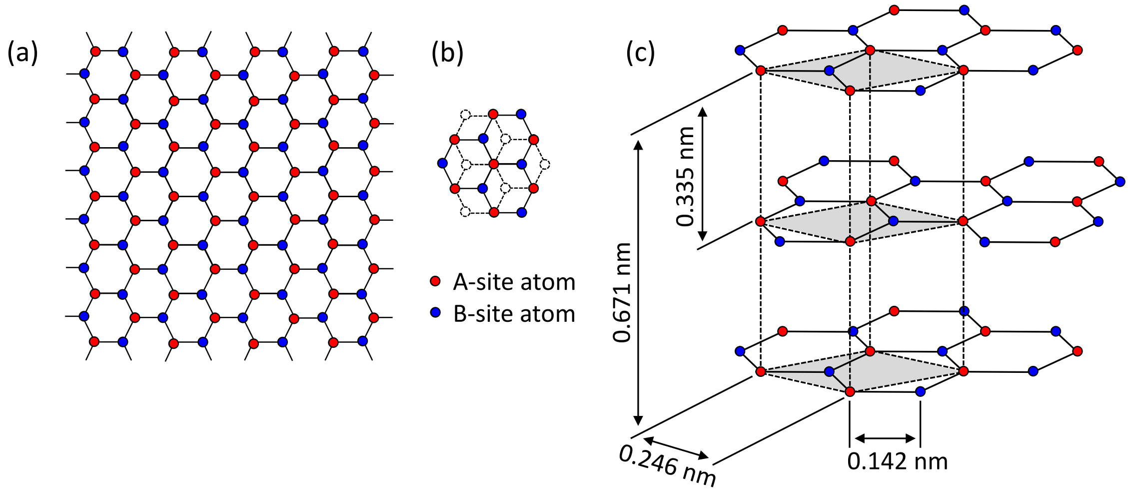

Figure 2.1: Schematic view of Graphene. Carbon atoms on the A/B sublattice are represented as red/blue dots and covalent bonds shown by black lines. (a) hexagonal graphene lattice. (b) top view of AB stacked bilayer graphene (no color in second layer). (c) three graphene layers with AB stacking.

sublattice are located on top of an atomic site of the other layer and the atoms of the other sublattice are located above a hollow sites of the other layer. This is called Bernal or AB stacking, where the atoms on top of atoms sites in the lower layer are called A, and atoms above hollow sites are called B atoms. The interlayer distance of two such graphene sheets in graphite is 0.335 nm. If a third commensurate graphene layer is added to an AB stack, then two arrangements are possible: one of the sublattices of the layer in the middle can either be sandwiched between atomic sides of both the upper and lower layers, this is called ABA stacking, or it can be positioned between an atomic and a hollow site on the two other layers, this is called ABC or rhombohedral stacking. Figure 2.1(c) schematically shows the unit cell of three graphene layers with ABA stacking.

When the surface of an AB graphene stack is scanned by Scanning Tunneling Microscopy (STM), in constant height mode, the tunneling current I is larger at atoms of the B sublattice than at atoms of the A sublattice. Analogously, in constant current mode, the STM tip height is higher at atoms of the B sublattice than at atoms of the A sublattice. This is a result of the stronger localization of π electrons on the B sites, since electrons on the A sites interact more strongly with the lower graphene sheet via the carbon atoms directly below them. On the B-sublattice, the π electron orbit therefore extend farther above the upper sheet. The sharp increase of I on atoms above hollow sites means that STM scans of AB graphene usually only reveal that half of the surface atoms, namely those belonging to the B sublattice. The space in between the closest three B sites is either an A site or a hollow site. In a STM image, the A site atoms do not appear clearly. However, at the A site triangular spaces I is slightly higher than at hollow ones, which makes it possible to determine the relative positions of the A and B sublattices by STM (this is discussed in Section 4.3).

2.1.2 Electronic properties of graphene

To describe the triangular Bravais lattice of graphene, the lattice vectors $\mathbf{a}_{1,2} = \frac{a}{2}(3, \pm\sqrt{3})$ are often used, where $a = 0.142$ nm is the shortest interatomic distance [8]. From this the nearest neighbor vectors $\boldsymbol{\delta}_{1,2} = \frac{a}{2}(1, \pm\sqrt{3})$ and $\boldsymbol{\delta}_3 = a(-1, 0)$ can be defined. These vectors are shown relative to the graphene lattice in Fig. 2.2(a). In momentum space the reciprocal lattice of graphene can be described by the vectors $\mathbf{b}_{1,2} = \frac{2\pi}{3a}(1, \pm\sqrt{3})$, that are derived from $\mathbf{a}_{1,2}$ using the condition $\mathbf{a}_i \cdot \mathbf{b}_j = 2\pi\delta_{ij}$. In (b), these vectors are shown in relation to the first Brillouin zone, which is the unit cell at the origin of the reciprocal lattice. The corners of the first Brillouin zone are described by the vectors $\mathbf{K}, \mathbf{K}' = \frac{2\pi}{3a}(1, \pm 1/\sqrt{3})$. These are the Dirac points, which have a special significance for the electronic properties that will be shown later. The electronic properties of graphene at low energies are dominated by the π electrons on the atomic sites of the two-dimensional Bravais lattice. It is possible to model them by using a Tight-Binding (TB) model which assumes that wavefunctions do not overlap, thus the π electrons are confined at the graphene atomic sites. This derivation was first shown by P. Wallace [4] and has also been described elsewhere [8, 9, 32]. In the TB model electronic charges move by 'hopping' between atoms. In order to hop an energy barrier is overcome, the strength of which determines the probability of hopping. For π electrons on pristine graphene the hopping is most likely between nearest-neighbor atoms (NN) of the same sheet, expressed by the energy parameter t. The next highest hopping probability on pristine graphene is between next-nearest-neighbor atoms (NNN) and can be represented by parameter t', where $t' < t$. The TB model can also include weaker hopping parameters, that represent interactions between sites with larger separation. However, they are routinely ignored in calculations since they are less relevant for low-energy electronic properties. Considering interactions between the first two nearest neighbors the Hamiltonian can be written as [8]:

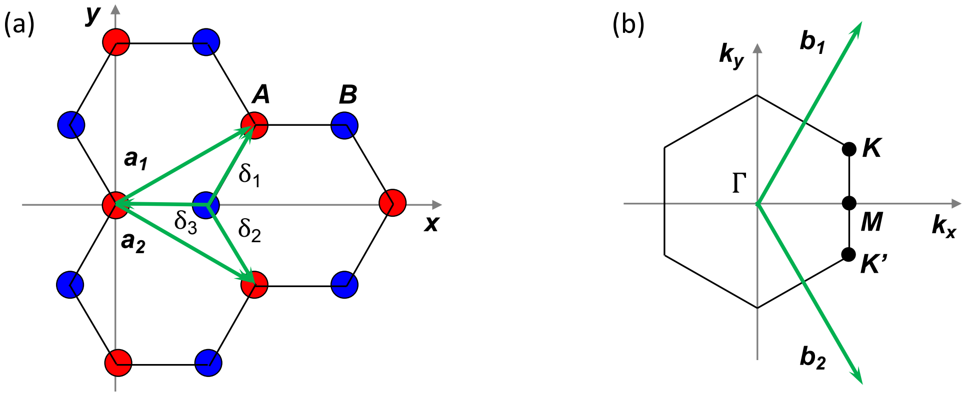

Figure 2.2: (a) Hexagonal lattice consisting of two triangular sublattices, A (red) and B (blue), and (b) first Brillouin zone of the corresponding reciprocal lattice. The lattice unit vectors $\mathbf{a}_{1,2}$, the NN vectors $\boldsymbol{\delta}_{1,2,3}$, and the reciprocal lattice vectors $\mathbf{b}_{1,2}$ are shown.

$$H = -t \sum_{<ij>} a_i^{+} b_j - t' \sum_{<<ij>>} (a_i^{+} a_j + b_i^{+} b_j) + H.c. \; , \tag{2.1}$$

where the creation/annihilation operators of an electronic excitation at atomic site i on the A and B sublattices are written as a_i^{+}/a_i and b_i^{+}/b_i, respectively. The sum over

$< ij >$ only count the NN and that over $<< ij >>$ only count the NNN sites. Because neighboring sites belong to different sublattices t only relates to hopping between and t' only to hopping within sublattices. Therefore, it can be useful to write the wavefunctions in spinor notation as $\psi_{\mathbf{k}} = \begin{pmatrix} \phi_{\mathbf{k}}^{\mathrm{A}} & \phi_{\mathbf{k}}^{\mathrm{B}} \end{pmatrix}$, where the amplitudes of the A and B sublattices are contained in the vectors $\phi_{\mathbf{k}}^{\mathrm{A}}$ and $\phi_{\mathbf{k}}^{\mathrm{B}}$, respectively. To solve Schrödinger's equation, multiplying $\psi_{\mathbf{k}}^{*}$ on the left of $H\psi_{\mathbf{k}} = E\psi_{\mathbf{k}}$ yields:

$$H_{\mathbf{k}} = E_{\mathbf{k}}\, S_{\mathbf{k}} \tag{2.2}$$

where $H_{\mathbf{k}}$ is a 2×2 matrix that contains the hopping probabilities between sublattices on the diagonal and on the same sublattice on the off-diagonal terms. In the overlap matrix $S_{\mathbf{k}}$ the non-diagonal terms are zero, since the TB model excludes overlap between sublattices, and normalizing the wavefunction imposes that the diagonal terms are each equal to 1. If the model is simplified to only include NN hopping (excluding NNN hopping and setting $t' = 0$), then no hopping occurs within the same sublattice. This truncation results in a description of low-energy properties. In this case, the diagonal terms of $H_{\mathbf{k}}$ become zero and Eq. 2.1 becomes:

$$\begin{pmatrix} E_{\mathbf{k}} & t\phi_{\mathbf{k}}^{\mathrm{A}}\phi_{\mathbf{k}}^{\mathrm{B}*} \\ t\phi_{\mathbf{k}}^{\mathrm{A}*}\phi_{\mathbf{k}}^{\mathrm{B}} & E_{\mathbf{k}} \end{pmatrix} = 0 \tag{2.3}$$

The off-diagonal terms only include the the translations to the three NN sites. The products can thus be written as $t\phi_{\mathbf{k}}^{\mathrm{A}}\phi_{\mathbf{k}}^{\mathrm{B}*} = t\sum_{l} e^{i\mathbf{k}\cdot\boldsymbol{\delta}} = t\gamma_{\mathbf{k}}$ and $t\phi_{\mathbf{k}}^{\mathrm{A}*}\phi_{\mathbf{k}}^{\mathrm{B}} = t\sum_{l'} e^{-i\mathbf{k}\cdot\boldsymbol{\delta}} = t\gamma_{\mathbf{k}}^{*}$, where l and l' indicates the sum over the three NN of A and B sublattice sites. The dispersion obtained by solving Eq. 2.3 thus becomes:

$$E_{\mathbf{k}} = \pm t\sqrt{\gamma_{\mathbf{k}}\gamma_{\mathbf{k}}^{*}}\ , \tag{2.4}$$

$$\text{where} \quad \gamma_{\mathbf{k}}\gamma_{\mathbf{k}}^{*} = 3 + 4\cos(\frac{3}{2}a\,\mathbf{k}_{\mathrm{x}})\cos(\frac{\sqrt{3}}{2}a\,\mathbf{k}_{\mathrm{y}}) + 2\cos(\sqrt{3}a\,\mathbf{k}_{\mathrm{y}})$$

In the low-energy regime, where NN interaction t dominates, this equation describes many important aspects of graphene relatively accurately. The energy dispersion of Eq. 2.4 is plotted in Fig. 2.3(a). Conduction and valence bands are symmetric and touch at six points in momentum space, which are the Dirac points at $\mathbf{K}$ and $\mathbf{K}'$. Expanding Eq. 2.4 in the vicinity of the Dirac points using $\delta\mathbf{k} = \mathbf{k} - \mathbf{K}$, and similarly for $\mathbf{K}'$, yields a linear dispersion:

$$E_{\pm}(\delta\mathbf{k}) = \pm\hbar v_{\mathrm{F}}|\delta\mathbf{k}|\ , \ \text{ where } \ v_{\mathrm{F}} = \frac{3\,a\,t}{2\,\hbar} \tag{2.5}$$

The different signs ± refer to the expansions of the conduction (+) and valence (−) bands. Together they form the Dirac cones, one of which is shown in Fig. 2.3(b). A result of this equation is that if the Fermi energy (E_{F}) is close to the energy of the Dirac points (E_{D}), then low-energy excitations follow the linear dispersion of the Dirac cones and produce ballistic electronic transport. In that case charge carriers behave as massless Dirac fermions that move at a constant speed given by the Fermi velocity $v_{\mathrm{F}} \approx 10^{6}$ m/s [7]. Therefore, an effective ultra-relativistic Dirac equation can be used to describe the electrons and predict some novel effects in graphene. Expansion of the spectrum at the Dirac points up to the second order in $\delta\mathbf{k}$ yields an additional

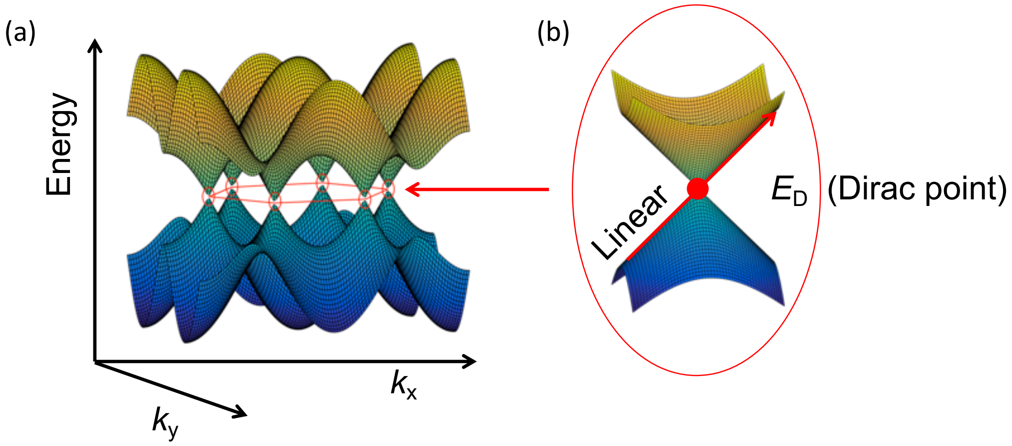

Figure 2.3: (a) Bulk graphene dispersion relation derived using the TB model with only 1st NN interaction (Eq. 2.4). The Dirac points and hexagonal first Brillouin zone is indicated in red. (b) Magnified dispersion obtained by expanding near the Dirac points (Eq. 2.5). These results have been shown in Ref. [4, 8, 9, 32].

term $\mp(\frac{3}{2}\,a^2\,t\,\sin(3\tan^{-1}(p_x/p_y))\,|\delta\mathbf{k}|^2$ in Eq. 2.5. This introduces a dependence on the direction of $\delta\mathbf{k}$ with a threefold symmetry, which is therefore called trigonal warping. The dispersion is modified if NNN interactions are also considered in Eq. 2.2. Solving it then yields:

$$E_{\mathbf{k}} = \pm t\sqrt{\gamma_{\mathbf{k}}\gamma^*_{\mathbf{k}}} - t'(\gamma_{\mathbf{k}}\gamma^*_{\mathbf{k}} - 3) \tag{2.6}$$

Expansion of this near the Dirac points introduces a summand $+3t'$ into Eq. 2.5. This shifts the bands to higher energies (for positive t and t'), thereby breaking the electron-hole symmetry.

When multiple graphene layers are commensurately stacked, the electronic properties change with the number of layers and the stacking order. This can be derived via a TB hamiltonian by introducing hopping terms between the graphene layers, which is known as the Slonczewski-Weiss-McClure model [8, 9, 33]. To calculate the dispersion, the wavefunction can be expanded to have A and B sublattice components from both layers. On two AB stacked graphene layers, which is the most stable stacking, the most significant inter-layer hopping $t_\perp$ is between A-sites that lie directly on top of each other on different layers. The simplest model is thus realized by adding a transition term between the A sublattice of the layers to the hamiltonian in Eq. 2.1. This yields two bands that touch at the Dirac points:

$$E_{\mathbf{k}} \approx \pm v_{\mathrm{F}}^2 k^2/t_\perp \tag{2.7}$$

The dispersion is not linear, but parabolic. Two additional bands that are shifted from the Dirac point by $\pm\,t_\perp$ also exist. If an electrochemical potential U_c is applied between the layers then different constant on-site potentials can be added to the upper and lower layer, respectively [8]. Including $\pm\,U_c$ in the first and second layer diagonal terms of the hamiltonian, respectively, breaks the symmetry between the layers. For $U_c << t$ this can be expanded to:

$$E_{\mathbf{k}} \approx \pm(U_c - U_c v_{\mathrm{F}}^2 k^2/t_\perp + v_{\mathrm{F}}^4 k^4/2t_\perp^2 U_c) \tag{2.8}$$

Thus an energy gap is opened between the conductance and valence band, that depends on U_c. This gap can be modified in experimental systems if a static field is applied below the bilayer graphene by a substrate due to electronic doping or a backgate. If there are more AB stacked layers, the dispersion relation depends on the number of layers N and the stacking order [8]. For Bernal stacking (ABAB ...) with an even N, $N/2$ parabolic electron and hole states appear that touch at the Dirac point. For odd N, there are $(N-1)/2$ parabolic states, as well as one linear state. For rhombohedral stacking (ABCABC ...), at the Dirac point two states follow the relation $|\delta \mathbf{k}|^N$, while $2N-2$ states are linear.

2.1.3 Epitaxial graphene on SiC

Graphene can be obtained by thermal decomposition on SiC(000$\bar{1}$), the C-terminated face of SiC, and on SiC(0001), the Si-terminated face. Both of them are schematically shown in Fig. 2.4. On the C-face, there are dangling C bonds, whereas the Si-face features dangling Si bonds. Epitaxial graphene is created when the Si atoms on the C-face or Si-face of 4H-SiC or 6H-SiC crystals are sublimated at temperatures above 1100°C (C-face), 1250°C (Si-face) [34]. After the Si atoms have desorbed, the remaining C atoms of approximately three bilayers of SiC can form one graphene layer on the crystal's surface. The growth of the epitaxial layers depends upon the face of SiC (C- or Si-face), the temperature (which promotes C-enrichment and surface diffusion) and the gas flow and pressure of desorbed Si and of the inert gas atmosphere, if it is used. On the Si-face, a C-rich layer with a C-atom density similar to graphene that is covalently bonded to the Si atoms on the SiC surface is formed. This is called the buffer layer. If more C-rich layers are grown, the higher layers assume the properties of graphene. On the C-face, the substrate does not strongly bond to the C-rich layer and graphene is formed even directly above the SiC surface. During epitaxial growth, the annealing pressure can control the C-enrichment by different mechanisms: if the sample is engulfed by Si gas, then the pressure directly adjusts the Si flow from the sample; if an inert gas environment, such as argon, is used, then the inert buffer gas reduces the probability of desorbed Si atoms returning to the sample surface and promotes C-enrichment [35, 36].

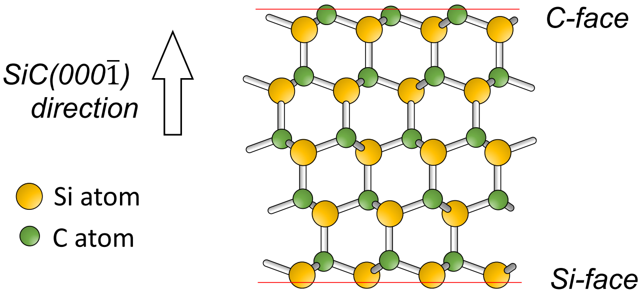

Figure 2.4: Schematic side view of 4H-SiC, the C- and Si-face of SiC(000$\bar{1}$) are marked by red lines. A similar schematic depiction is shown in Ref. [35].

Epitaxial Graphene on SiC(000$\bar{1}$)

On the C-face, the graphene growth is faster than on the Si-face and initially separate graphene domains are formed, which eventually cover the whole sample surface. During the epitaxial growth the number of layers also increases. On the C-face, the growth rate and thus the number of graphene layers differs locally [34]. On different domains the direction of the graphene lattice grown on the C-face can differ, in contrast to the Si-face. For multi-layer epitaxial graphene, results showing rotational misalignment between layers inside the graphene stacks (*i.e.* not AB or AA stacked layers) have been reported. This can be seen in the STM image Fig. 2.5(a) [37], that shows several different Moiré patterns, which are formed by misaligned lattices. However, a different study found that inside of domains AB stacking occurs and that rotational misalignment only exists between different domains at different positions [39]. The authors of that study claim that earlier LEED and x-ray diffraction studies concluded that rotational misalignment exists within stacks because they always measured several domains at once [34, 40, 41]. Nevertheless, many studies using STM, which is a local probe on the atomic scale, have found rotational misalignment of the top two [37] and of the top three surface layers [42] of epitaxial graphene. If different rotations only occurred between different epitaxially grown domains, then rotations between layers could only be expected near the domain boundaries. The authors of Ref. [39] suggest that epitaxial graphene grown at relatively lower temperatures may have smaller domains, and thus a greater portion of the surface may be covered by inter-domain boundaries, where the rotated layers routinely observed by STM could be expected.

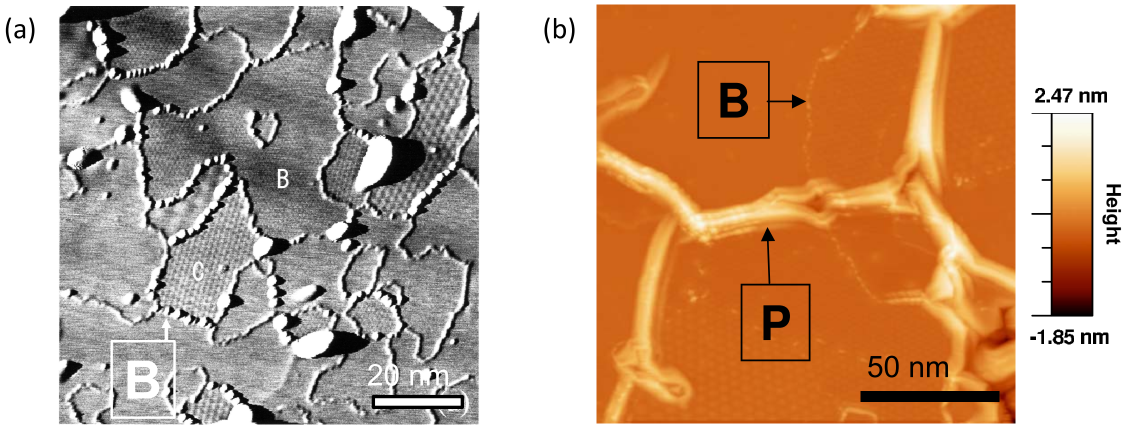

Figure 2.5: (a) STM image of epitaxial graphene/SiC(000$\bar{1}$) (grown by annealing in vacuum at 1800°C for 60 s). ”B” and ”C” mark Moiré patterns with periodicities 0.79 nm and 1.46 nm, respectively. From Naitoh *et al.*, 2003 (`https://doi.org/10.1142/S0218625X03005165`) [37]. (b) STM image of epitaxial graphene/SiC(000$\bar{1}$) (grown by annealing in vacuum at about 1150°C for 15 min). From Varchon *et al.*, 2008 (`http://dx.doi.org/10.1103/PhysRevB.77.165415`) [38]. The boxed ”B” and ”P” mark examples of bead and pleat features, respectively.

Other surface features are also frequently observed by STM, including pleats (with height 0.5-2.0 nm) and beads (with height of about 0.2 nm) [38]. They are visible in both STM images in Fig. 2.5. The tall pleats may be created by Si gas of sublimated Si that forms beneath the initially epitaxial layers. In that case, they may be precursors to carbon nanotubes that be formed on SiC(000$\bar{1}$) [37, 43]. Alternatively, it has been proposed that pleats may be created the different thermal contraction of epitaxial graphene and SiC after annealing [44].

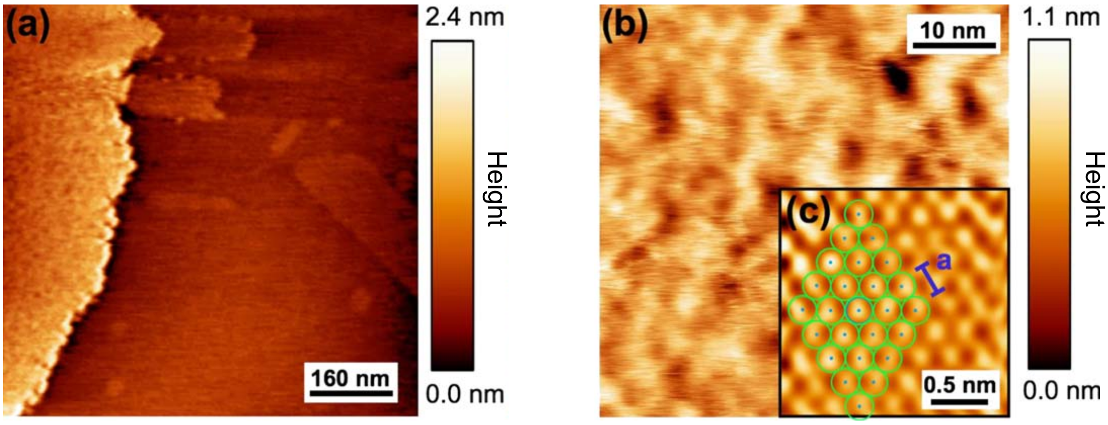

Figure 2.6: STM images of graphene (grown at 1475°C). (a) Rough graphene region (left), smooth graphene region (right). (b) Morphology of the rough graphene. (c) Atomic image on the rough region, hexagonal lattice with lattice parameter $a = 0.245$ nm is indicated. STM parameters: bias voltage $V =$ (a) 72 mV, (b)(c) 100 mV, tunneling current $I =$ (a) 5.0 nA, (b)(c) 3.0 nA. From Biedermann *et al.* (2009). (`http://dx.doi.org/10.1103/PhysRevB.79.125411`) [45].

The STM results in Fig. 2.6 show atomically smooth graphene terraces, however terraces with rough morphologies have been observed as well [45]. In Fig. 2.6(a) it can be seen that the rough terrace is separated from the smooth one by a step-edge. The corrugation on the rough terrace showed peak-to-valley heights of about 0.2-0.5 nm. Nevertheless, atomic resolution STM images confirm the graphene lattice, as seen in Fig. 2.6(b). By increasing the growth temperature, which increases the average number of layers, less rough areas were observed. The roughness may be induced by the substrate, on areas with inadequate chemo-mechanical polishing before the epitaxial graphene growth. Thus, when more epitaxial layers are grown the substrate influence is mitigated and the rough area reduced.

The electronic properties of epitaxial graphene on SiC(000$\bar{1}$) are dominated by the epitaxial graphene inside the band gap of the SiC substrate, which is 2.43 eV (4H), or 2.20 eV (6H) according to *ab initio* calculations [46]. Several experiments suggest that epitaxial graphene stacks have similar dispersions as single layer graphene. Among these are electronic transport measurements on about 10-20 layer graphene [47, 48] and Scanning Tunneling Spectroscopy (STS) in magnetic fields on about 10 epitaxial layers [49]. This is not expected on AB stacked graphene, but could be explained by rotational misalignment [50]. Thus, a significant coverage of rotated graphene layers is apparently present on many epitaxially grown samples, which could possibly depend on growth conditions.

Different electronic doping has been obtained on epitaxially grown graphene on the C-face, including both n-type and p-type doping. Several studies found n-type doping, with the Dirac point about 300 meV [53] or 200 meV [54] below the Fermi energy.

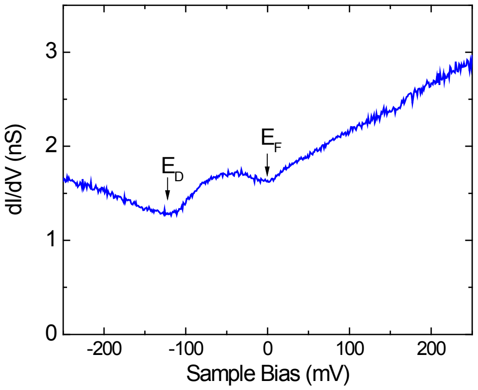

Figure 2.7: Tunnelling dI/dV (in nano-Siemens) versus bias voltage on epitaxial graphene/SiC(000$\bar{1}$) at $T = 13$ mK. Two minima appear (at $V = -125$ mV and $V = 0$). STS parameters: initial bias voltage $V = -250$ mV, tunneling current $I = 200$ pA, modulation voltage $V_{mod} = 250$ μV. Reprinted by permission from Springer Nature: Nature ”High-resolution tunnelling spectroscopy of a graphene quartet”, Young Jae Song *et al.*, (2010) [51].

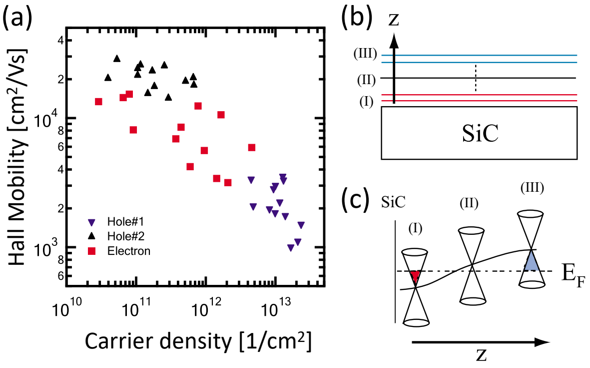

Figure 2.8: (a) Hall mobility versus carrier density, extracted by three-carrier analysis, for 13 different Hall bar devices on graphene/SiC(000$\bar{1}$). (b) Schematics of the epitaxial graphene/SiC(000$\bar{1}$) layers involving three dominant channels and (c) of the Dirac cones, shifted by doping. Reprinted from Y.-M. Lin, *et al.*, Applied Physics Letters **97**, 112107 (2010), with permission of AIP Publishing [52].

Variations of n-type doping can stem from different amounts H-atoms bonded to the SiC surface [55], as well as shielding by the lower graphene layers [42]. As an example, Fig. 2.7 shows dI/dV measured by STS on few-layer epitaxial graphene [51]. At stronger bias voltages, the dI/dV increases approximately linearly with $|V|$, as expected. Two dI/dV minima were obtained, one near the Fermi energy, and one at $V = -125$ mV. The latter one is likely due to the lower density of states (DOS) at the Dirac point, which is shifted below the Fermi energy by doping. The additional minimum close to the Fermi energy is often observed by STS, even on other samples including graphene/SiC(0001) [56] and mechanically exfoliated graphene on SiO_2 [57]. However, it has not been well-explained. Since such a DOS minimum is not indicated by ARPES measurements on graphene/SiC(000$\bar{1}$) [39, 54], it may be related to inelastic tunneling modes of the tunneling current or be the consequence of an anomaly at zero bias voltage [9]. In a different STS experiments, the Dirac point on about 10 epitaxial layers it was found close to but above the Fermi energy, signifying weak p-doping [49].

Hall transport measurements found different carrier channels by fitting the measured electronic resistivities with different types of doping [52]. The extracted Hall mobilities and carrier densities are shown in Fig. 2.8(a), they reveal two hole channels with strong and weak p-doping, and an electron channel with relatively strong n-doping. The substrate induces n-type doping, thus the electron channel can be expected on graphene layers near the substrate. The channel with relatively strong p-type doping probably lies on top of the graphene stack, where p-doping can be induced by adsorbates on the surface. The weakly doped channel can exist on intermediate layers. This scenario is illustrated in the cartoon in Fig. 2.8(b) and (c). On the surface, p-type doping can be induced at ambient conditions, likely due to an electrochemically-mediated electron transfer between oxygen and the sample [58].

Epitaxial Graphene on SiC(0001)

On the Si-face, the epitaxial layers are formed above the buffer layer, that possesses a C-atom density similar to graphene, however, it is covalently bonded to the SiC surface. Therefore, its morphology and electronic features are different from graphene. The buffer layer features a $(6\sqrt{3} \times 6\sqrt{3})R30°$ superlattice and a band gap of about 400 meV [59]. The superlattice is formed by the substrate structure and periodicity of covalent bonds. The epitaxial layers above the buffer layer are shielded from the substrate and form graphene. On the first few graphene layers the $(6\sqrt{3} \times 6\sqrt{3})R30°$ corrugation due to the buffer layer appears, but its amplitude rapidly decreases with increasing number of layers [56, 60, 61]. The $(6\sqrt{3}\times 6\sqrt{3})R30°$ lattice on the covering graphene layers contains two high symmetry points. Therefore, many authors define a (6×6) quasi-lattice that is more readily observed by STM, for example [50]. The strong interaction with the substrate during the initial phase of the growth of an epitaxial layer results in uniform alignment of the graphene layers, thus graphene grown on SiC(0001) are uniformly AB stacked. The electric properties of these layers are typical of graphene, within the band gap of the SiC substrate. However they become n-type doped by the substrate, which is strongest on the first layer above the buffer layer. The Dirac point has been reported at different values below -400 meV (with respect to the Fermi energy), and weakens on subsequent layers due to shielding. The authors of Ref. [56] reported results of STS that showed the Dirac point at -310 meV on the 2nd, -190 meV on the 3rd, and -140 meV on the 4th graphene layer. $\mathrm{d}I/\mathrm{d}V$ mesurements by STS usually obtain a minimum close to the Fermi energy. Since such a minimum is not indicated by ARPES measurements on graphene/SiC(0001) [62] it probably does not stem from the sample propertiesbut from the measurement technique [9], as discussed for graphene/SiC($000\overline{1}$).

It is possible to decouple the buffer layer from the substrate by passivating the dangling Si bonds. This has been achieved by exposing the epitaxial graphene/SiC(0001) to atomic H at temperatures between 600-1000 C° [62, 63]. As a result the buffer layer behaved an additional graphene layer. Thus, a sample with zero layers after atomic H treatment would become a single graphene layer, a single epitaxial layer would become bi-layer, and so on. Furthermore, since the Si-bonds are passivated by H-atoms the substrate does not induce strong doping and the graphene Dirac point is nearby the Fermi energy [63]. Because of the weak interaction between decoupled graphene and the SiC substrate it is termed quasi-free-standing graphene.

2.1.4 Graphite surface

Graphite is a crystal of graphene layers with Bernal stacking, since there are three distinct stacking positions the size of the unit cell may vary, for example it may be hexagonal (ABAB ...), as shown in Fig. 2.1(c), or rhombohedral (ABCABC ...). Crystals of graphite occur naturally and can also be artificially created. In this work, most graphite samples are highly oriented pyrolytic graphite (HOPG), that is synthesized by a thermolytic process. Inside the graphene planes, it has a crystallite domain size in a is between

1 to 10 μm. Perpendicular to the graphene planes, it is highly ordered in the c-axis, but it has many stacking faults [64, 65]. One of the samples is Kish graphite, which is formed on the surface of molten iron. Differently from HOPG, it can be considered to have a semi-infinite thickness [64].

The electronic properties of graphite depend on the stacking order and on the effective number of electronically coupled layers [66]. On the surface of graphite, the states at the Fermi energy are dominantly located on the sites without lower-layer neighbors. Thus, constant height STM on graphite measures a higher I on one sublattice, as on any AB stacked graphene layers [67]. When more layers determine the electronic properties of a graphene stack, the states at the Fermi energy increases accordingly. However, the effective number of layers is reduced by inhomogeneous charge distribution between layers. These can occur due to stacking faults. In such a case, only a few graphene layers on top can dominate the electronic surface properties of graphite [68]. A study combining STS measurements and first principles calculations of graphite in magnetic fields found different effective thicknesses for different graphite samples [64]. Kish graphite and HOPG were probed by STS and the results simulated by calculations. For Kish the experimental results were well reproduced by a model of an infinite stack, but for a result on HOPG the best match was obtained by assuming a 40 layer stack. A different study of the out-of-plane conductivity found that the top 60 layers contribute to the electronic properties on the surface [65] This is consistent with the lower density of stacking faults expected on Kish.

Nevertheless, on the surface of graphite, the the topmost layer dominates the local electronic properties. Thus, when features on the surface of graphite are probed by STM/STS, then a two-dimensional, single layer graphene model is often sufficient to describe the most significant properties that can be observed, *e.g.*, for single vacancy states [69] or for zigzag edge states [11–13] (see Section 2.2.3). Because of the AB stacking, the graphene sublattice symmetry is broken. Thus, as on AB stacked graphene, on the surface of graphite, hyperbolic dispersions on both sides of the Dirac point can be obtained, which is at the Fermi energy [32]. In the present work, STM/STS was utilized to probe the surface of graphite samples. Since the graphene layers at the surface dominate the features that were measured, no significant difference between Kish graphite and HOPG was found.

2.2 Graphene Zigzag Edge State

2.2.1 Zero-energy modes in graphene

The TB model (introduced in Section 2.1.2) not only gives good approximation of the electronic properties of pristine graphene at low energies, but it also reveals a condition for the presence localized electronic states in disordered graphene. In the low-energy approximation of the TB model, where only the hopping parameter t is non-zero, the solutions can be separated into parts that have non-zero amplitudes only on one of the two sublattices. Such a system is described by a bipartite lattice, where the wavefunctions that exist on the A sublattice do not interact with wavefunctions on the B sublattice, and all solutions thus have thus two independent parts. In pseudo-spin notation that was introduced in Section 2.1.2 the bipartite Hamiltonian can be written as:

$$\psi^*_{\mathbf{k}} H \psi_{\mathbf{k}} = \begin{pmatrix} \phi^{\mathrm{A}*}_{\mathbf{k}} & \phi^{\mathrm{B}*}_{\mathbf{k}} \end{pmatrix} \begin{pmatrix} E^{\mathrm{A}}_{\mathbf{k}} & h_{\mathrm{AB}} \\ h^{+}_{\mathrm{AB}} & E^{\mathrm{B}}_{\mathbf{k}} \end{pmatrix} \begin{pmatrix} \phi^{\mathrm{A}}_{\mathbf{k}} \\ \phi^{\mathrm{B}}_{\mathbf{k}} \end{pmatrix} = E_{\mathbf{k}} \tag{2.9}$$

If the number of sublattice sites is equal, then so is the number of amplitudes in the vectors $\phi^{\mathrm{A}}_{\mathbf{k}}$ and $\phi^{\mathrm{B}}_{\mathbf{k}}$, and the solutions are also symmetric. However, if the dimension of the two vectors is not equal, then there exist more solutions on the majority sublattice, whose number is equal to the imbalance of the amplitudes on the sublattices [70, 71]. These states, created by the defects in the graphene lattice, are thus related to the difference in the number of orbitals contributing to the wavefunctions on the sites of the two respective sublattices, which can be called the sublattice imbalance. This can occur, *e.g.*, if there is a single atomic vacancy or a chemical bond that removes one π electron orbit from the system. Then, the number of amplitudes in $\phi_{\mathbf{k}}$ of the minority sublattice is reduced by one and there exists a state on the majority sublattice that can be localized at the origin of the sublattice imbalance [70, 71]. In general, any difference of the number of π orbitals on the two sublattices induces a proportionate number of defect-induced states on the majority sublattice. Thus, if an imbalance of π orbitals exceeding one exists, then more than one defect-state can be induced. On the other hand, if atomic sites are missing on both sublattices, the number of defect-states may be less than if defects exist only one sublattice. Because defect states decay away from the defect [70], the local distribution of defects, which determines the sublattice imbalance, also determines the distribution of localized electronic defect states.

The simplest instance of a zero-energy mode is a single vacancy, for this case there are both theoretical [70] and experimental results [69]. At a single vacancy an electronic state appears that decay away from the vacancy following an inverse power law.

The simulated DOS at single vacancies on graphene using the TB model [14] is shown in Fig. 2.9. The figs.(a)-(c) show results of a system with one isolated single vacancy, the LDOS indicates the density of states close by the vacancy, whereas the DOS indicates an average of the whole system, where the vacancy states have little influence compared to the bulk states. The case $t' = 0$ (where higher order interactions are also zero) describes a perfect bipartite system with electron-hole symmetry. At the Dirac point, at $E = 0$, appears a resonance peak due to the vacancy states (see (a)). The interaction of states on the two sublattices when $t' \neq 0$ breaks the particle-hole symmetry, and both the Dirac point and the resonance peak are shifted from $E = 0$ (see (b)(d)). Notably, the peak is shifted to an energy that is closer to the Fermi energy than the Dirac point. Figures 2.9(d)(e) show results for a graphene system with concentrations (x) of randomly distributed single vacancies, since there is a greater number of vacancies they significantly affect the DOS that is averaged over the whole system. In the case of many, randomly distributed single vacancies, the resonance also appears, but it is accompanied by an increase of the spectral weight at surrounding energies. Although overall the sublattices have the same number of atomic sites, since vacancies occur on both equally, the localized character of the vacancy states causes them to appear at local clusters with sublattice imbalances. The increase of the DOS in an energy range has also been derived using a coherent phase approximation [72].

A random distribution of vacancies does not create a great imbalance between the sublattices, however a larger imbalance is created if vacancies preferentially distributed

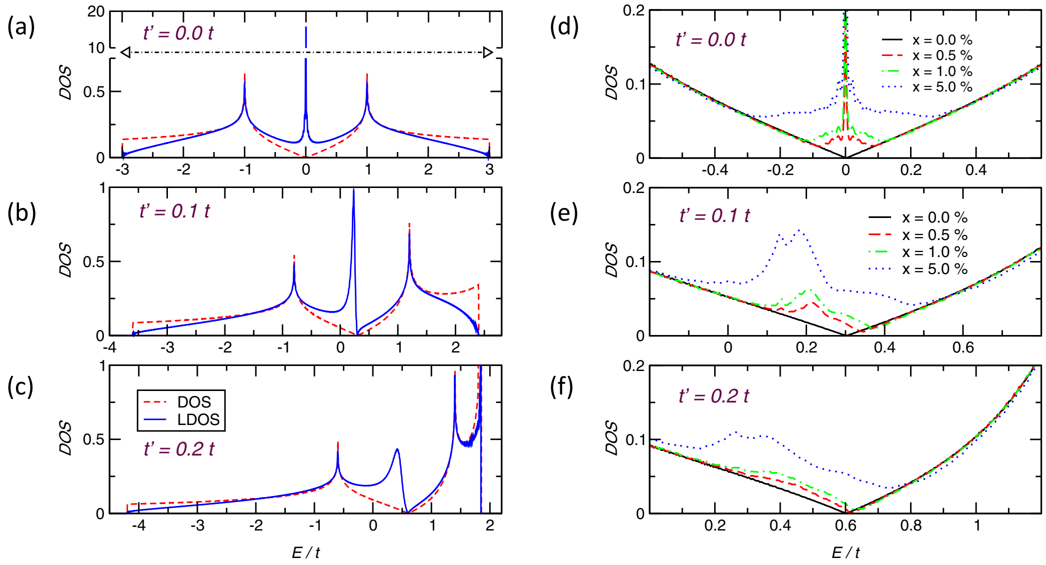

Figure 2.9: Numerical results for the density of states in the vicinity of (a)-(c) a single vacancy or (d)-(f) many random vacancies on graphene with vacancy concentration x. Calculations (a)-(d) without and (b)(c)(e)(f) with next-nearest-neighbor interaction (mediated by t') are shown. From Pereira *et al.*, 2006 (`http://dx.doi.org/10.1103/PhysRevLett.96.036801`) [14].

on one sublattice. DOS of graphene with vacancies on only one sublattice was investigated by numerical calculations that use the TB model [70]. It was found that in addition to the resonance peak at the Dirac energy a suppression of the DOS appears (see Fig. 2.10(a)). Furthermore, the DOS gap is approximately proportional to the square root of vacancy concentration on one of the two sublattices (see (b)).

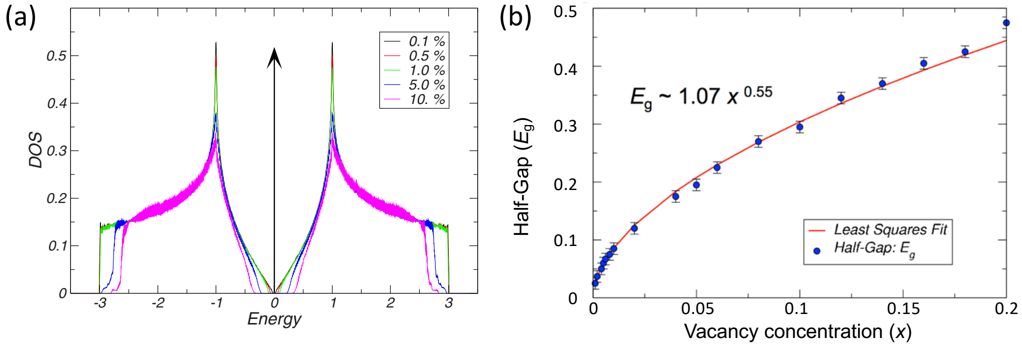

Figure 2.10: (a) Calculated DOS of graphene with a distribution of single vacancies on one sublattice. Calculation of a TB model with only nearest-neighbor interaction ($t' = 0$) and with 4×10^6 atomic sites. (b) Half-gap energy versus vacancy concentration (x) on one sublattice with a least square fitting. From Pereira *et al.*, 2008 (`http://dx.doi.org/10.1103/PhysRevB.77.115109`) [70].

To check this behavior single vacancies distributions with a greater number on one sublattice was also simulated (Fig. 2.11) [70]. This allows the variation of the degree of sublattice uncompensation μ without changing the total vacancy concentration. η indi-

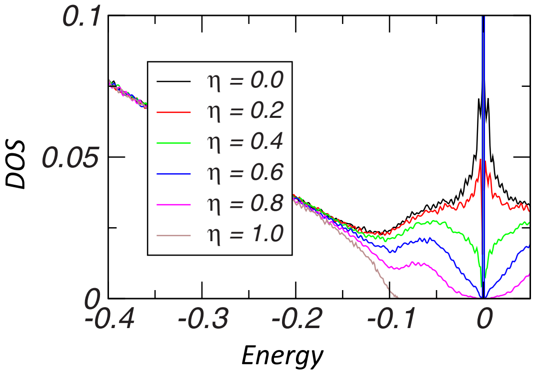

Figure 2.11: Simulated DOS of random single vacancies that are preferentially distributed on one of the two sublattices with degree of uncompensation η versus energy, with vacancy concentration $x = 0.01$ vacancies/atoms. From Pereira *et al.*, 2008 (`http://dx.doi.org/10.1103/PhysRevB.77.115109`) [70].

cates the the distribution between the sublattices, with $\eta = 1.0$ signifying all vacancies on one sublattice and $\eta = 0.0$ equal vacancies on both sublattices. The depression energy range is gradually filled by DOS that is proportional to η. At higher concentrations x this becomes more significant at lower η. Therefore, the DOS depression near the Dirac point is proportional to the sublattice imbalance created by the vacancies.

2.2.2 Theory of the graphene zigzag edge state

Graphene edges, excluding lattice reconstructions, form one of two different structures, that are named armchair edges and zigzag edges (as shown in Fig. 2.12). At armchair edges the neighboring edge atoms alternatively belong to both sublattices. Thus, the atoms that are missing beyond the edge also belong to both sublattices and there is no imbalance between A and B sublattices along the edge. At zigzag edges all edge atoms belong to the same sublattice and all missing atoms beyond the edge belong to the other sublattice. Because of this, there is a high sublattice imbalance at zigzag edges and localized electronic states exist, but not at armchair edges.

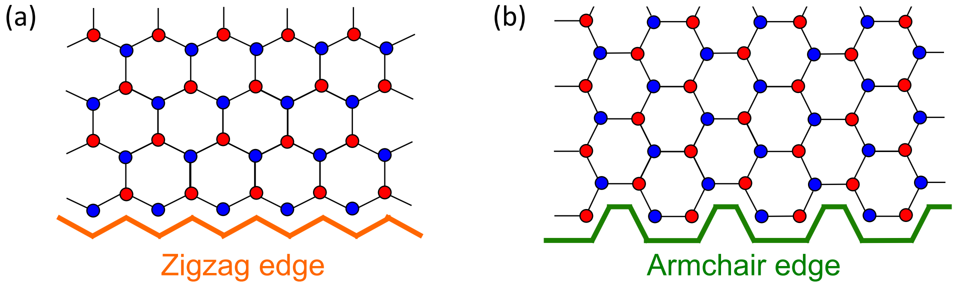

Figure 2.12: Schematic graphene (a) Zigzag edge and (b) Armchair edge. Red/blue dots show C-atoms on the A/B sublattice, black lines represent valence bonds.

Zigzag edge states have been first theoretically predicted by Fujita *et al.* in 1996 [10, 73] and later they were experimentally confirmed in 2005 [11, 13]. The first calculated band structures [10] that showed flat bands due to edge-localized states were of

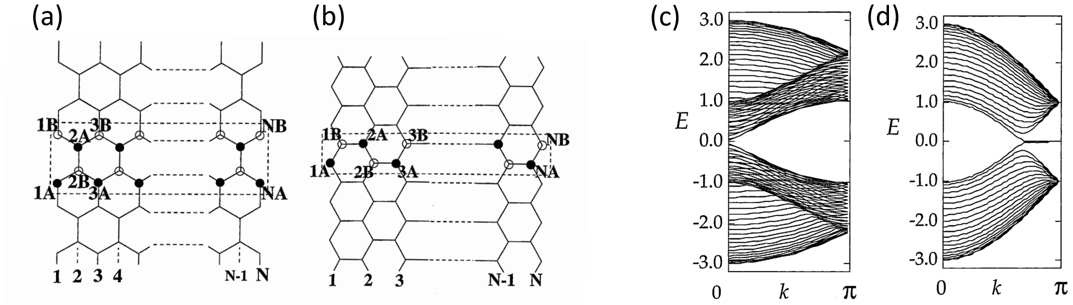

Figure 2.13: Infinite Graphene nanoribbons schematics (a)(b) and corresponding simulated band structures (c)(d). GNRs with (a)(c) armchair edges and (b)(d) zigzag edges are shown. The bottom numbers label the lateral position of (a) dimers or (b) zigzag chains. In (a)(b) the rectangles show the unit cells and the labels indicate the position and sublattice of the atomic sites in them. The width of the calculated nanoribbons is $N = 20$ (about 4.1 nm). From Fujita *et al.*, 1996 (`https://doi.org/10.1143/jpsj.65.1920`) [10].

infinitely long one-dimensional graphene nanoribbons (GNR) with zigzag or armchair edges (see Fig. 2.13), these used the TB model and considered 1st NN interaction only. The unbonded electrons at the edge atoms are ignored in the calculations and did not contribute to the electronic band structure, which is effectively similar to assuming that the edge atoms are each passivated by a single hydrogen atom. The electronic bands of the armchair ribbon in Fig. 2.13(c) resemble the band of bulk graphene when projected onto the armchair edge direction. However, for the band structure of the π electrons on the zigzag ribbon (Fig. 2.13(d)) a remarkable difference appears between the wavenumbers $2\pi/3 \leq |k| \leq \pi$, where valence and conduction bands form a degenerate flat band at the Dirac point energy ($E = 0$). This band is flat at $k = \pi$ and becomes dispersive when k reaches below $2\pi/3$, where the Dirac point of bulk graphene is located. The flat band remains stable even when the ribbon width is increased. Actually, the flat band region of k increases with the ribbon width (see Fig. 2.13(d) and 2.14). Therefore, the real space distribution of the edge state becomes wider with the nanoribbon width, at

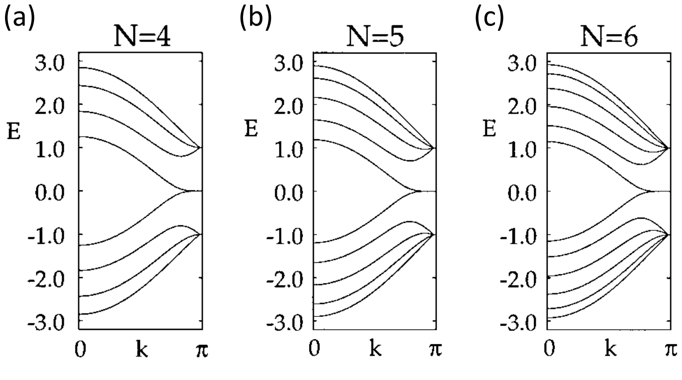

Figure 2.14: Calculated band structures of GNRs with zigzag edges with (a) $N = 4$ zigzag chains (width about 0.7 nm), (b) $N = 5$ (width about 0.9 nm), (c) $N = 6$ (width about 1.1 nm). From Nakada *et al.*, 1996 (`http://dx.doi.org/10.1103/PhysRevB.54.17954`) [73].

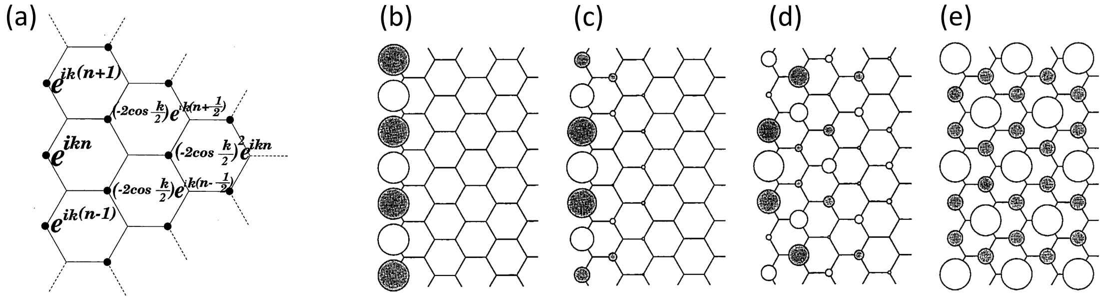

Figure 2.15: (a) Schematic representation of the analytic solution of the zigzag edge state on the edge sublattice (solid circles) near the edge is shown. (b)-(e) Schematic representation of the real component of the analytical state in the flat bands near the zigzag edge. The black and white circles represent the difference in sign. The solutions for (b) $k = \pi$, (c) $k = 8\pi/9$, (d) $k = 7\pi/9$ and (e) $k = 2\pi/3$ are shown. From Fujita *et al.*, 1996 (`https://doi.org/10.1143/jpsj.65.1920`) [10].

least as long as the GNR width is sufficiently narrow [73]. Since it does not disappear at larger widths it becomes clear that the flat band is not a feature of the GNR, but instead it arises alone from the zigzag edges. In this simulation states on different sublattices do not interact and the flat band states are thus confined to the edge sublattice. In parallel direction to the zigzag edges the states undergo a band inversion when crossing the bulk graphene Dirac points, which increases the robustness of the edge-localized states [9, 74].

Fujita *et al.* derived an analytical solution for this flat band state, which is shown in Fig. 2.15. This solution can be constructed as a linear combination of atomic orbitals on the edge-sublattice sites, which satisfies two conditions: for the flat band states at $E = 0$ the sum of the complex wavefunction over neighboring sublattice sites must be zero, and, because of the translational symmetry, the Bloch components on successive edge sites must differ by a phase factor e^{ik}, for the lateral wavenumber k. In this semi-infinite system, the convergence condition for the wavefunction becomes $|2\cos(\frac{k}{2})| < 1$, and the state of the flat bands only exist in the range allowed by this convergence condition (*i.e.* $2\pi/3 \leq |k| \leq \pi$). The analytical solution confirms the range of the flat bands that was obtained by the simulations (Fig. 2.13). Figure 2.15(b)-(e) show the real component of the analytical solution at various values of k within the convergent range. It can be seen that in the flat band regime the flat band function decays exponentially away from the edge, where the decay constant depends on k and is smallest at $k = \pi$. Therefore, these electronic states are localized on the zigzag edge of graphene. TB simulations by Niimi *et al.* of mixed zigzag and armchair edges show that the zigzag edge state is robust on edges with finite length, even when small zigzag segments are in close proximity of armchair segments [12]. These simulations yielded an exponential decay length of $\xi = 0.5$ nm at pure zigzag edges and found an increase up to $\xi = 1.2$ nm near armchair segments. At mingled zigzag and armchair edges they also found that the calculated local density of states (LDOS) is increased on a $(\sqrt{3} \times \sqrt{3})R30°$ superlattice (relative to the graphene lattice). Both the longer decay constant $\xi = 1.2$ nm and the $(\sqrt{3} \times \sqrt{3})R30°$ superlattice are experimentally supported [11–13], which is discussed in the next section.

2.2.3 Experimental results of graphene zigzag edge states

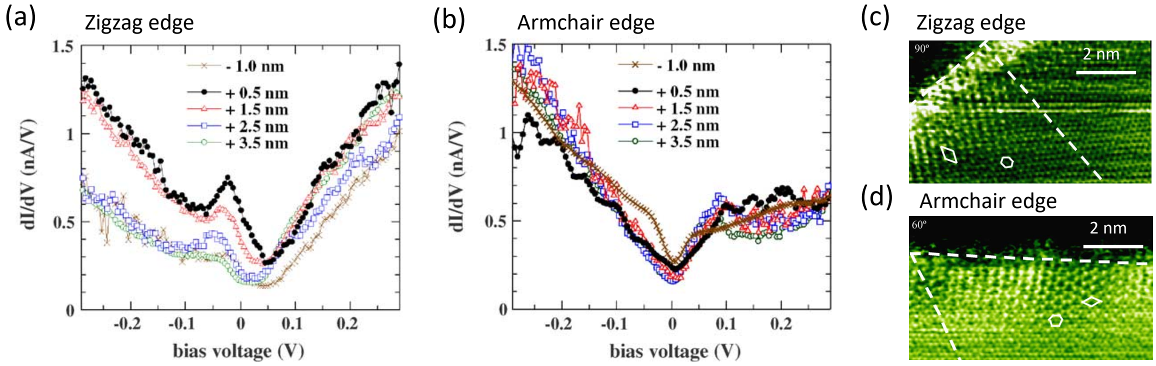

Figure 2.16: STM/S measurements of zigzag and armchair rich step-edges on ZYX graphite. (a)(b) dI/dV versus bias voltage V at different distances from each edge (at $P \leq 2 \times 10^{-7}$ Pa, $T = 77$ K). (c)/(d) STM images near zigzag/armchair rich edges (in air, $T = 300$ K, $V = 0.1$ V, $I = 0.1$ nA). The graphene sublattice and the $(\sqrt{3} \times \sqrt{3})R30°$ superlattice unit cells are marked by a white hexagon and diamond shape, respectively, the dashed lines highlight the edge and the superlattice directions. From Niimi *et al.*, 2005 (`https://doi.org/10.1016/j.apsusc.2004.09.091`) [11].

Due to the zigzag edge state, the electronic density of states near the Dirac point energy is increased on the edge sublattice of zigzag edges. This LDOS peak can be measured by combined scanning tunneling microscopy and spectroscopy (STM/STS). Such a study was first reported by Niimi *et al.* in 2005 [11], some results of which is shown in Fig. 2.16. They observed a dI/dV peak near the Fermi energy that only appeared on naturally existing zigzag step-edges, and not on the armchair ones, on the surface of ZYX-grade exfoliated HOPG with single crystalline sizes between 100-200 nm. Step-edges have the monatomic height of one graphene layer. This peak of the measured dI/dV decays exponentially with distance from the edge (Fig. 2.16(a)) with decay length of 1.2±0.5 nm [12]. By comparing experiment and theory, they concluded that the LDOS peak is a result of the zigzag edge state [11, 12].

A similar result was reported by Kobayashi *et al.* in the same year [13], who studied HOPG that was repeatedly heated (to 800°C in UHV) and exposed to atomic hydrogen. This group also found dI/dV peaks that only appeared on zigzag-direction edges. In the former experiments by Niimi *et al.* [11, 12], the localization of the LDOS peak only at the zigzag edge and its decay into the bulk terrace were clearly observed, showing good agreement with the theoretically predicted edge state. However, the edge termination is unclear. On the other hand, in the latter experiment [13], edge termination by hydrogen can be safely expected, but unfortunately the spatial variation of the peak was not observed. In addition, in both of these studies, the atomically resolved topographical structure on the edge was difficult to determine directly by STM. This is presumably due to the increased LDOS along the edge. Thus, the direction of straight edges is compared with the atomic rows in the bulk away from the edges instead. Both experimental studies observed the $(\sqrt{3} \times \sqrt{3})R30°$ superlattice that is associated with mixed zigzag and armchair edges (see Figs. 2.16(c)(d)), thus it is more accurate to call the edges they studied zigzag-and armchair-rich edges. On zigzag edges, few, short armchair edge segments may occur despite edges having approximately zigzag-direction. This may be the case if an edge atom is missing. The edge feature may also be changed by different chemical bonding on the edge atoms. When the third sp^2 atom at the edge atoms is not bonded, dangling bond states are expected to contribute to the $\mathrm{d}I/\mathrm{d}V$ spectrum close to the Fermi energy. This would occur at both the zigzag and armchair edges. Since the studies shown here did not observe a $\mathrm{d}I/\mathrm{d}V$ peak at armchair edges, the sample edges are probably passivated. Noting the narrowness of the measured LDOS peak (≈ 80 meV) Niimi *et al.* [12] concluded that the termination is by a single hydrogen at each edge atom. On the other hand, it is noted that the peak width observed in Ref. [13] is about two times wider.

2.3 Graphene Zigzag Nanoribbon

2.3.1 Theory of the spin-polarized edge state

Free standing graphene

Due to the high density of states, the electron-electron interaction becomes important on zigzag edges. In the case of a weakly doped graphene zigzag edge, the LDOS at the Fermi energy becomes relatively high. Therefore, qualitatively the Stoner criterion for magnetic ordering can be satisfied [75] and ferromagnetic alignment of the electron spins of the edge state can be favored over a paramagnetic state. The first published calculation of the zigzag edge state [10] already examined the possible polarization of the edge states on graphene nanoribbons with zigzag edges (zGNR) by calculating the magnetic moment of the edges (using the Hubbard model with a Hartree-Fock approximation). Their calculations showed that a zGNR with a width of 10 atomic chains (about 2.0 nm) would have finite magnetization independently of the on-site potential. Based on the Stoner criterion, magnetic ordering appears possible even on isolated zigzag edges that are not nearby another zigzag edge. However, according to the Mermin-Wagner theorem [76] magnetic ordering would not be stable on such a one-dimensional structure at temperature $T \neq 0$ or even at $T = 0$. Indeed, DFT calculations have shown that magnetic order would be limited by thermally induced spin-wave fluctuations within magnetic correlation lengths that increase exponentially when T decreases below 10 K, and decay with T^{-1} at higher T [77]. At $T = 300$ K, first principle calculations suggest a magnetic correlation length of about 1 nm. However, on zGNRs two different edge states on opposite edges can have magnetic interactions that may stabilize the magnetic order at $T \neq 0$ [16]. This is possible, since the different sublattices, and thus the different edge states, interleave on the zGNR. When the spin coherent length and edge state decay length is sufficiently long, and the zGNR sufficiently narrow, magnetic interaction between the edges that stabilizes spin-polarization can occur.

It should be noted that, apart from zigzag edges, magnetic order can also be induced in graphene by vacancy states [78] which carry a magnetic moment [79]. Similarly to the results on zGNRs, first principles calculations show that different interactions between defect states on the same and on different sublattices create magnetic order [80]. Furthermore, magnetic order has been predicted on nano-graphene bilayer structures [81].

For zGNRs, the energy of different spin configurations of the edge state electrons was calculated using a local spin density approximation [15]. It was found that energetically favorable spin alignments are those in which spins along each edge are aligned. This is possible with either parallel alignment on opposite edges (*i.e.* ferromagnetic alignment, FM), or anti-parallel alignment on opposite edges (*i.e.* anti-ferromagnetic alignment, AM). A representation of these two spin configurations is shown in Fig. 2.17. Among the two states, AM is more stable, yielding an energy lower by 2.3 meV/atom than for FM. Compared to a paramagnetic state, AM reduces the system's energy by 239.9 meV/atom. Furthermore, the calculated energy difference between AM and FM was reduced by increasing the zGNR width, which was also derived in other theoretical studies [82].

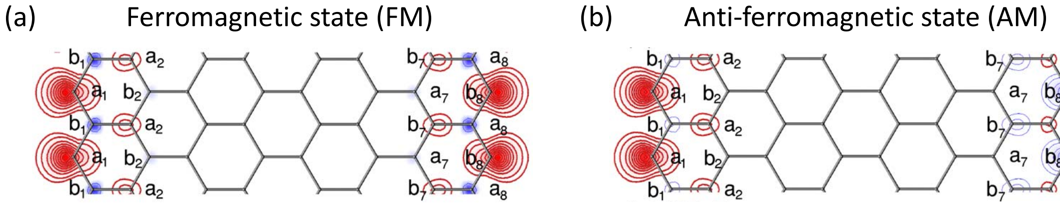

Figure 2.17: Schematics of zGNRs (width 1.6 nm, 8 atomic chains) with calculated spin densities of the edge states (up/down shown in red/blue colors) for (a) FM and (b) AM configurations. From Lee *et al.*, 2005 (`http://dx.doi.org/10.1103/PhysRevB.71.193406`) [15].

The stability of the spin polarized state depends on the electronic doping, as well as the zGNR width. This has been investigated using a π-orbital Hubbard-model self-consistent field theory [83, 84]. According to these calculations, increasing the doping can change the ground state. For weak doping, the ground state changes from AM to a canted inter-edge spin alignment to FM (the canted state has relative inter-edge spin angle that is between 180° (AM) and 0° (FM). For a zGNR of width 2.0 nm, doping must shift the Dirac point by more than 1 eV away from the Fermi energy to induce a transition to a paramagnetic state [83, 84].

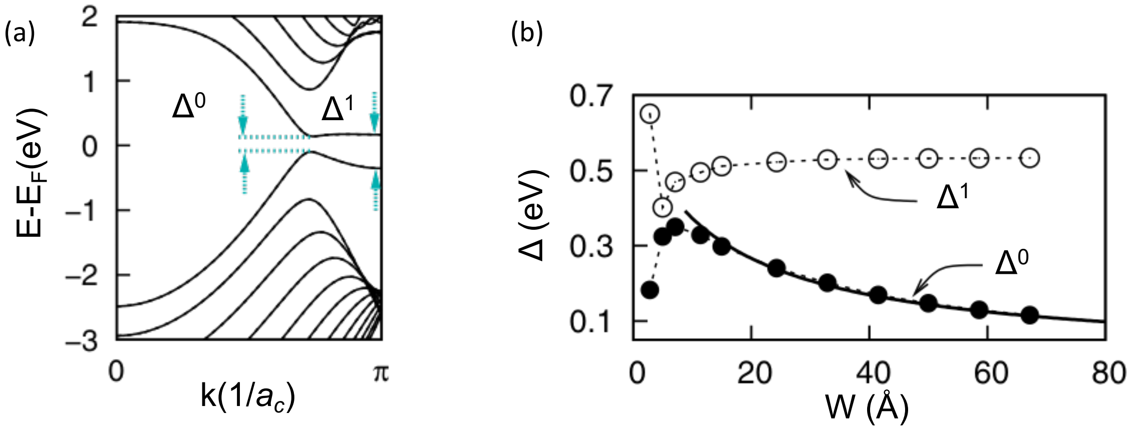

Figure 2.18: (a) Calculated band structure of a zGNR of width $N = 12$ atoms (about 2.4 nm), the direct band gap (Δ^0) and the gap at wavenumber $k = \pi/a_c$ (Δ^1) are indicated ($a_c = 0.246$ nm). (b) Δ^0 and Δ^1 for different zGNR widths W are shown. The solid line is a fit of Δ^0 of the form $9.33/(W + 15.0)$. From Son *et al.*, 2006 (`http://dx.doi.org/10.1103/PhysRevLett.97.216803`) [16].

When the edge states on a zGNR are spin-polarized, the electronic band structure is changed. In the AM configuration, the states on nearest-neighbor sites on the zGNR have opposite spin-alignment, thus a band gap is expected for AM (but not for FM) [85]. The electronic band calculated by local spin-density approximation (LSDA) [16] is shown in Fig. 2.18(a). The lifting of the spin degeneracy of the edge states opens a band gap. The band splitting can be defined by a direct gap Δ^0 at $k = 0.75\pi/a_C$ and a larger gap Δ^1 at $k = \pi/a_C$, where $a_c = 0.246$ nm is the the lattice constant. The same theoretical study investigated the change of the band structure with different widths W. The two splittings are plotted against W in (b). For zGNRs with $W > 0.5$ nm, Δ^0 decreases and Δ^1 increases with increasing W. Whereas Δ^1 rapidly reaches a saturated value at 0.53 eV, Δ^0 continues to decrease even at wider W, following a $1/W$ decay.

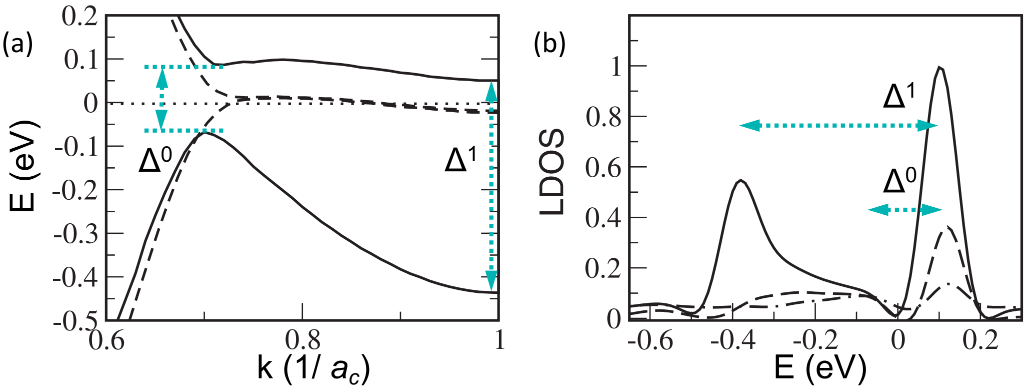

Figure 2.19: (a) Band structure and (b) local density of states (LDOS) calculated for a zGNR with width $N = 20$ atomic chains (about 4.1 nm) by LSDA. In (a), the solid line is the AM polarized state, and the dashed line is the non-magnetic state. In (b), the solid line shows LDOD on the edge atoms, the dashed one that on the third, the dot-dashed line that on the fifth atoms from the edge. Δ^0 and Δ^1 are indicated. From Jiang *et al.*, 2008 (`http://dx.doi.org/10.1103/PhysRevLett.101.246803`) [86].

Another LSDA calculation of the spin-split edge states on a zGNR is shown in Fig. 2.19(a) [86]. This shows the bands for both the spin-polarized ground state (solid line) and for the paramagnetic state (dashed line). These results are similar as those obtained by the previous study, however the spatial distribution of the states across the zGNR is considered as well. The LDOS of the first three edge sublattice sites is shown in (b). The states at $k = \pi/a_c$, that form Δ^1 are strongly localized on the edge atoms, and Δ^1 is not dependent on W, as seen in Fig. 2.18(b). Thus this gap stems purely from the edge state spin-alignments. On the third and fifth atomic row from the edge, only the more extended states near $k = 0.75\pi/d_z$ appear, which form Δ^0. Since Δ^0 is proportional to $1/W$ (see Fig. 2.18(b)), this gap stems from the confinement of the states on the zGNR and becomes dominant in the LDOS at positions not exactly on the edge atoms. According to these calculations, Δ^0 would appear on a wider area than Δ^1, and that the higher energy LDOS peak would be sharper than the lower one, at least theoretically. These results are worth noting, when considering local tunneling spectroscopy measurements (STS).

For better comparison with experimental data, the effects of zGNR width, edge defects and environmental screening on spin-polarized edge states were investigated via a first-neighbor TB model (with hopping integral t) including e-e interaction [31]. Different chiral edges were considered. Zigzag and armchair edges are mixed on regular intervals on chiral edges, *e.g.*, 8 zigzag edge sites followed by 1 armchair site. Thus, chiral edges form an angle θ with zigzag edges, which increases with the amount of armchair segments. These calculations for chiral edges can suggest the effect of edge impurities on a zigzag edge state. The substrate screening is incorporated in the on-site Coulomb repulsion parameter U. The results of the gaps Δ^0 and Δ^1 at various θ and W are shown in Fig. 2.20, where (a) shows results for several nanoribbon widths W, and (b) for several U. The tight binding gaps Δ_g, which are not related to the edge states, are also plotted. As derived previously [16], Δ^1 is relatively independent of W, while Δ^0 increases with decreasing W. Both gaps decrease as the amount of armchair segments increases and both disappear for angles between $15° - 25°$. Δ^1 is more sensitive to θ than Δ^0. The results of Ref. [31] show that the presence of some armchair segments does not greatly change Δ^0 of a spin-polarized edge, especially on wider zGNRs. This is because Δ^0 is due to confinement, and thus mainly depends on W. The results of different U was only investigated for $W \approx 1.1$ nm, on which it drastically changed the results of both Δ^0 and Δ^1, showing the importance of the substrate influence. The confinement gap Δ_g appears when the edge states seize to dominate the low energy properties of the zGNRs. Thus, Δ_g is zero for small values of θ and reaches a maximum at $\theta = 30°$, which corresponds to the armchair edge, where no edge states exist.

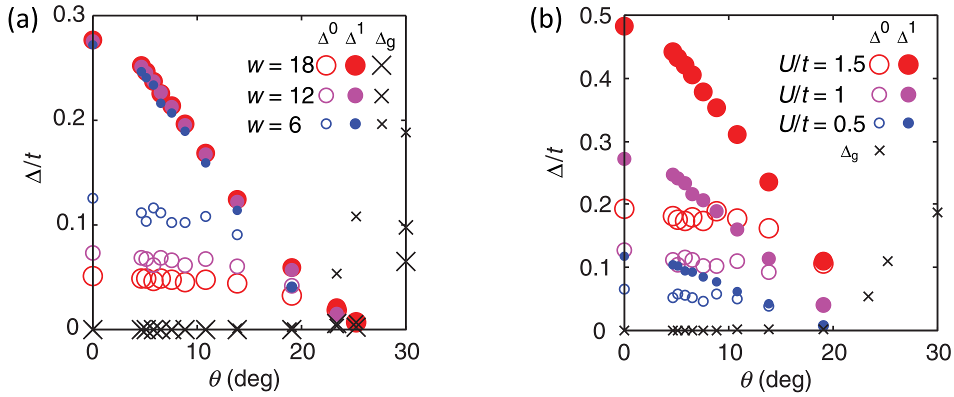

Figure 2.20: Calculated electronic band gaps Δ^0, Δ^1 and Δ_g versus edge direction θ of spin-polarized edge states on nanoribbons with chiral edges. Δ^0 and Δ^1 are the spin and confinement induced gaps of the spin-splitted edge states. Δ_g is the band gap derived from tight binding calculations. (a) shows results for different nanoribbon widths w and $U/t = 1$. (b) shows results for different U and $w = 6$. The unit of w is the number of atoms across the nanoribbons, $W = 6, 12, 18$ is about 1.1, 2.4, 3.7 nm, respectively. From Yazyev *et al.*, 2011 (`http://dx.doi.org/10.1103/PhysRevB.84.115406`) [31].

Graphene on substrate

Although the substrate effect was considered by taking account of the screening effect in the previous theoretical works [31, 84], the substrate was more directly considered in the work of Chen and Weinert [18]. They simulated the electronic states band structure of spin-polarized graphene nanoribbons on top of an infinitely large single graphene layer (with AB stacking), *i.e.*, a graphene substrate, by density function calculations [18]. Thus, this is the simplest model of our experimental system, like ZGNRs on graphite. The results of these calculations are presented in Figs. 2.21(a)(b). In (a), a schematic of

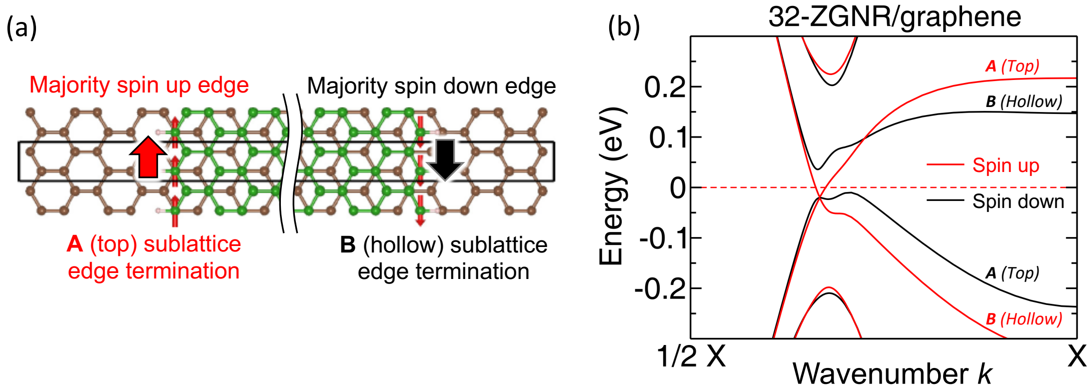

Figure 2.21: Calculated band structure from Ref. [18] of a spin-polarized zGNR with a width of 32 zigzag chains, *i.e.* $W = 6.7$ nm, on top of a graphene layer with Bernal stacking. (a) Schematic of the model zGNR (green lattice) on top of graphene (brown lattice), adapted with modifications from Ref. [18]. The black rectangle marks the unit cell used for calculations. The large red/black arrow are next to the edge that terminates on the A/B sublattice with majority spin up/down. (b) Calculated band structure, spin up states (red curves) and spin down states (black curves). Labels indicate the states close to Energy = 0 on the A and the B sublattices. Adapted from Chen and Weinert, 2016 (`http://dx.doi.org/10.1103/PhysRevB.94.035433`) [18].

the simulated zGNR and graphene are shown. (b) shows the simulated band structure of a spin-polarized zGNR with $W = 6.7$ nm. Due to the AB stacking the sublattice symmetry is broken, thus spin up and down bands are non-degenerate on the different sublattices. In the simulated model, close to Energy = 0, the valence band states on the A sublattice host down spins, while those on the B sublattice host up spins. The spins are reversed on the conduction bands. In (b) close to the Fermi energy, the spin down states are gapped with a gap of about 49 meV, however the spin up states only feature a negligibly small gap. Thus, according to this calculation the spin-polarized zGNR, that is AB stacked on graphene, is half metallic, *i.e.* conductive for spin up states but not for spin down states.

2.3.2 Experimental results of graphene zigzag nanoribbons

Several experimental works have examined nano-structures with zigzag edges and have claimed that they observe spin polarized edge-states. However, the experimental evidences are not conclusive enough, thus warranting further studies. The various reasons for that are, for example, the lack of atomic precision of the edge shape, information on edge termination or measurements of decay character or width dependence of the states, etc. Moreover, some of them do not report reproducibility of their data with others obtained in many similar nanostructures.

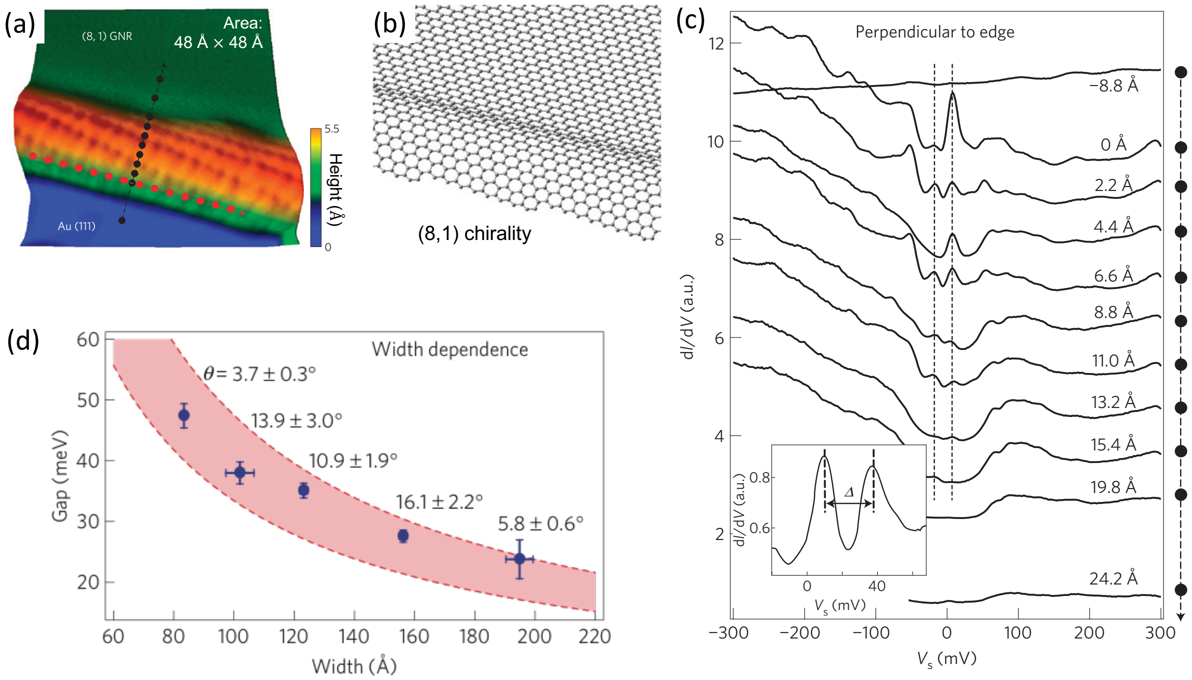

Figure 2.22: (a) STM image of an (8,1) chiral nanoribbon with $W = 15.6 \pm 0.1$ nm on Au(111) and (b) schematic of the same zGNR section. (c) STS result across the edge, on the black dots shown in (a). The inset shows the edge spectrum at a (5,2) chiral nanoribbon with $W = 15.6 \pm 0.1$ nm. (d) $\mathrm{d}I/\mathrm{d}V$ peak separation (gap) at the edges of different nanoribbons, angles refer to the nanoribbon edge directions with respect to the zigzag-direction. Shaded region shows calculated spin gap for nanoribbons with angles $0° < \theta < 15°$. Measurements at $T = 7$ K. Reprinted by permission from Springer Nature: Nature Physics "Spatially resolving edge states of chiral graphene nanoribbons", Chenggang Tao, *et al.*, (2010) [23].

Tao *et al.* [23] reported a STM/STS studies on nanoribbons with chiral edges obtained by unzipping carbon nanotubes that showed a width dependent edge state peak separation. The samples were fabricated via oxidation at 500° and sonification of carbon nanotubes in an organic solution, which mechanically 'unzipped' them. Afterwards, they were transferred to an Au(111) substrate. The nanoribbons usually did not posses pure zigzag edges, but chiral edges, which consist of a mixture of zigzag and armchair edge segments, as explained in the previous Section 2.3.1. Figures 2.22(a)-(c) show the results on a nanoribbon of width $W = 15.6 \pm 0.1$ nm and a (8,1) chiral edge (8 zigzag, followed by 1 armchair edge site, schematically shown in (b)), thus the nanoribbon possesses zigzag-rich edges. The nanoribbon is considered to be curved and floated near the edges (see (a)(b)), which may indicate strong interaction of the edge with the substrate. STS across the nanoribbon edge, in (c), reveals mainly two $\mathrm{d}I/\mathrm{d}V$ peaks, and outside of the curved region these peaks appear only faintly. It is not clear if the peaks stem from hybridization of graphene and Au(111), or from a graphene edge state. They also probed other nanoribbons with different widths and obtained multi-peak spectra at the edges for $W < 20$ nm. From this, the peak separation was found to be inversely proportional to W, as shown in (d). The peak splitting for different W in (d), which the authors called a 'gap', was compared with the calculated gap due to spin-polarization in Ref. [31]. Though the peak separations on different W are consistent with the calcula-

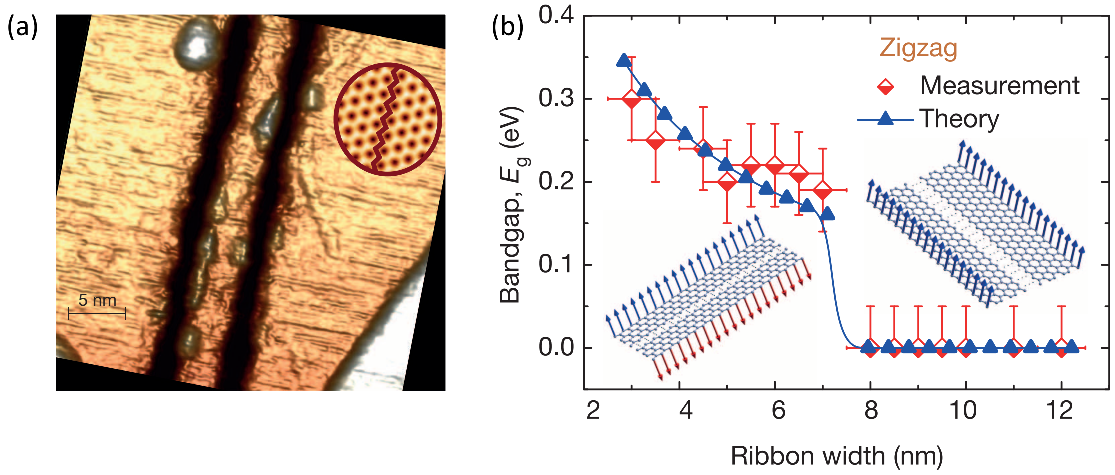

Figure 2.23: (a) STM image of a graphene nanoribbon with zigzag-direction edges and width $W = 6.5$ nm on Au(111). (b) Band gap obtained on such nanoribbons with different W by tunneling I-V measurements, and calculated band gap on spin-polarized zGNRs. Measurements were made at room temperature. Reprinted by permission from Springer Nature: Nature "Room-temperature magnetic order on zigzag edges of narrow graphene nanoribbons", Gábor Zsolt Magda, *et al.*, (2014) [21].

tions of spin-polarized nanoribbons, the unknown edge termination make it necessary to clarify the properties of zGNR edge states in a new study that avoids these difficulties.

Another possible indication of spin-polarization was obtained from spectroscopy measurement on zGNRs prepared by using the STM tip with a high applied V to cut graphene on a Au(111) substrate [21]. An example of the STM image is shown in Fig. 2.23(a). By the same method, armchair nanoribbons were also fabricated. At room temperatures, the STM tip was held at constant height above the nanoribbon centers while sweeping V and measuring the tunneling current (I). On zigzag nanoribbons, a band gap was observed that decreases in size with the ribbon width (W) until no gap was measured for $W > 7$ nm as shown in Fig. 2.23(b). This transition related to W was not observed on armchair nanoribbons. The figure also shows band gap calculations, which used a mean field Hubbard model. The calculations are consistent with the measured W-dependence of the gap and the transition between the capful and gapless states. However, while this result is suggestive, it does not directly show any edge state properties like the localized nature of the edge. Furthermore, only the direction of the nanoribbon edges was controlled. The atomic edge structure appears significantly disordered.

So far, the discussed zGNRs were those fabricated by the so-called top-down method. Instead, the zGNRs (1.1 nm width) in the study by Ruffieux *et al.* [22] were synthesized via a bottom-up method and deposited on a Au(111) with insulating NaCl monolayer islands (see Figs. 2.24(a)-(d)). The dI/dV of the zGNRs could be probed on two substrates, the insulating NaCl islands and Au(111), in (a). On the NaCl islands several dI/dV peaks surrounding the Fermi energy were obtained, as shown in (b). Only the surface states of the substrate were observed on Au(111), shown in (c). The multi-peak dI/dV spectrum on NaCl may consist of three peaks, although the third one is not clearly observed. The authors found consistency between the experimental results and

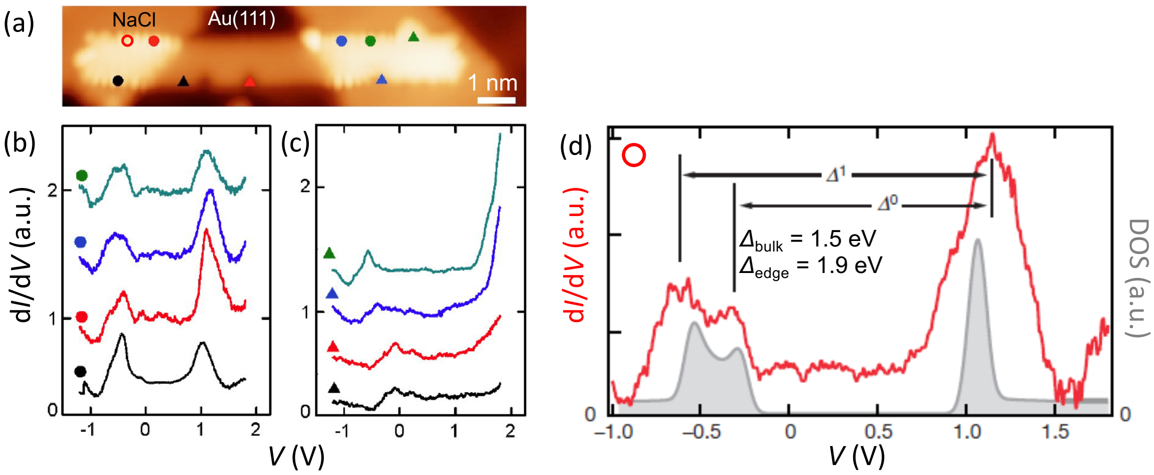

Figure 2.24: (a) STM image of a zGNR on Au(111) and NaCl monolayer islands. dI/dV spectra taken at the (b) colored dots, (c) triangles, (d) circle. (d) also includes calculated DOS at a spin-polarized graphene zigzag edge. Measurements at $T = 7$ K. Reprinted by permission from Springer Nature: Nature ”On-surface synthesis of graphene nanoribbons with zigzag edge topology”, Pascal Ruffieux, *et al.*, (2016) [22].

a calculated spectrum for a spin-polarized zigzag edge state. The calculation used the GW approximation (using Green's function and assuming screened interaction) of the many-body perturbation theory, which yielded a better fit than mean-field calculations. The synthesized zGNRs in this study have well controlled zigzag edges, however a drawback of this method is that only a single zGNR width can be obtained. Thus the width dependence, expected for spin-polarized edge states, cannot be confirmed. Furthermore, no spatial distribution was shown, which could differentiate states of the sample edge and bulk. The absence of edge states on edges on the Au(111) substrate in this study is in severe contradiction with the results presented in Refs. [21, 23], which were also obtained on Au(111) substrates, and even with the theory [30].

2.4 Hydrogen Plasma Etching

One of the main difficulties in studying zigzag edge states is obtaining clean and versatile graphene zigzag edges, as discussed in the previous section. These difficulties were recently overcome by the development of a method based on anisotropic etching by hydrogen plasma (H-plasma), which can produce highly accurate zigzag edges with known edge termination [24–29]. This is used to prepare the samples in this work. Additionally, such an etching technique is of special interest, because it can produce clean zigzag edges on pre-patterned structures with less controlled edges [24]. Etching occurs due to chemisorption of H-radicals in the H-plasma. These can form covalent bonds with C-atoms of graphene at surface defects. Afterwards, the remaining C-C bonds of a hydrogenated C-atom can be broken by other H-radicals. The stability of the C-C bonds depends on the configuration of the edge atom and differs on zigzag and armchair edges, this gives rise to the etching anisotropy [24, 25]. The etching product is probably methane [87]. Several studies investigated etching of graphene by hydrogen plasma. The H-plasma etching parameters are summarized in table 2.1. This includes the results by our group, by Matsui *et. al.* [28], which were used in the present work, and is shown to provide an overview of the different published techniques.

Table 2.1: Summary of studies of H-plasma etching of graphene. The technique used in this work is the same as that in Ref. [28]. In all cases a frequency f_{RF} = 13.56 kHz was used to generate the plasma.

Summary of studies of H-plasma etching of graphene

Work		Sample	T (°C)	P (Pa)	W_{RF} (W)	t (min)
Xie *et. al*	[25]	Graphene/Si	300	40	20	60
Yang *et. al*	[24]	Graphite, Graphene/SiO_2	200-700	∼45	50, 100	20-120
Diankov *et. al*	[26]	Graphene/SiO_2	500	∼53	20	10
Hug *et. al*	[27]	Graphene/SiO_2	200-600	40-170	30	≥60
Matsui *et. al*	[28]	Graphite, Graphene/SiO_2	200-700	13-590	10-50	20-60

Xie *et. al* [25] found that exposing graphene to H-plasma under certain conditions selectively etches the edges, while leaving the terraces pristine. The termination of graphene nanoribbons on Au(111) was studied after the same H-plasma treatment [29]. For this study, chiral nanoribbons were first prepared by unzipping carbon nanotubes in an organic solution by sonification [88]. After 15 min exposure to H-plasma, it was found by STM that the nanoribbon widths decreased and zigzag, armchair and chiral edges were formed. However, zigzag edges were apparently not preferentially created. The edge type only depended on the original direction of the nanoribbons. Comparisons of first-principles LDOS calculations of the thermodynamically favorable structures in the presence of hydrogen to the STM images are shown in Fig. 2.25. Simulations of zigzag, chiral and armchair edges passivated by a single hydrogen atom, shown in Fig. 2.25(f)-(h), yield good agreement with the STM measurements (c)-(e). In Fig. 2.25(i), the calculated energy of zigzag edge termination by a one and two hydrogen atoms is shown at different chemical potentials of hydrogen μ_{H}. The STM images of graphene show that μ_{H} remains below the threshold to hybridize with the bulk terrace during the H-plasma treatment ($\mu_{\mathrm{H}} < -0.2$ eV). In this range, termination by a single hydrogen per edge atom is most stable according to the calculation (this is also the case for armchair and chiral edges). Thus, the H-plasma etching seems to produce single hydrogen edge terminations.

Yang *et. al* [24] confirmed that the preferential etching inside graphene layers can produce hexagonal nanopits with edges aligned in the zigzag directions of the graphene lattice. The etching rate is similar on multi-layer graphene and graphite, but it is increased on monolayer graphene [24, 25, 27]. Etching may be faster on single layers because of an increased roughness that can be induced in graphene by the substrate. This would provide a higher defect density that serve as nucleation points for nanopit growth. Nevertheless, on both the single-and multi-layer graphene samples anisotropic step-edges were obtained, that posses the monatomic height of a single graphene layer.

However, the study by G. Diankov *et. al* [26] found that the same H-plasma etching conditions that etch multi-layer graphene anisotropically, can etch single-layer graphene

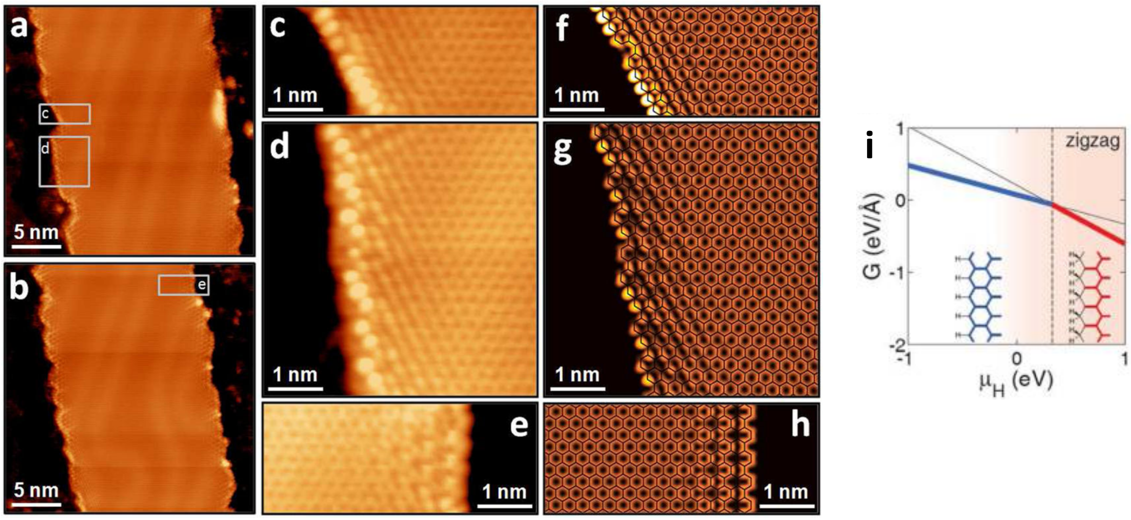

Figure 2.25: (a)-(e) STM images at room temperature of nanoribbons on Au(111) after H-plasma treatment. (c)-(e) are higher resolution images at areas indicated in (a)(b). (f)(g) show simulated LDOS from first-principles calculations on the edge shapes of (c)-(e), respectively. The STM parameters are $V = -0.97$ V, $I = 0.05$ nA. (i) Calculated graphene zigzag edge formation energy per unit length versus chemical potential of hydrogen (μ_{H}) calculated from first principles. Blue/red line marks the range where termination by one/two hydrogen per edge atom is more stable. In the shaded range graphane is more stable then graphene. Reprinted with permission from Zhang *et al.* [29]. Copyright 2013 American Chemical Society.

isotropically. In that case, round graphene nanopits with mixed zigzag and armchair edges were created on top of SiO_2, instead of hexagonal nanopits. The reason that etching occurs differently on single and multi-layer graphene in this study is unclear.

The work by Hug *et al.* [27] and that by Matsui *et al.* [28] independently and concurrently studied the parameter dependencies of the etching process and reached consistent conclusions. The latter study was conducted in our laboratory with the same etching technique used in this work, thus it will be discussed in the following chapter.

Chapter 3

Experimental

In this work three different types of samples were studied, namely graphite (HOPG and Kish graphite), epitaxially grown multi-layer graphene on SiC($000\bar{1}$) (abbreviated as graphene/SiC($000\bar{1}$)) and epitaxially grown single-and bilayer graphene on SiC(0001) (abbreviated as graphene/SiC(0001)). The preparation of the samples is described in Section 3.1. All samples were treated by anisotropic hydrogen plasma etching to create hexagonal nanopits with zigzag edges of monatomic height. The samples were probed by Scanning Tunneling Microscopy and Spectroscopy (STM/STS) at low temperatures. The STM/STS measurement system is discussed in Section 3.2.

3.1 Hydrogen Plasma Etching

3.1.1 Sample preparation technique

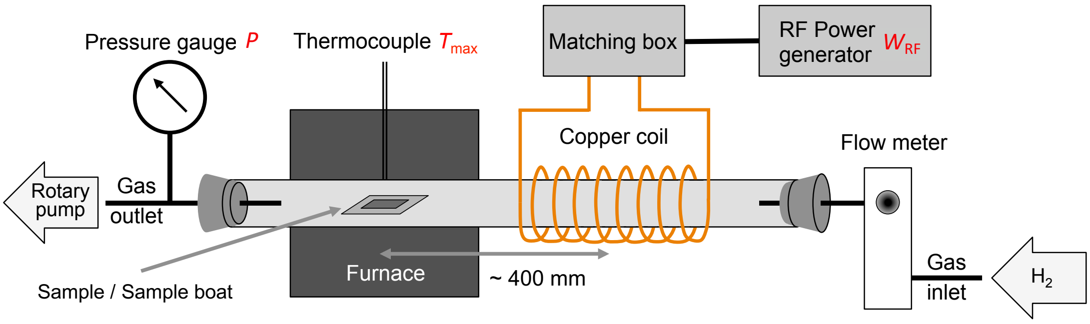

Figure 3.1: Schematic view of the hydrogen plasma etching setup [28, 89, 90].

The plasma etching apparatus is schematically shown in Fig. 3.1 [28, 89, 90]. The etching occurs inside a quartz tube with an inner diameter of 42 mm, an outer diameter of 45 mm, and a length of 1200 mm. The tube is connected to a gas inlet with a gas flow meter on one side and to a rotary pump on the other side. During the etching, gas flows into the tube through the inlet, flows through the length of the tube, and is evacuated on the other end by the rotary pump [91]. The direction of the gas flow is thus from right to left in Fig. 3.1. While gas flows through the quartz tube it passes first through a copper radio frequency (RF) coil and then through a furnace [92], which surround the

Table 3.1: Summary of etching processes and etching parameters used to prepare the samples studied in this work. All etching processes were performed by H-plasma, except for HOPG P110, which was initially etched by O-plasma. Subsequent etching processes on the same sample were performed without removing it from the vacuum.

Graphite samples

Sample ID	T (°C)	P (Pa)	W_{RF} (W)	t (min)	Comment
HOPG-P18	600	110	20	50	
HOPG-P33	600	110	20	50	
Kish-P40	600	110	20	50	
HOPG-P65	600	11	20	15	Lower P
	600	220	20	30	Higher P
HOPG-P79	600	110	20	10	with 120710-2-1
HOPG-P110	30	110	30	3	O-plasma
	600	110	20	40	
HOPG-P123	600	110	20	10	with G1213

Few-layer epitaxial graphene on SiC(000$\bar{1}$) samples

Sample ID	T (°C)	P (Pa)	W_{RF} (W)	t (min)	Comment
G1212	600	110	20	30	in append. B.1
G1213	600	110	20	10	

Epitaxial graphene on SiC(0001) samples

Sample ID	T (°C)	P (Pa)	W_{RF} (W)	t (min)	Comment
120710-2-1	600	110	20	10	

tube and have a center-to-center distance of 400 mm along the tube length. The copper RF coil, with a wire diameter of 3.5 mm, possesses 15 windings with a coil diameter of 50 mm and a coil length of 300 mm. It is connected to a matching box and a RF generator. The RF generator [93] with a power output of W_{RF} produces an alternating electronic field with a frequency $f_{\mathrm{RF}} = 13.56$ MHz, which is applied to the H_2 gas. The matching box [94] is connected in series between the RF generator and the copper coil to match the impedances and maximize the power transfer between the two.

The sample is inserted into the quartz tube and positioned at the center of the furnace, then the closed tube is evacuated by the rotary pump until the pressure becomes stable below about 1 Pa. The furnace is heated to a temperature T over the course of one hour. After T is reached, H_2 gas is introduced, the inlet is adjusted to let the pressure at the sample position be P. After a few minutes, when the gas flow has stabilized, the RF power generator is activated to produce H-plasma during an exposure time t, which will be referred to as the etching time. When W_{RF} is turned on the H-plasma glow is confirmed visually. After etching, the gas flow is stopped and the quartz tube continues to be evacuated by the rotary pump until the temperature decreases to $T \approx 50$°C. The graphene and graphite samples studied in this work were prepared by H-plasma etching with different parameters, which are summarized in table 3.1.

3.1.2 Hydrogen plasma etching parameters

As mentioned earlier previous attempts to measure spin-polarization often failed to provide clear answers due to difficulties in fabricating clean samples. In a breakthrough development this laboratory succeeded in significantly improving reliable fabrication of graphene samples exhibiting precise zigzag edges (Sato *et al.* in 2015 [89]). The method, which is based on H-plasma etching, succeeded in identifying the critical parameters to create the create anisotropic features on graphene samples. This is a precondition for the study of zigzag edge states in the present work. Afterwards, the etching parameter space was further explored by Kita *et al.* [90]. A wider comprehensive study of the etching parameters, including earlier results, was made by Matsui *et al.* [28]. In that study, the etching parameters of the samples were chosen to optimize the zigzag edge fabrication. This is based on the etching parameter study, which is briefly discussed in the following.

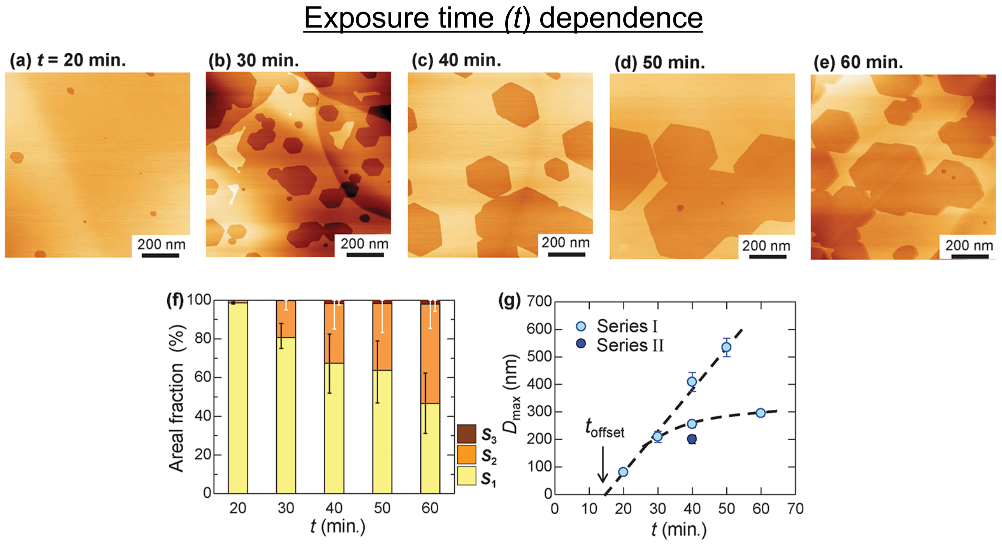

Figure 3.2: (a)-(e) STM images of graphite surfaces etched by H-plasma with different etching times and $P = 30$ Pa, $T = 600$ °C, and $W_{\mathrm{RF}} = 20$ W. (f) Areal fraction of the top layer (S_1), the second (S_2), and third layer (S_3) below that after etching with different t, extracted from STM images. (g) Maximum hexagonal nanopit diameter (D_{max}) after etching for different t. Reprinted with permission from T. Matsui, *et al.*, The Journal of Physical Chemistry C **123**, 22665 (2019). Copyright (2019) American Chemical Society [28].

The etching results on the surface of graphite after different exposure times t are shown in Fig. 3.2 [28]. At the chosen parameters hexagonal are formed. Their density and size was evaluated from the areal fraction of the second and third top layers (S_2 and S_3), which are exposed by nanopits in the upper layer, shown in (f). Furthermore, their size was evaluated by the maximum nanopit diameter (D_{max}), which is shown after different t in (g). At shorter etching times, D_{max} increases with t. However, for longer etching times it can be reduced, if sufficiently large nanopits completely remove the top layer. Thus, D_{max} can be expected to not increase significantly after a certain t. For

t larger than about 30 min D_{max} becomes scattered, which may depend on detailed sample and etching conditions that cannot be easily controlled. Nevertheless, there seems to exist a offset time t_{offset} of 10-15 min, marked in (g), before nanopit growth commences. In (f), it can be seen that there is an offset time of 30-40 min before nanopits in the third layer appear. This time delay during etching is suggestive of the nanopit formation mechanism. It may support the results of molecular dynamics simulations [95–97] that suggest that extended exposure to H-ions is necessary before covalent C-bonds are broken.

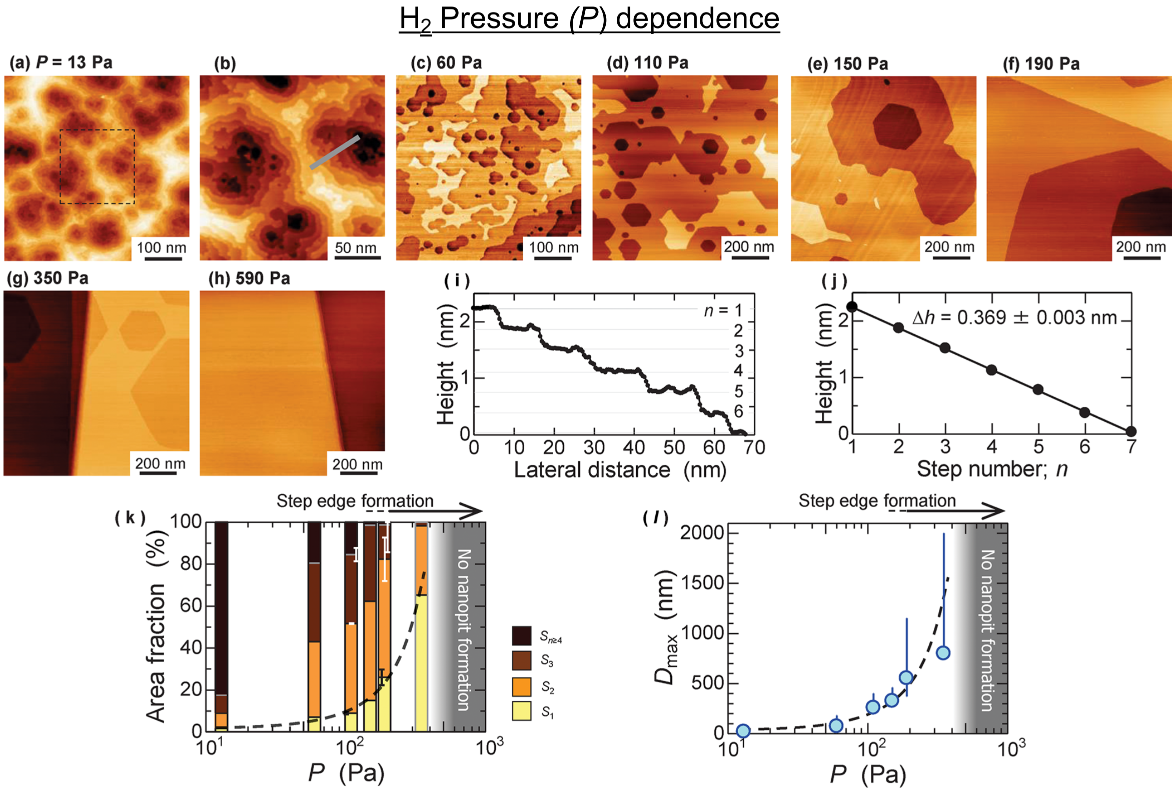

Figure 3.3: STM images of graphite surfaces etched by H-plasma at the indicated P and $T = 500$ °C, $t = 40$ min, and $W_{\mathrm{RF}} = 20$ W. (b) is a magnified image of the region indicated by the square in (a). (i) Cross sectional profile along the solid line in (b), and (j) relation between the terrace height and the step number showing that the nanopit steps are of monolayer height. (f) Areal fraction of the top layer (S_1), the second, third, or lower layer below that (S_2, S_3, $S_{\mathrm{n}\leq4}$) after etching with different P, extracted from STM images. (g) Maximum hexagonal nanopit diameter (D_{max}) after etching for different P. Reprinted with permission from T. Matsui, *et al.*, The Journal of Physical Chemistry C **123**, 22665 (2019). Copyright (2019) American Chemical Society [28].

Figure 3.3 shows STM results of etched graphite surfaces with progressively increased etching pressure P from 13 to 590 Pa [28]. By increasing P the etching nature changes from irregular isotropic to anisotropic etching and the number of nanopits decreases. Thus, at lower pressures round craters across many graphene layers are created (a)(b). The line profile across a crater created by low P, shown in (i), still shows the step-edges due to the graphene layers. (j) shows the height difference of the step-edges exposed by the etching, which have an average height of 0.369 ± 0.003 nm, thus they are monatomic layers. The STM height is calibrated from the known height of naturally existing graphite step edges. Figures (k) and (l) show the areal fractions of different layer and the D_{max}, respectively, similar as in Fig. 3.2. At low P, the first layer does almost not appear, but by increasing P beyond about 60 Pa etching within a single layer becomes dominant, thus the fraction of higher layers increases as well. Furthermore, the nanopit shape becomes more hexagonal, thus D_{max} of the hexagonal nanopits increases from about 0 nm at 13 Pa in (a)(b) to a maximum of about 600 nm at 350 Pa in (g). At the same time, the density of nanopits decreases, which results in a decrease of the areal fractions of lower terraces seen in (k). The decreased density indicates that nanopits are formed less frequently. The nanopits that are observed are likely created from the least stable graphene sites, such as initial defects. The increase of D_{max} is likely a consequence of the reduced nanopit formation. This is because the nanopits are formed at especially unstable graphene sites are likely created near the beginning of the etching process, thus increasing the average growth time. Moreover, the decreased density reduces the overlapping that would obscure large nanopits at lower P with higher nanopit densities. At higher P the nanopit formation does not appear to occur, for example no nanopits are observed in (h), which was etched at $P = 590$ Pa. Both the study in our laboratory and the one by Hug *et al.* [27] found consistent results of the etching dependence on P. The etching processes at different P are consistent with a model of a ”glow” and a ”remote” plasma mode [27, 28]. The glow mode, which includes the glowing region of the plasma, roughly represents the spatial extension of the different H-ions inside the plasma. Inside the glow mode the high-energy H-ions create defects on the graphene surface. At $P = 13$ Pa, the sample is well inside the glow mode, thus isotropic craters are formed that extend to deeper layers than is found at higher P. By increasing P of the plasma the glow mode region shrinks, because more frequent collisions reduce the life time of the H-ions, and the sample is exposed to a lower concentration of H-ions. Outside the glow mode, in the remote mode, lower-energy H-radicals are present, which are responsible for the anisotropic growth at defects in the bulk terrace. However, in this mode new defects, that can act as nuclei for nanopit growth, are not likely to be formed, thus no nanopits appeared in the STM image of graphite etched at $P = 590$ Pa (in (h)) [28]. At intermediate pressures (the results of $P = 60$ to 350 Pa are shown in (c)-(g)) both the anisotropic etching mechanism of the glow mode and the isotropic mechanism of the remote mode are at work. Thus, in this P range hexagonal nanopits are formed, whose number and size can be controlled by adjusting P.

The nanopit growth depends on the etching temperature T as well. The results with parameters $P = 110$ Pa, $t = 40$ min, $W_{\mathrm{RF}} = 20$ W are shown in Fig. 3.4 [28]. The STM images in (a)-(f) reveal that nanopits are created for $T > 200$ °C. Nanopit formation is suppressed at low T presumably because the thermal energy is insufficient for etching reactions to occur. The nanopits that appear at 300 °C in (b) are round, but their shape becomes more hexagonal at 400 °C in (c). For an increased T at 500 °C, shown in (d), the surface is drastically changed. The in-plane etching is purely anisotropic and forms fewer large hexagonal nanopits. By increasing T further the size of the hexagonal nanopits becomes smaller, as seen in (e)(f). At higher T the etching may be suppressed due to desorption of H from the surface before etching can occur [98], or due to the instability of the presumed product of the etching: CH_4 [87, 99]. The arial fraction of the different

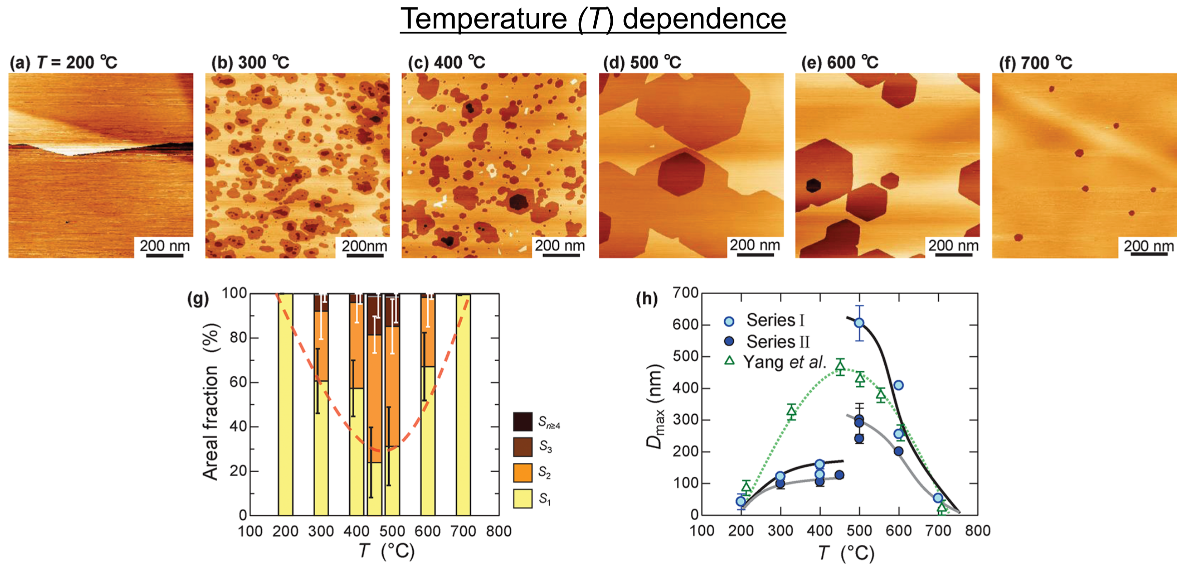

Figure 3.4: STM images of graphite surfaces etched by H-plasma at the indicated T and $P = 110$ Pa, $t = 40$ min, and $W_{\mathrm{RF}} = 20$ W. (g) Areal fraction of the top layer (S_1), the second, third, lower layers below that (S_2, S_3, $S_{\mathrm{n}\leq 4}$) after etching with different T, extracted from STM images. (h) Maximum hexagonal nanopit diameter ($D_{\max}$), including results by Yang *et al.* [24], after etching for different T. Reprinted with permission from T. Matsui, *et al.*, The Journal of Physical Chemistry C **123**, 22665 (2019). Copyright (2019) American Chemical Society [28].

layers in (g) indicate that deeper layers are exposed the most for $T \approx 450 - 500$ °C. This is also reflected in (h), which shows that $D_{\max}$ is largest at a similar range of T, however the $D_{\max}$ obtained in our laboratory showed a sudden transition by a factor of 2-3 in between $T \approx 450$ and 500 °C. This transition occurs only in $D_{\max}$ and is not reflected in the arial fractions of the second layer S_2 in (g). Thus, the total etched surface seems to change relatively smoothly with T, despite the observed transitional jump of $D_{\max}$. This indicates a strong suppression in the formation of new nanopits occurring between $T = 450$ and 500°C, for reasons that were discussed in the previous paragraph. In previous studies, such as ref. [24] shown in (h), such a transition of $D_{\max}$ was not observed.

To increase the density of nanopits it is possible to first create defects via an isotropic etching process. This can be done, for example, by H-plasma etching at lower P to etch graphene in the plasma glow mode, or by O-plasma etching, which also etches anisotropically. Both of these methods were used on certain graphite samples before the anisotropic H-plasma etching (details are shown in table 3.1). In Ref. [28], successive low P (LP, 13 Pa) and middle P (MP, 190 Pa) etching trials were investigated by STM, AFM and Raman spectroscopy. Raman spectroscopy measures the inelastic scattering of a monochromatic light source, which allows the determination of vibrational modes of different molecules. Graphene has several modes that feature as characteristic peaks in the Raman spectrum. The so-called the D band peak at a wavelength of about 1350 cm^{-1} only appears if there is interaction between the electronic states of the two graphene sublattices, thus it is observed if there are armchair edges, or lattice disorder,

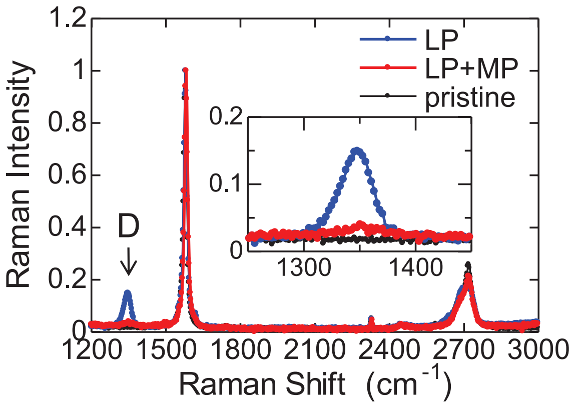

Figure 3.5: Raman spectroscopy on multilayer graphene flakes on SiO_2 that are: pristine, etched by H-plasma LP etching, etched by LP and then MP etching. LP etching parameters are $T = 600°C$, $W_{RF} = 20$ W, and for LP: $P = 13$ Pa, $t = 15$ min, for MP: $P = 190$ Pa, $t = 30$ min. The inset is a magnification of the spectra around the D band peak. Reprinted with permission from T. Matsui, *et al.*, The Journal of Physical Chemistry C **123**, 22665 (2019). Copyright (2019) American Chemical Society [28].

but it is not observed at zigzag edges. Therefore, the D peak indicates isotropic etching, its absence anisotropic etching. Since Raman spectroscopy can include larger areas than STM in a measurement, it is a useful tool to evaluate whether a high concentration of zigzag edges is presence on a graphene or graphite surface after etching. Figure 3.5 shows Raman spectra on two few-layer graphene flakes, that were exfoliated onto SiO_2 and etched by H-plasma at LP and successively at LP and MP, respectively [28]. The D band peak appears after LP etching, since the isotropic nanopits include many armchair edge segments. After LP+MP etching, the D peak is significantly reduced. This confirms that the anisotropic MP etching removes most armchair edges so that the surface is dominated by zigzag edges. STM images on graphite after LP+MP etching confirms that the density of hexagonal nanopits is increased compared to simple MP etching [90].

3.2 Scanning Tunneling Microscopy and Spectroscopy

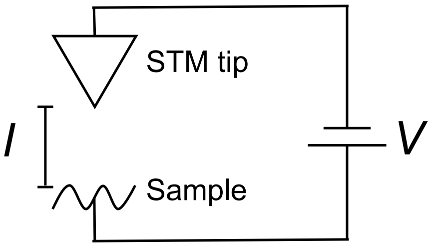

Figure 3.6: Schematic of a STM tip and sample between which a bias voltage V is applied and a tunneling current I flows.

The samples in this work are studied by Scanning Tunneling Microscopy (STM) and by Scanning Tunneling Spectroscopy (STS). To investigate the spatial dependence of electronic properties at the sample surface combined scanning tunneling microscopy and spectroscopy measurements are used (STM/STS). By STM/STS, both information of the sample topography and its LDOS can be obtained. This is done by applying the voltage V and controlling the tip height while measuring the tunneling current I between the STM tip and sample (see Fig. 3.6). I depends on the electronic states on the tip and sample at energies between the Fermi energy and $e \times V$ and on the tunneling probability between the two. Thus, it is proportional to the integral of $\rho_{\text{tip}} \times \rho_{\text{sample}}$ times the tip-sample transition probability T, which in turn is proportional to the tip-sample distance L (see eq. 3.1).

$$I \propto \int_{-\infty}^{\infty} [f_{\text{tip}}(E) - f_{\text{sample}}(E + eV)] \cdot \rho_{\text{sample}}(E + eV) \cdot \rho_{\text{tip}}(E) \cdot T(L) \ \mathrm{d}E \qquad (3.1)$$

Thus, if the electronic states on the tip and sample and the transition probability (ρ_{tip}, ρ_{sample}, and $T(L)$) are relatively constant, then I is only sensitive to L and it is possible to measure sample height with sub-angstrom precision. This allows STM measurements of the sample topography. Furthermore, if L is kept constant and the tip is chosen so that ρ_{tip} remains constant within the applied V, then sample LDOS ρ_{sample} becomes proportional to the derivative of I with respect to the voltage:

$$\frac{\mathrm{d}I}{\mathrm{d}V} \propto \rho_{\text{sample}}(E) \qquad (3.2)$$

By varying V at a constant L and measuring I the differential current $\mathrm{d}I/\mathrm{d}V$ is obtained, which can be used to measure the LDOS of the sample. This allows tunneling spectroscopy measurements to probe the electronic properties of the sample surface. Before each measurement at one position, L is determined by setting a certain I at an applied V. This is done before each point measurement, because L gradually drifts and the sample height itself can vary at different positions. From the I-V data the gradient can be numerically extracted to yield $\mathrm{d}I/\mathrm{d}V$. However, a higher energy resolution can often be obtained with a so-called AC method, which is used for the tunneling spectroscopy measurements in this work. $\mathrm{d}I/\mathrm{d}V$ is measured during a step-wise V sweep across the measurement voltage range while applying a modification voltage V_{mod} with frequency $f_{\text{mod}} = 1.2343$ kHz. When a step of V is reached and a delay time has passed, then the I is measured for a certain acquisition time by a lock-on method that detects signals with the same frequency as f_{mod}. After the delay time and acquisition time have passed V is swept to the next predetermined step. The measured difference of I at the opposite amplitudes of a relatively small V_{mod} is used to linearly approximate $\mathrm{d}I/\mathrm{d}V$ as $\Delta I/V_{\text{mod}}$ at different values of V. The value of V_{mod} is usually chosen so that the linear approximations of $\mathrm{d}I/\mathrm{d}V$ cover the whole sweeping range of V. By choosing a sufficiently small V_{mod}, the energy resolution is mainly limited by thermal noise (at $T = 78$ K: ≈ 6.7 mV, at $T = 4$ K: ≈ 3.4 mV). STS measurements, including both sample height and $\mathrm{d}I/\mathrm{d}V$, usually include multiple measurements along lines that are either at identical positions or removed from each ether by small intervals. To reduce random noise, often the data of consecutive scans are averaged. However, especially for STS at $T = 78$ K, the thermal drift is sufficient to gradually shift the X-Y position of the STM tip relative to the sample between measurement lines during the data acquisition time. To correct the error due to lateral drift the position coordinates are shifted when necessary, and an average of the shifted height and dI/dV values was calculated (see appendix A).The STM/STS data is analyzed using original programs, as well as the free-to-use software WSxM [100].

In this work, a STM head manufactured by UNISOK Co., Ltd. was operated by a commercial controller (model SMP100, RHK Technology, Inc.) at room temperature and atmospheric conditions (RT-STM). A different machine was used to take STM/STS measurements at lower temperatures (60 mK $\leq T \leq$ 78 K). These were taken by a home-made ultra-low temperature multi-functional scanning probe microscope (ULT-SPM) [101]. The cooling system is based on a 3He-4He dilution refrigerator (Kelvinox-100, Oxford Instruments). The SPM head was also specially manufactured by UNISOK CO.,LTD. and was operated by a commercial controller (VME Workstation from OMICRON Vakuumphysik GmbH with software SCALA). This system originally used the STM head, which is currently used in the RT-STM, and was described in Ref. [101]. Now, the STM head was exchanged with the SPM head. The upgrade of the ULT-STM to a ULT-SPM system was described in Ref. [102]. The ULT-SPM was used for measurements below room temperatures, including all STS measurements in this work. STM tips made of W and PtIr were used and no difference between the results obtained by the

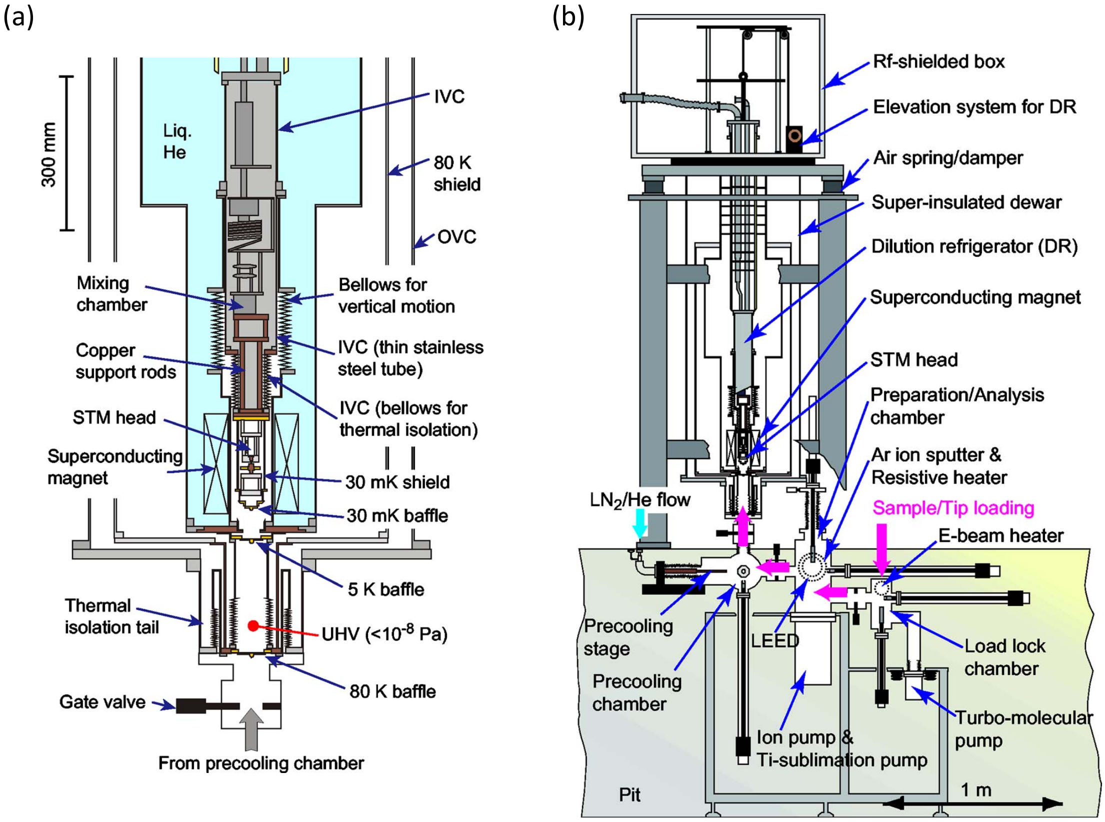

Figure 3.7: Diagrams of the ULT-SPM system (formerly a STM head was installed, as shown here, which has been replaced by a multi-functional SPM head). (a) experimental chamber, dilution refrigerator and bath are shown. (b) a wider region is shown, including all four UHV chambers and the part shown in (a). Figures were published in Ref. [101].

different materials was found. The SPM head is designed to take STM/STS, AFM and transport measurements. However, in this work only STM/STS capabilities are used, except that the transport capability was used to soft anneal the epitaxial graphene on SiC samples in vacuum via a tungsten filament installed on the sample holder below the sample. The ULT-SPM system is schematically shown in Fig. 3.7. It is designed to take measurements under three extreme conditions simultaneously: in ultra-high vacuum (UHV, $P < 10^{-8}$ Pa), at ultra-low temperatures (ULT, $T \geq 60$ mK), and in high magnetic fields ($B \leq 13$ T). It includes four vacuum chambers that are shown in Fig. 3.7(a), between which samples and STM tips can be transferred in sequence through gate valves via transfer rods (see the magenta arrows in Fig. 3.7(b)). The Load lock chamber is used to insert and extract samples and STM tips into the vacuum. Next, they are transferred into the main chamber, in which the epitaxial samples were annealed via a transport stage that uses leads on the sample holders. After transfer into the Precooling chamber, where in this work samples and tips were pre-cooled by liquid Nitrogen, they are transferred into the Experimental chamber to the SPM head. As shown in Fig. 3.7, flexible welded bellows are used to connect the RT and ULT parts, thereby reducing the thermal conduction. By taking STS measurements over longer times at lower temperatures the drift of the STM tip position during the measurement is reduced. Magnetic fields can be applied via the superconducting magnet surrounding the SPM head in the bath.

Chapter 4

Results on H-plasma Etched Graphite Surface

The contents of this chapter will be published elsewhere, the chapter will be made available in three years.

本章については、３年以内に雑誌等で刊行予定のため、現在非公開。

Chapter 5

Results on H-plasma Etched Graphene/SiC($000\overline{1}$)

The contents of this chapter will be published elsewhere, the chapter will be made available in three years.

本章については、３年以内に雑誌等で刊行予定のため、現在非公開。

Chapter 6

Results on H-plasma Etched Graphene/SiC(0001)

On graphene/SiC(0001), unpassivated Si bonds on the substrate surface interact strongly with epitaxial layers and strongly modifying their electronic properties. Thus, the edge states can be expected to be changed, and the study of them on this sample may yield new insights. The monolayer graphene/SiC(0001) sample fabrication and hydrogen plasma (H-plasma) etching is explained in Section 6.1. After etching, the sample was probed via STM/STS. In addition to the expected nanopits, elevated terraces were created as well. Measurements of these elevated terraces are discussed in Section 6.2. Results of the nanopits formed by the etching are discussed in Section 6.3. Section 6.4 summarized Chapter 6.

6.1 Sample Preparation

The single-layer graphene sample (sample ID 120710-2-1) was epitaxially grown on 4H-SiC(0001) by H. Hibino at NTT laboratories. Different from graphene grown on the C-face, on the Si-face the first layer of C-atoms is partly bonded to the substrate, producing the so-called buffer layer. Furthermore, more even layer growth and no rotational defects between epitaxial graphene layers is obtained. The number of layers was checked by atomic force microscopy image phase contrast by H. Hibino as well. Before H-plasma etching, we probed the sample by STM. To remove adsorbates before STM measurements, the sample was heated in UHV by a W-filament at $< 600°\text{C}$ for 5 min on the STM sample holder. A (6×6) lattice was observed that is expected for graphene/SiC(0001) [50]. Additionally, a few deep crevices with several tens of nm length were observed. The sample was etched for 10 min using the parameters optimized for creating zigzag edges on graphite ($T = 600°\text{C}$, $P_{\text{H}} = 110$ Pa, $W_{\text{RF}} = 20$ W) the etching parameters are identical to those used for the epitaxial C-face sample G1213 (all parameters are shown in Table 3.1).

6.2 Elevated Terraces on the Etched Sample

After etching, STM images taken at $T = 78$ K revealed that the sample surface was significantly modified. Nanopits of monatomic depth were created. These are partly hexagonal nanopits, including some well-defined hexagonal shapes aligned in zigzag directions, as well as mixed zigzag and armchair edges, as in the case of etching graphene/SiC(000$\bar{1}$) with the same parameters. Furthermore, elevated, smooth terraces with irregular boundaries, with a height of 0.12 ± 0.03 nm, that is less than that of a graphene layer, were obtained on more than half of the sample surface. Figure 6.1 shows a STM image of an area on the boundary between the elevated and non-elevated areas. As shown in (a) and (c), the elevated regions are smoother than the lower ones, this is also clear in the height profile of (b). The magnified image of the boundary reveals that the atomic corrugation continues across the boundary, showing that both elevated and non-elevated terraces are covered by the same graphene sheet, as shown in (c).

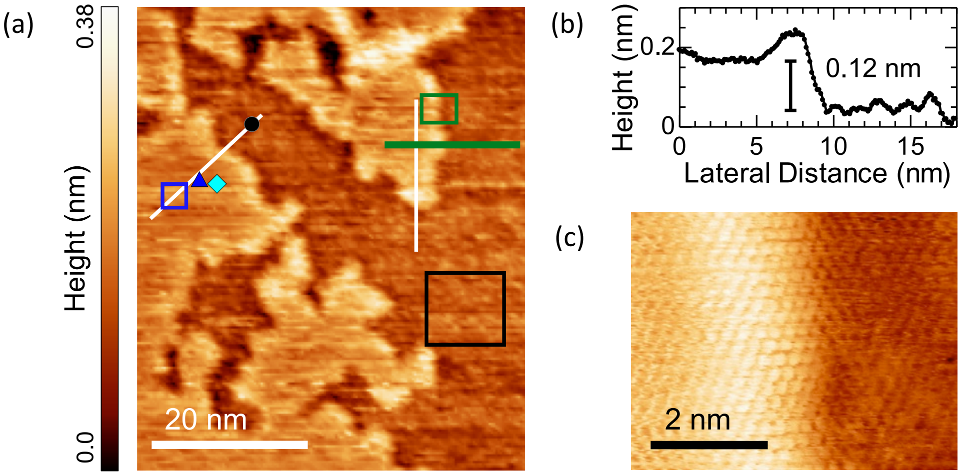

Figure 6.1: (a) STM image of graphene/SiC(0001) at $T = 78$ K (sample 120710-2-1). (b) Height profile along the green line in (a). (c) STM image of the area in the green rectangle in (a) with greater magnification. Additional lines, rectangles and symbols in (a) refer to measurements shown in Figs. 6.2 and 6.3. The STM measurement parameters are $V =$ (a) 500 mV, (b)(c) 250 mV, and $I =$ (a) 0.05 nA, (b)(c) 0.06 nA. Copyright 2019 The Japan Society of Applied Physics [117].

Atomically resolved STM images and STS results on the elevated and the lower terraces is shown in Figs. 6.2(a)-(d). On the lower terrace in (a), a hexagonal atomic lattice and the (6×6) corrugation is clearly observed, as on the sample before etching, which stems from the $(6\sqrt{3} \times 6\sqrt{3})R30°$ lattice of the buffer layer. The $\mathrm{d}I/\mathrm{d}V$ spectrum on the lower terrace in (b) features an asymmetric spectrum with respect to the Fermi energy, with lower $\mathrm{d}I/\mathrm{d}V$, at negative V. This is probably due to the strong n-type doping by the and buffer layer, which was present before etching as well. Such tunnel spectrum is expected on graphene/SiC(0001) and similar to published results, one of which [56] is shown in Fig. 6.2(b). The STM image of the elevated terrace in (c) shows one sublattice much clearer than the other, and the (6×6) lattice does not appear. By

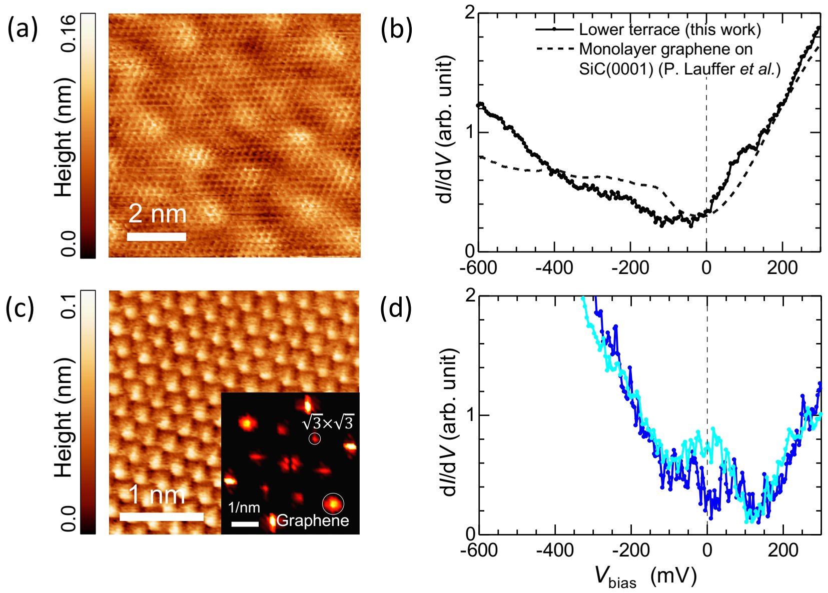

Figure 6.2: STM/STS measurements (at $T = 78$ K) on the etched graphene/SiC(0001) (a)(b) elevated and (c)(d) lower terraces. (a)(c) STM images from the positions of the rectangles indicated in Fig. 6.1(a), the FFT of (c) is included as an inset. (b)(d) $\mathrm{d}I/\mathrm{d}V$ spectra from the positions of the symbols with matching color drawn in Fig. 6.1(a). For comparison, (b) includes a published result from Ref. [56]. The STM/STS parameters are $V =$ (a) 500 mV, (c) 300 mV, $I =$ (a) 0.05 nA, (c) 0.06 nA, and $V_{\text{mod}} =$ (b)(d) 3 mV. V_{bias} is identical with the bias voltage V. Copyright 2019 The Japan Society of Applied Physics [117].

Fast Fourier Transform (FFT) a superlattice with a $(\sqrt{3} \times \sqrt{3})$ unit cell was revealed instead, as shown in the inset of (c). A different type of tunnel spectrum is obtained on the elevated terrace in (d). The dispersion is more symmetric, indicating that doping was reduced and that the Dirac point is closer to $V = 0$. In a range of about $-100 \leq V \leq 100$, the dispersion is relatively low, whereas is is much higher at larger values of $|V|$, which could indicate an electronic gap. Since the (6×6) corrugation is absent on the elevated terrace, but a triangular lattice was obtained, it seems that two AB stacked layers are present instead of one graphene layer, which was there before etching. The gap-like LDOS feature can be formed on bilayer graphene due to the electrostatic potential of the substrate, thus it is consistent with a two-layers being present.

To obtain two graphene layer in the elevated regions, the former buffer layer must be decoupled from the substrate before forming an additional graphene layer. In that case the dangling Si-bonds must have been passivated by hydrogen atoms during the H-plasma etching. As a result, bilayer quasi-free-standing (qFS) graphene was created. This is known to occur during atomic H treatment of Graphene/SiC(0001) (see Section 2.1.3) and the elevation height, as well as the other features obtained here are consistent with published results [62, 118].

On the qFS bilayer, the spectra feature several peaks near $V = 0$ inside the gapped region, which depend on position, but usually remain constant within distances of about 10 nm, as seen in the next figure (6.3). Such $\mathrm{d}I/\mathrm{d}V$ peaks near $V = 0$, as well as the $(\sqrt{3} \times \sqrt{3})$ pattern that is often observed indicate the presence of localized defect states [14, 69]. Defect states may originate from an inhomogeneous distribution of defects or dangling bonds below the sample, since nothing is directly observed by STM they cannot be present on the surface layer. On single qFS graphene with strong p-type doping, clusters of dangling Si bonds on the substrate, that are not passivated by H, can induce defect states that do appear in STM images [119]. On the other hand, in the present study, the doping on the qFS graphene is weaker and no clusters were observed by STM. It should be noted that our sample became bilayer graphene after etching, thus the STM signature of such clusters may not be observable on the surface. However, the observed weaker doping, compared to published data, is consistent with an incomplete passivation of dangling bonds. Furthermore, the presence of dangling bonds is in term consistent with defect states that are indicated by the tunnel spectra. The qFS terraces thus feature an incomplete substrate passivation with some dangling bonds below bilayer graphene.

Figure 6.3 shows STM/STS results along lines that cross from the elevated to the lower terraces. Changes of the dI/dV similarly to Fig. 6.3 are typically observed across the boundary of these two terraces. Close to the boundary (near distance $x = 0$ nm) from elevated to lower terrace, the dI/dV spectra change from the more symmetric one with small peaks near the Fermi energy to the strongly asymmetric one without peaks. This shows that weak doping and defect state peaks appear specifically on the elevated, and n-type doping on the lower terrace. However, at the location of the data in Fig. 6.3(c) and (d), across a peninsular shaped elevated region, the transition of the dI/dV spectrum follows the topographic change less closely. Instead, an intermediate region exist between $0 \leq x \leq 3$ nm in which the spectrum changes gradually. Thus, the morphology of the elevated terrace and the electronic structure of the lower one are obtained on this special region.

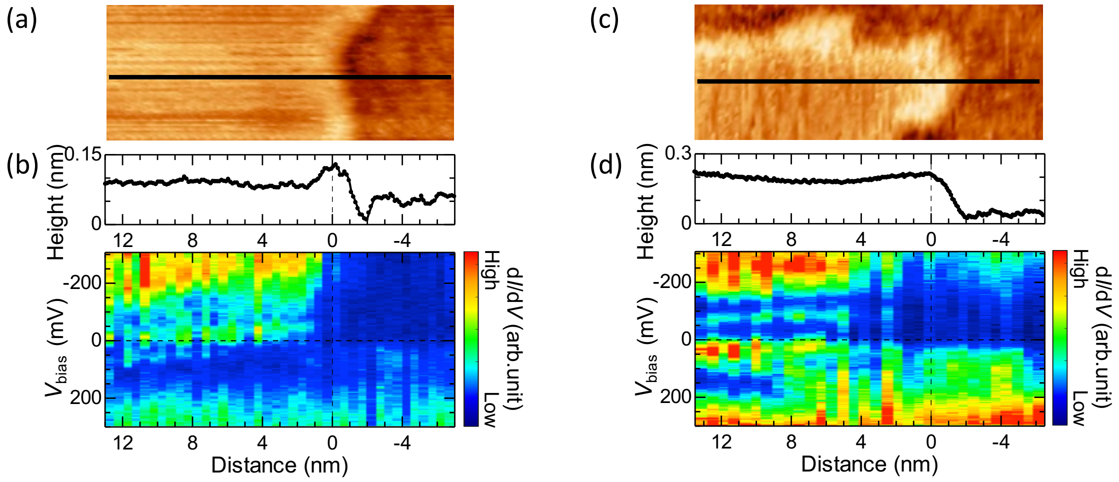

Figure 6.3: STM/STS measurements (at $T = 78$ K) on the etched graphene/SiC(0001). (a)(c) STM image, (b)(d) height profile and dI/dV colormap across the boundary of the elevated and lower terraces. (a)(b) are taken along the diagonal and (c)(d) along the vertical white line in Fig. 6.1(a). The STM/STS parameters are $V =$ (a)(c)(d) 300 mV, (b) STM: 300 mV, (b) STS: 500 mV, $I = 0.06$ nA, and $V_{\mathrm{mod}} = 5$ mV. Copyright 2019 The Japan Society of Applied Physics [117].

On this sample regions with incomplete intercalation were obtained, such as the ones shown here, as well as regions with uniform intercalation or no intercalation. On the opposing sides of a substrate edge, often different types of intercalation appeared, indicating that substrate steps hinder the propagation of H below the surface, an example is shown later (Fig. 6.5(a)).

6.3 Nanopits on the Etched Sample

H-plasma etching was successful in creating hexagonal nanopits with zigzag edges on the graphene/SiC(0001) sample. Figure 6.4 shows nanopits that were formed on the epitaxial graphene (a)-(c) and on graphite (d)-(f), etched at the same time. The epitaxial graphene surface shown in Fig. 6.4(a) consists mostly of elevated, qFS graphene terraces. The presence of small, enclosed lower regions make the surface morphology rough. The nanopits on graphene/SiC(0001) have a larger maximum diameter (about 50 nm) and a higher density than on graphite. It suggests that on mono-layer graphene there are more defects, resulting in earlier nanopit formation during the etching process, which is consistent with published studies of anisotropic etching of mono-and few-layer graphene by H-plasma [24, 26]. However, they are often less hexagonal than nanopits of the same size obtained on graphite (*e.g.* the left-hand nanopit in Fig. 6.5(a)). This is similar to the results on graphene/SiC(000$\bar{1}$), shown in Section 5.2.2.

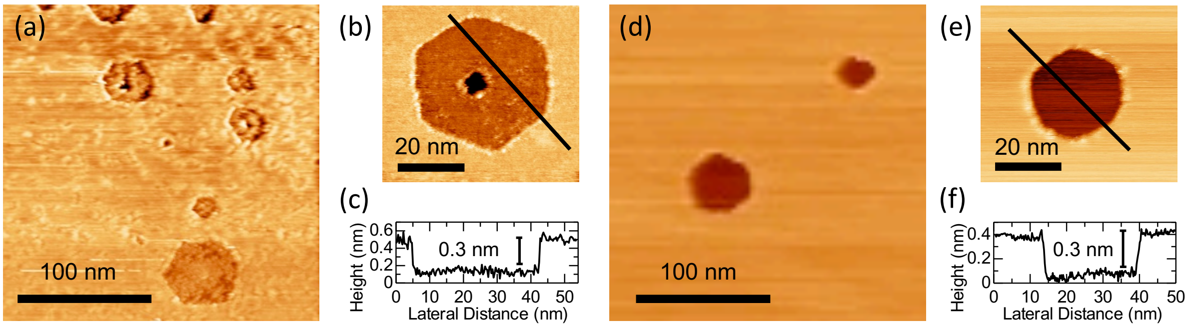

Figure 6.4: (a)(b)/(d)(e) STM images (taken at $T = 78$ K) and (c)/(f) height profile, along the line indicated in (b)/(e), of hexagonal nanopits on graphene/SiC(0001) (sample 120710-2-1) / graphite etched at the same time (sample HOPG-P79). The STM measurement parameters are $V =$ (a)(d)-(f) 500 mV, (b)(c) −400 mV, $I =$ (a)-(c) 0.06 nA, (d)-(f) 0.1 nA. Copyright 2019 The Japan Society of Applied Physics [117].

The interlayer distance between the two graphene layers was investigated by STM on nanopits in the qFS regions. The nanopit edges have a height of 0.350 nm, which is less than on the other two samples in this work (0.369 nm on graphite and 0.375 nm on graphene/SiC(000$\bar{1}$)). Due to such a lower height a stronger interaction with the lower layer can be expected on this sample.

Figure 6.5 shows a larger STM image in (a) consisting of two images scanned next to each other, together with a schematic cross-section of this surface in (b). This figure illustrate the combinations of qFS graphene and (partly) hexagonal nanopits that were created by H-plasma etching.

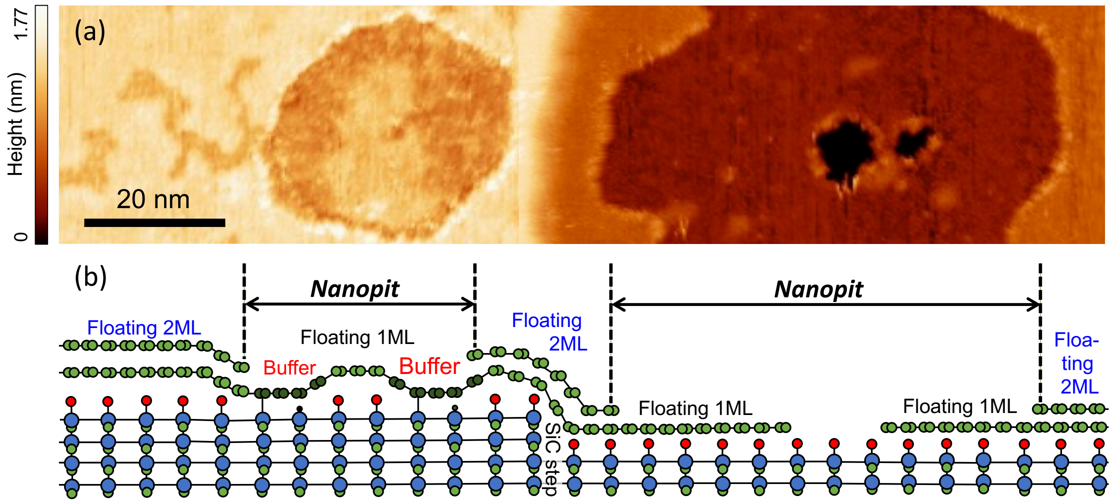

Figure 6.5: (a) STM images of nanopits on graphene/SiC(0001) (at $T = 78$ K) after H-plasma etching (sample 120710-2-1), and (b) schematic horizontal cross-section near the center of the STM image in (a). The green, blue and red circles represent carbon, silicon and hydrogen atoms, respectively. The graphene nanopit edges are expected to be H-terminated, but this is not shown. The STM parameters are $V = 500$ mV, $I = 0.06$ nA. Copyright 2019 The Japan Society of Applied Physics [117].

A feature that is often observed at nanopits on qFS terraces is a nanopit in the center of a larger hexagonal nanopit.

Examples of this are visible in Fig. 6.4(b) and at the right-hand side of Fig. 6.5(a). It is notable that small nanopits to the deeper (3rd) layer often appear in the center oof upper layer nanopits. On graphite (after longer etching times), lower layer nanopits are usually randomly distributed inside of upper layer nanopits. It suggests that a defect on the lower or both layers, may have served as a nucleation center for both the upper and lower layer nanopits. Furthermore, it is noteworthy that all nanopits in the lower graphene layer (the former buffer layer) are surrounded by quasi-free-standing terraces. It suggests that the passivation of the substrate by H is promoted by direct access of the H-plasma to the SiC from that small nanopit.

In Fig. 6.5, the left-hand side is only partially intercalated and the 3rd layer is not exposed. The right-hand side is completely intercalated and the 3rd layer is exposed. As discussed before, movement of H-atoms across the substrate step that separates these two terraces is apparently hindered.

Since both anisotropic etching and H-intercalation occur during the H-plasma treatment on this sample, different types of zigzag-aligned graphene edges are obtained. These are edges on the buffer layer, on the passivated SiC(0001) and on qFS graphene. Of these the last one was most frequently obtained and can be seen in the STM images of Figs. 6.4(a)(b) and Fig. 6.5(a)). We took preliminary measurements on single zigzag edges on qFS graphene, which are not shown here.

6.4 Summary of Chapter 6

H-plasma etching of the epitaxial monolayer graphene on SiC(0001) was investigated for future studies of the edge states under different substrate conditions. Its surface features a (6×6) superlattice that is induced by the lower C-rich buffer layer. After H-plasma etching, nanopits with monatomic depth were created, with hexagonal or rounded edges. They are less aligned in zigzag-direction than on graphite. The maximum nanopit size is similar as for the C-face sample and larger than on graphite. The differences of the etching results to those on graphite, likely stem from a higher density of initial defects. Most of the nanopits appeared on elevated terraces, where the nanopit height depth was found to be 0.35 nm.

In addition, elevated terraces with height of 0.12 ± 0.03 nm were created where the (6×6) pattern does not appear and a triangular atomic lattice is observed. This suggests the presence of another graphene layer below the originally monolayer graphene. STS reveals that the Dirac point is shifted close to the Fermi energy, and that the LDOS close by the Dirac point is suppressed, which can indicate bilayer graphene. The features of the elevated terraces are consistent with hydrogen (H) intercalation, as a result, we obtained quasi-free standing (qFS) bilayer graphene on the H-terminated SiC(0001) substrate. Thus, the nanopit depth on qFS regions corresponds to the interlayer distance between two graphene layer, which is less than on etched graphite or multi-layer graphene/SiC(000$\overline{1}$).

Within the suppressed LDOS range, position-dependent peaks appear. These LDOS peaks, as well as the presence of a $(\sqrt{3} \times \sqrt{3})$ superlattice, indicate localized electronic states on the elevated terraces. They are likely induced by dangling Si-bonds, which should be managed for STS studies of the edge states.

Chapter 7

Conclusions

In this work, the electronic states of graphene zigzag edges, obtained by hydrogen plasma (H-plasma) etching, were examined. Using H-plasma etching anisotropic nanopits with monatomic height were fabricated on the surface of graphite and on graphene. During the etching graphene step-edges that are aligned in the zigzag directions are created, thus hexagonal nanopits are formed in the exposed graphene layers. In this study, the surface of graphite, as well as few-layer graphene samples epitaxially grown on the C-face and on the Si-face of SiC, were investigated by scanning tunneling microscopy and spectroscopy (STM/STS). At room temperatures and atmospheric conditions only STM experiments were performed, and at temperatures between 78 K and 60 mK in ultra-high vacuum both STM and STS were employed. The main aim is to investigate the existence of spin-polarized edge-states. This was achieved by probing the electronic graphene edge states of zigzag graphene nanoribbons (zGNR) on samples with different interactions with substrates. On such zGNRs, spin-polarization is expected, but was not conclusively shown so far. The zigzag edge states are known to be sensitive to substrate influence, thus different graphene samples are investigated to clarify the different influences on such a state.

On all three systems zigzag edges could be fabricated by H-plasma etching using the same etching parameters and only varying the etching time. On the two few-layer epitaxial graphene samples the nanopits grew more rapidly during etching than on graphite and less well-shaped hexagonal pits were created. Both differences probably stem from a higher rate of nanopit formation on the few-layer samples due to a higher density of initial defects. On graphene/SiC($000\overline{1}$), the C-face, etching also removed rotational defects that existed before. However, the most significant additional effect occurred on graphene/SiC(0001), the Si-face, where large terraces became quasi-free standing (qFS) after etching due to hydrogen atoms passivating dangling bonds on the substrate. At the etched nanopits on the surface of graphene/SiC($000\overline{1}$) the interlayer distance was 0.377 nm and it was 0.350 nm on qFS graphene/SiC(0001), which suggests a decreased and an increased interaction with the substrate, respectively, compared to that on etched graphite (with distance 0.369 nm).

On graphite and on graphene/SiC($000\overline{1}$), STM/STS measurements showed single LDOS peaks near the Dirac point, together with LDOS depressions, that decay exponentially with distance from the edge. This indicates that the etched hexagonal nanopit edges host localized electronic states that conform with the single layer expectations of a zigzag edge state. Such results were obtained on graphene/SiC($000\overline{1}$), too, despite the presence of different morphologies, of strong doping, and of the apparent presence of localized states on some terraces. Zigzag edge states were observed on all types of terraces, showing the robustness of the edge states on this sample. A difference to the states on graphite is a wider energy range of the edge state LDOS.

Between etched hexagonal nanopits narrow zGNRs with widths from 4 to 42 nm are formed and the edge states at these were probed on graphite and on graphene/SiC($000\bar{1}$) by STM/STS down to 60 mK. In previous reports of spin-polarization, several limitations were always present, such as insufficient edge quality and termination, unknown substrate interaction, inability to vary the graphene nanoribbon width and limited statistical data, which hindered conclusive experimental confirmation of spin-polarization. Our measurements were able to avoid most of these problems by preparing nanoribbons by anisotropic H-plasma etching on the surface of graphite, where the substrate effect is well studied, and on graphene/SiC($000\bar{1}$), where we can compare single isolated and nanoribbon edge states. This allows us to obtain clear results of the edge states and their location and sublattice dependence.

STS at zGNRs on graphite revealed that its edge states become split where edge states on different sublattices are in close proximity on nanoribbons with zigzag edges. This suggests that interaction between states on different sublattices is necessary for the split. Furthermore, the edge state splitting depends on the nanoribbon width (W) and the substrate influence, since the split energy is inversely proportional to W and a slightly greater splitting is observed on the edge with weaker interactions with the lower layer. The observed edge state features are semi-quantitatively consistent with theoretical expectations of spin-polarization, by taking into account the effect of graphene substrate.

Indications of spin-splitting with larger LDOS peak separation were obtained on few-layer graphene/SiC($000\bar{1}$) as well. However, vastly different edge state features were obtained for different zGNRs, which may reflect the variety of different surface environments here. This result again shows the important role that the substrate plays for the edge states and may suggest a possible transition among different magnetic edge states, which could modify the edge states. Since the split edge states were observed in the presence of some edge disorder, and possibly on the doped graphene/SiC($000\bar{1}$), these result show their robustness in these conditions.

Future Prospects

In this work, clear indications for spin-polarization on graphene nanoribbons were obtained and several conditions for their occurrence were demonstrated. This opens the door towards future works and the application of tailor-made spin-polarized junctions, for example in novel spintronic devices. The potential of different substrates to modify spin-splitted edge states was demonstrated as well.

In the future, the most important work on zigzag graphene nanoribbons is the direct observation of the edge magnetism, which may be achieved by a spin-polarized STS technique. An important step towards this goal is the observation of the transition between different edge state spin alignments, e.g., between a non-magnetic state, a gapped or semi-metallic antiferromagnetic spin alignment and a metallic ferromagnetic spin alignment on the edge states, on graphene nanoribbons fabricated by hydrogen plasma etching. Such a transition can be induced by varying the several control parameters. These can be the applied magnetic field, gate voltage, doping and temperature, as well as the nanoribbon width and length to tune the energy differences between the different states and the crossover temperature below which the thermally activated fluctuations are suppressed or magnetic domain walls are trapped by defects. If the transition between different types of edge states can be induced by applying a magnetic field, this could directly show the magnetic property of the split edge states even by using a regular STS. For such an experiment, nanoribbons fabricated on the graphite surface are a suitable system. An additional verification of the results in this work can be obtained by checking that single hydrogen atoms passivate the etched edges, which may be done by electron energy loss spectroscopy or inelastic tunnel spectroscopy.

We hope that this work may spark new studies into spin polarization of graphene zigzag nanoribbons and the effect of the substrate, as well as may enable the development of novel graphene-based spintronic devices.

Appendices

Appendix A

Correction of Drift for Scanning Tunneling Spectroscopy Data

In this work, STM/STS measurements are utilized to probe the LDOS of samples. In each measurement, scans are made along lines across the sample surface, where the STM tip height and $\mathrm{d}I/\mathrm{d}V$ spectrum is measured at regular intervals (with unit distance x_{unit}). Usually, we chose to measure fewer points along a line by STS than by STM, since the required time for measurements at each point is longer. After completing scanning along a line, another line with equal length is scanned, until the scan is completed. Subsequent lines can be scanned at the same position (line mode), or at a parallel position, that is shifted by the distance x_{unit} orthogonally to the previous line. By shifting the scanning line, measurements are taken in a rectangular grid, which form a two-dimensional map. The positions of the data thus form lines and columns. Both the scanning direction and the number of lines and of points on a line can be adjusted.

Since the STS measurement time is longer than for STM, gradual drift of the STM tip relative to the sample during measurements is more significant. To correct the drift, we have shifted the positions of measurements on different lines or columns. To determine the appropriate shift, we compare the STM image acquired during the STM/STS measurement to the STM images that are taken before and after every STM/STS measurement and that are less-affected by drift due to shorter measurement times.

An example of lateral drift adjustment for a line mode STM/STS measurement with four lines across a graphene edge is shown in the height profile in Fig. A.1(a). It is clearly seen that the edge position is shifted between measurement lines. To analyze such data, the lateral positions of the measured height and $\mathrm{d}I/\mathrm{d}V$ values were shifted to compensate for drift. The correction was done to match the height profiles to the one of the line initially measured, as shown in (b). The shifted positions were matched to the neighboring distance coordinates of the initial sweep by making a weighted average of the $\mathrm{d}I/\mathrm{d}V$ measurement at each position. This is shown in the schematic distance coordinates of two subsequent measured lines in (c) and (d). Therefore the number of averaged data points is reduced around both ends of the scan line. In the case of a shifted coordinate being out of range of the initial line position coordinates, that value is discarded, and the number of data points in the averages is reduced at the scan line ends. This was done in order to be able to make averages of the $\mathrm{d}I/\mathrm{d}V$ of all sweeps while continuing to use the same distance coordinates.

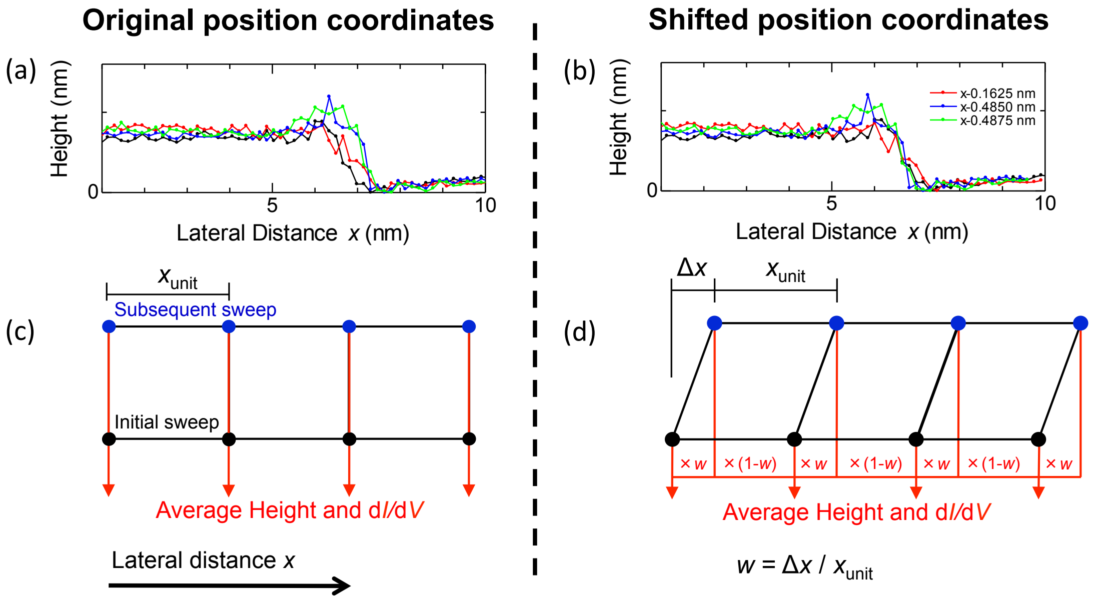

Figure A.1: (a) Height profile measured at $T = 78$ K across an etched nanopit edge on graphite (sample Kish-P40). Four lines were measured (order of measurements: black, red, blue, green symbols) during line mode STM/STS. The edge position shifted in positive x direction on each subsequent line. (b) The height profile of (a) was shifted, such that the three subsequent lines (red, blue, green symbols) best match the initial one (black symbols) to correct the drift between them. (c) Schematic representation of the data averaging for the original datasets. (d) Schematic representation of the weighted averaging for data shifted by distance Δx. To make averages at the same x coordinates, the $\mathrm{d}I/\mathrm{d}V$ values were multiplied by the weight w or $(1 - w)$ and included in the $\mathrm{d}I/\mathrm{d}V$ average of the closest neighbor on the left or right.

Appendix B

Graphene/SiC($000\overline{1}$)

B.1 Comparison of H-plasma Etching Trials

The STM/STS results of etched graphene/SiC($000\overline{1}$) that are discussed in Chapter 4 were obtained on sample G1213 after etching it for 10 min. An identical sample (G1212) was etched for 30 min, after which poor surface conductivity made it difficult to probe it by STM/STS. Such difficulties did not occur when probing the sample etched for 10 min. This is because the epitaxial graphene is completely removed on some regions of G1212 after etching for 30 min, which can be confirmed by Raman spectroscopy.

Figure B.1 shows the Raman spectra obtained on sample G1212 before etching and after a 30 min treatment and of sample G1213 after 10 min etching. In the wavenumber range $1460 - 1940$ cm^{-1} the Raman intensity is increased due to the SiC substrate. The presence of graphene on these samples is indicated by the G and the G' peaks at about 1576 cm^{-1} and between $2690 - 2735$ cm^{-1}, respectively [120]. For each case, two curves are shown, that are representative of areas with stronger (black curves) or with weaker graphene signatures (blue curves). Both of these peaks clearly appear on all regions of the samples before etching and after 10 min etching, however, after 30 min etching in some regions they do not (blue curve after 30 min etching). This indicates that there are relatively large regions on the sample after 30 min etching that are no longer covered by graphene. The absence of epitaxial graphene in some areas can cause the sample surface to not be conductive (since the SiC substrate posses a band gap).

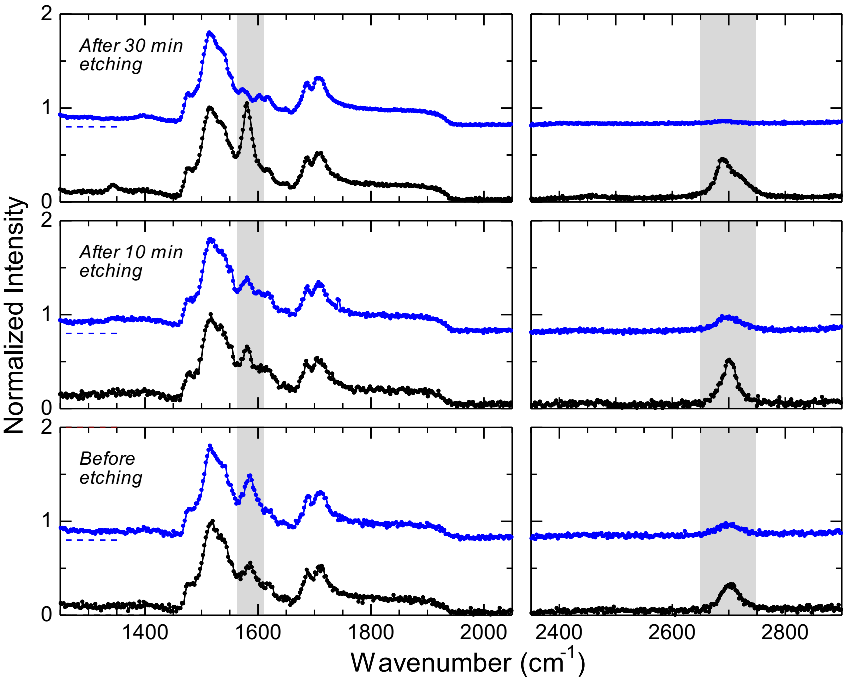

Figure B.1: Raman spectra taken on graphene/SiC(000$\bar{1}$), before etching (sample G1212), after 10 min etching (sample G1213), after 30 min etching (sample G1212) for two different regions (black and blue) for each sample. The Raman intensity of each spectrum is normalized at 1517 cm^{-1}. The G peak (at about 1576 cm^{-1}) and the G' peak (at 2690 – 2735 cm^{-1}) indicate the presence of graphene, their range is shaded. The sample surface is not completely homogeneous area with higher intensity graphene signature peaks (black curves) and with lower intensity peaks (blue curves) are observed.

B.2 Tunneling Spectroscopy on Bulk Graphene/SiC(000$\bar{1}$)

Measured dI/dV were, which are position-dependent on the bulk terraces of epitaxial graphene on SiC(000$\bar{1}$). These are discussed here in more detail. The main results obtained on that sample are discussed in Section 5, the tunneling spectra on bulk terraces are discussed in Section 5.2.2, where these features were only briefly mentioned.

An example is shown in Fig. B.2, where the results of STS measurements on a bulk terrace are shown, on which dI/dV peaks appear. These measurements were taken on a H-plasma etched surface and nanopits are created at the top and bottom area in (a). In Fig. B.2(b), the dI/dV maps on the terrace at three different bias voltages are shown. At the higher ($V = -84$ mV) and the lower ($V = -254$ mV) voltages only a weak spatial dependence of the LDOS is observed. However, at $V = -172$ mV, clearly an increased dI/dV value was measured in the center of the terrace. The STM image (B.2(a)) reveals several bright spots, but they apparently do not correspond to the position of of the tunnel spectrum features. The colormap in Fig. B.2(c) shows the tunnel spectra along the arrow in (a), revealing a peak in the center of the probed area. This is not due to an edge state, since its intensity increases farther away from the edge, as seen in (b). Figure B.2(d) shows the average tunnel spectra in the range

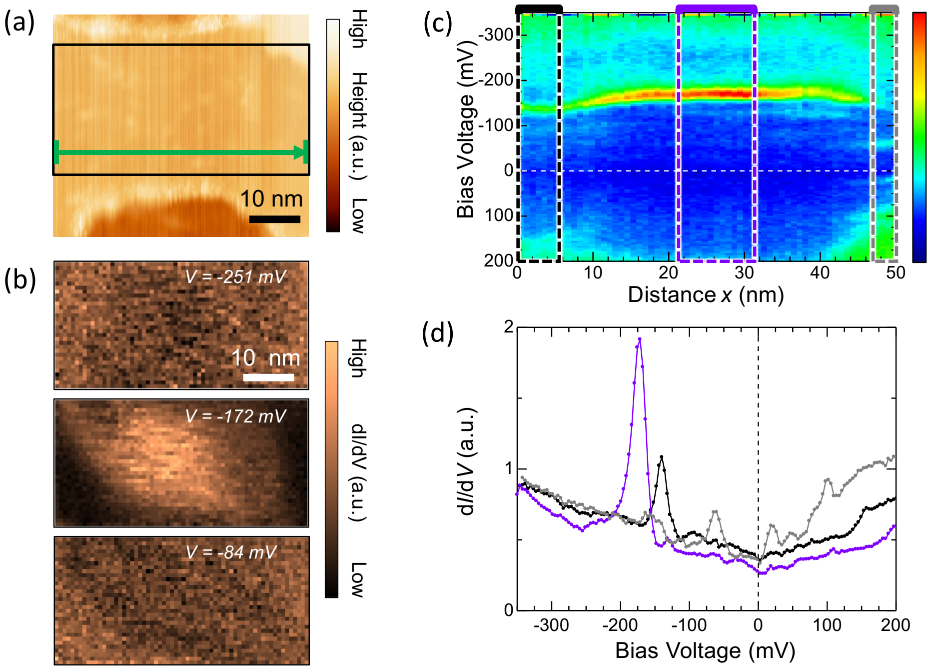

Figure B.2: STM/STS on a flat terrace on etched graphene/SiC(000$\bar{1}$) (sample G1213, PtIr STM tip). (a) STM image, the dI/dV maps in (b) were taken in the black rectangle at three different V. (c) dI/dV colormap along the blue arrow in (a). (d) dI/dV curves of the averages indicated by brackets and dashed lines in (c) with corresponding colors. The STM/STS parameters are $V = -350$ mV, $I =$ nA, $V_{\text{mod}} = 3.9$ mV.

of (c) between 0 nm $\leq x \leq$ 5.7 nm (black curve), 21.3 nm $\leq x \leq$ 31.2 nm (purple curve) and 46.8 nm $\leq x \leq$ 50 nm (gray curve). In the three regions, different LDOS peaks apparently appear in the graphene bulk terrace. The peak in the center, at about 17 nm $\leq x \leq$ 36 nm, is shown by the purple curve at $V = -171.6 \pm 3.9$ mV. Beyond this range this peak's intensity gradually decreases and it shifts to higher energies. At the position of the gray curve, the center peak has mostly disappeared and different, smaller peaks appear instead at $V = -62.6, 20.6$ and 97.9 ± 3.9 mV. At the position of the black curve, the energy-shifted center peak continues to appear with a reduced intensity, as well as a small bump at $V \approx 90$ mV.

These LDOS features indicate states that do not stem from edges or vacancy states on the surface graphene layer, since they do not correspond to any features we observed on the surface by STM. Instead, they may be related to features that lie below the surface and were not seen by STM.

In addition to the spatial variations inside bulk terraces, these LDOS peaks also change spatially close to graphene edges. In Fig. B.3(a), the STM image of an etched nanopit on a rough graphene region are shown. dI/dV spectra were taken across one nanopit edge shown in (a) in the height profile shown in (c) and dI/dV colormap in (d). This includes results on the lower terrace, on the edge and on the upper terrace bulk region. Averaged tunnel spectra from these three regions are shown in (d). In the bulk region of the upper terrace, a single peak clearly appears for $x > 10$ nm at at $V = 49.5 \pm 3.6$ mV (blue curve in (d)), but interestingly, it decays in the vicinity of the

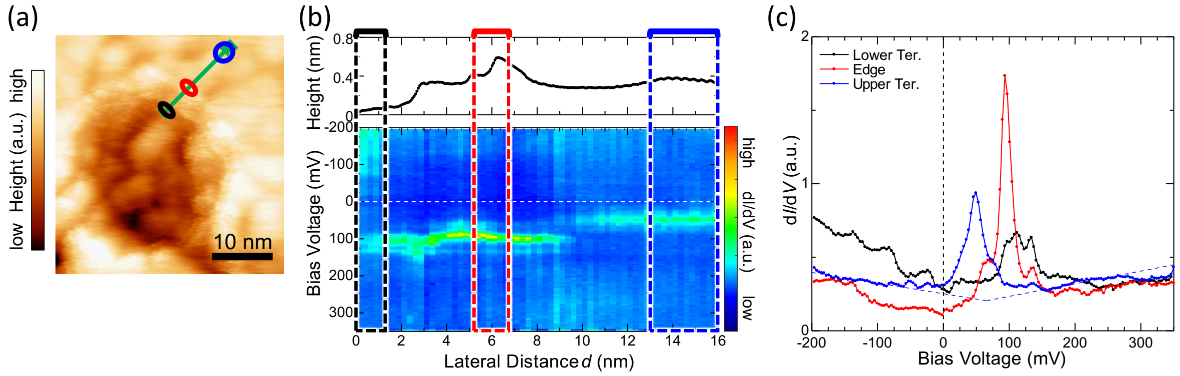

Figure B.3: STM/STS measurement on etched graphene/SiC(000$\bar{1}$) across a nanopit edge at $T = 2$ K (sample G1213, PtIr STM tip). (a) STM image of a hexagonal nanopit on graphene in a rough surface region. (b) Height profile and dI/dV colormap along the black line in (a) across the nanopit edge. (c) dI/dV spectra taken at the positions of the circles in (a) and the brackets and dashed lines in (b) with the corresponding colors. The Dirac point on the upper terrace is estimated from the fitted blue lines to be at $V = +66.0 \pm 3.6$ mV. The STM/STS parameters are $V = 350$ mV, $I = 0.04$ nA, $V_{\mathrm{mod}} = 3.6$ mV.

edge. On the upper terrace near the edge, for about $5 \leq x \leq 10$ nm, a different LDOS peak appears at $V = 94$ mV (red curve in (d)). This is relatively close in energy to the Dirac point, which is estimated at about $V = 66.0 \pm 3.6$ mV. The peak is most intense at the edge, gradually decays with distance on the upper terrace, and does not appear on the lower terrace. This indicates that this peak appears due to an edge state, which is expected at the zigzag edges of the etched nanopits. On the lower terrace, a smaller peak appear at different bias voltage of $V = 112$ mV, thus the two LDOS peaks can be distinguished and it is clear that the peak on the bulk terrace does not appear on the edge. Instead, this peak decays, even as the edge state intensity gradually increases, such a behavior has been confirmed near other edges as well. Therefore, the LDOS peaks that are observed on nanopit edges are probably indicating edge states, as is the case here.

Along the whole measured distance, an additional small dI/dV peak was measured at $V = 134$ mV. Since this small peak appears in both bulks and even while the tip was moving across the edge, this peak is unlikely to t indicates a bulk or an edge state that belongs to either layer.

A different type of LDOS peak was observed on the sample surface before etching on Moiré superlattices with large lattice constants ($a_{\mathrm{MP}} > 10$ nm), such as the one shown in the STM images of Fig. B.4(a) with $a_{\mathrm{MP}} = 11.8$ nm (expected inter-layer rotation is 1.2°). The STS measurements in (b) were taken across several of the bright Moiré spots [121]. The tunnel spectra reveal three peaks, at $V = -63$ mV, -124 mV, and -142 mV, the middle ones clearly smaller than the other two. The peaks increase and decrease in intensity following the Moir'e pattern. The averaged spectra on top of two adjacent AA areas, and one from between them is shown in (c). The peaks appear much more intense on the AA regions. From the spectrum with smaller peaks, the Dirac point energy is estimated, yielding a value of $V = -113$ mV, which lies between the two stronger peaks. These two strong LDOS peaks likely appear because of van Hove

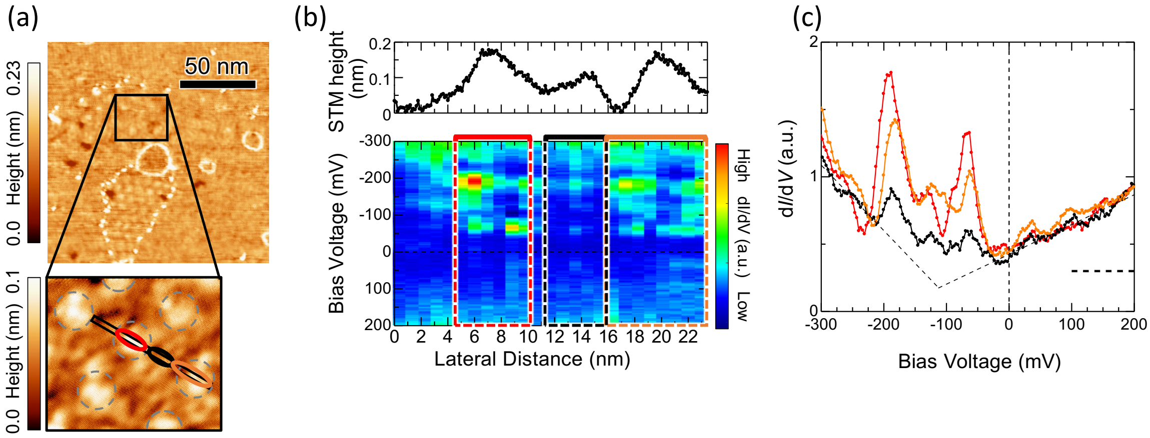

Figure B.4: STM/STS measurements across a Moiré pattern on graphene/SiC($000\overline{1}$) before etching. (a) STM image of the Moiré region and magnified image inside of it, showing the position of (b) the STM height profile and dI/dV colormap. (c) Averaged tunnel spectra on (orange, red curves) and between (black curve) the AA stacked regions of the Moiré pattern. Linear fits of the black curve at higher values of V are plotted by dashed lines. The STM/STS parameters are $V = 300$ mV, $I = 0.06$ nA, $V_{\mathrm{mod}} = 3.0$ mV.

singularities that exist due to the rotation between the top two graphene layers. While not exactly symmetric on this sample, their position on both sides of the Dirac point, and their increased intensity on the AA regions are consistent with this [115]. The additional, weaker LDOS peak seems to be related too, since it exhibits a similar spatial periodicity, but its origin is not clear.

These van Hove singularity peaks are different from the peaks that were observed on some bulk terraces in that their spatial dependence follows the periodicity of a Moiré superlattice and that they appear in pairs, as was observed. This was however not seen for the bulk peaks, which did not show a spatial periodicity, and usually appeared as a single peak. Furthermore, the van Hove peaks would only appear nearby the Dirac point if there is a large rotation angle, resulting in large a_{MP}. It is conceivable that one van Hove peak appears near the Fermi energy, if there is both a sufficiently large doping and a smaller rotation angle. This is unlikely to have been the case, since the Dirac point was always obtained within the observed spectral range, and because smaller rotations form smaller Moiré lattices that are easier to observe by STM. The bulk peaks discussed here did not occur in a region with a visible Moiré pattern, thus they are probably not related. Finally, bulk peaks appear before and after etching, during which the Moiré patterns were removed. Thus these peaks are not related to inter-layer rotation and originate from a different source, which are possibly defect states that are induced by structures on lower layers.

B.3 Large Etched Nanopits on Graphite

On the graphite sample, that was etched together with the graphene/SiC($000\overline{1}$) sample for $t = 10$ min (and etching parameters $T = 600$°C, $P_{\mathrm{H}} = 110$ Pa, $W_{\mathrm{RF}} = 20$ W), an unusual area was observed, where a high density of hexagonal nanopits appeared along

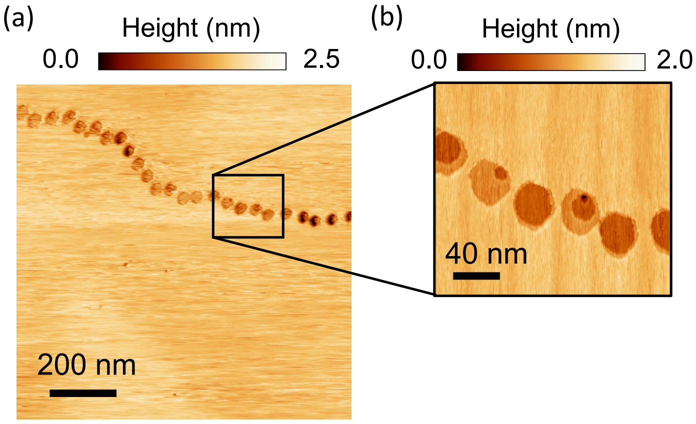

Figure B.5: STM images of the surface of graphite (sample HOPG-P123) that was etched by H-plasma together with the graphene/SiC($000\bar{1}$) (sample G1213). (b) shows a magnified images of area indicated in (a), and show height profiles along the position of the arrows drawn in the STM images. All measurements were obtained at room temperature in atmospheric conditions. STM parameters are $V = 0.5$ V, $I = 0.1$ nA.

a line (Figs. B.5(a)(b)). These were probably created along a line of initial defects that were present before etching. These nanopits were not only unusual due to their high density, but also due to their larger size. In this unusual area, the largest nanopit diameter was about 38 nm, which is about 50% larger than observed elsewhere on this graphite sample, but very similar to the diameter of the large nanopits on graphene/SiC($000\bar{1}$). Since similar sizes were produced on both samples by the same etching process, it seems that the nanopit growth rate is nearly identical. However, the nanopits on the epitaxial sample form more quickly than on pristine graphite. In fact, the formation time seems to be similar as for the special case of initial defects on graphite. This indicates that faster nanopit formation, but not faster nanopit growth, accelerates the etching.

Acknowledgements

First, I want to thank Prof. Hiroshi Fukuyama for giving me the chance to join his research group, as well as for his guidance and discussions with which he often successfully ignited my curiosity to try something new. Further, for his tireless help and encouragements during this work which he is always willing to offer. I am also gratefully indebted to him for his very valuable comments, suggestions and proof-reading of this thesis.

I want to express my gratitude to Dr. Tomohiro Matsui, who built the ULT-SPM system, taught me in its use, and that of many other important experimental techniques. He pioneered the H-plasma etching technique and pursued the series of works on etched graphene zigzag edges that I could join and that eventually cumulated in this one. For the opportunity to contribute to this project I am deeply in his debt. I am grateful as well for his valuable comments on this thesis.

I thank Prof. Ryo Shimano for accepting me as a student in his team during my last semester, so that I can write this thesis.

My special thanks go to Prof. Shuji Hasegawa, Prof. Kensuke Kobayashi, Prof. Shingo Katsumoto, Prof. Osamu Sugino and Prof. Fumio Komori for reviewing this work and providing valuable comments.

Furthermore, I thank Hideki Sato, for helping to lay out the groundwork that this work builds upon and Kazuma Kita, for his work to improve the H-plasma etching technique. My gratitude goes to Ryuji Nakamura and Jun Usami, for their friendship, support and many long discussions during shared meals.

I also thank the other former members with whom I shared my time in Fukuyama laboratory: Dr. Kazuki Nakayama, for teaching and letting me participate in his experiments, Dr. Masahiro Kamada, Katsuyoshi Ogawa, Megumi Avigail Yoshitomi and Naomasa Suzuki, for their support. I also want to thank Valentina Eremina and Paul Yilin Liu, who during their respective terms as exchange students were helpful and curious and made the laboratory a more interesting place to be. I would like to thank Prof. Satoshi Murakawa, the members of Murakawa laboratory and Asst. Prof. Sachiko Nakamura for their various advice and help. More generally, I want to thank all the lab-members for creating a friendly and inclusive environment in the laboratory.

I want to acknowledge the financial support by the University of Tokyo Fellowship, that allowed me to concentrate fully on the scientific work.

Finally, I would like to thank my parents and my fiancé, who made it possible for me to live in Japan, for their unfailing support and encouragement throughout the last five years. This would not have been possible without them.

Bibliography

[1] L. Radushkevich and V. Lukyanovich, Russian Journal of Physical Chemistry A **26**, 88 (1952).

[2] S. Iijima, Nature **354**, 56 (1991).

[3] H. W. Kroto, J. R. Heath, S. C. O'Brien, R. F. Curl, and R. E. Smalley, Nature **318**, 162 (1985).

[4] P. R. Wallace, Physical Review **71**, 622 (1947).

[5] K. S. Novoselov, A. K. Geim, S. V. Morozov, D. Jiang, Y. Zhang, S. V. Dubonos, I. V. Grigorieva, and A. A. Firsov, Science **306**, 666 (2004).

[6] K. S. Novoselov, A. K. Geim, S. V. Morozov, D. Jiang, M. I. Katsnelson, I. V. Grigorieva, S. V. Dubonos, and A. A. Firsov, Nature **438**, 197 (2005).

[7] Y. Zhang, Y.-W. Tan, H. L. Stormer, and P. Kim, Nature **438**, 201 (2005).

[8] A. C. Neto, F. Guinea, N. M. Peres, K. S. Novoselov, and A. K. Geim, Reviews of Modern Physics **81**, 109 (2009).

[9] H. Aoki and M. S. Dresselhaus, *Physics of Graphene* (Springer Science & Business Media, 2013).

[10] M. Fujita, K. Wakabayashi, K. Nakada, and K. Kusakabe, Journal of the Physical Society of Japan **65**, 1920 (1996).

[11] Y. Niimi, T. Matsui, H. Kambara, K. Tagami, M. Tsukada, and H. Fukuyama, Applied Surface Science **241**, 43 (2005).

[12] Y. Niimi, T. Matsui, H. Kambara, K. Tagami, M. Tsukada, and H. Fukuyama, Physical Review B **73**, 085421 (2006).

[13] Y. Kobayashi, K. Fukui, T. Enoki, K. Kusakabe, and Y. Kaburagi, Physical Review B **71**, 193406 (2005).

[14] V. M. Pereira, F. Guinea, J. M. B. Lopes dos Santos, N. M. R. Peres, and A. H. Castro Neto, Physical Review Letters **96**, 036801 (2006).

[15] H. Lee, Y.-W. Son, N. Park, S. Han, and J. Yu, Physical Review B **72**, 174431 (2005).

[16] Y.-W. Son, M. L. Cohen, and S. G. Louie, Physical Review Letters **97**, 216803 (2006).

[17] Y.-W. Son, M. L. Cohen, and S. G. Louie, Nature **444**, 347 (2006).

[18] M. Chen and M. Weinert, Physical Review B **94**, 035433 (2016).

[19] M. Wimmer, I. Adagideli, S. Berber, D. Tománek, and K. Richter, Physical Review Letters **100**, 177207 (2008).

[20] F. Muñoz-Rojas, J. Fernández-Rossier, and J. Palacios, Physical Review Letters **102**, 136810 (2009).

[21] G. Z. Magda, X. Jin, I. Hagymási, P. Vancsó, Z. Osváth, P. Nemes-Incze, C. Hwang, L. P. Biro, and L. Tapaszto, Nature **514**, 608 (2014).

[22] P. Ruffieux, S. Wang, B. Yang, C. Sánchez-Sánchez, J. Liu, T. Dienel, L. Talirz, P. Shinde, C. A. Pignedoli, D. Passerone, and T. Dumslaff, Nature **531**, 489 (2016).

[23] C. Tao, L. Jiao, O. V. Yazyev, Y.-C. Chen, J. Feng, X. Zhang, R. B. Capaz, J. M. Tour, A. Zettl, S. G. Louie, and H. Dai, Nature Physics **7**, 616 (2011).

[24] R. Yang, L. Zhang, Y. Wang, Z. Shi, D. Shi, H. Gao, E. Wang, and G. Zhang, Advanced Materials **22**, 4014 (2010).

[25] L. Xie, L. Jiao, and H. Dai, Journal of the American Chemical Society **132**, 14751 (2010).

[26] G. Diankov, M. Neumann, and D. Goldhaber-Gordon, ACS Nano **7**, 1324 (2013).

[27] D. Hug, S. Zihlmann, M. K. Rehmann, Y. B. Kalyoncu, T. N. Camenzind, L. Marot, K. Watanabe, T. Taniguchi, and D. M. Zumbühl, npj 2D Materials and Applications **1**, 1 (2017).

[28] T. Matsui, H. Sato, A. E. Amend, K. Kita, and H. Fukuyama, The Journal of Physical Chemistry C **123**, 22665 (2019).

[29] X. Zhang, O. V. Yazyev, J. Feng, L. Xie, C. Tao, Y.-C. Chen, L. Jiao, Z. Pedramrazi, A. Zettl, S. G. Louie, H. Dai and M. F. Crommie, ACS Nano **7**, 198 (2012).

[30] Y. Li, W. Zhang, M. Morgenstern, and R. Mazzarello, Physical Review Letters **110**, 216804 (2013).

[31] O. V. Yazyev, R. B. Capaz, and S. G. Louie, Physical Review B **84**, 115406 (2011).

[32] L. E. F. Torres, S. Roche, and J.-C. Charlier, *Introduction to Graphene-Based Nanomaterials* (Cambridge University Press, 2014).

[33] M. S. Dresselhaus and G. Dresselhaus, Advances in Physics **51**, 1 (2002).

[34] L. N. Srivastava, G. He, R. M. Feenstra, and P. J. Fisher, Physical Review B **82**, 235406 (2010).

[35] P. N. First, W. A. de Heer, T. Seyller, C. Berger, J. A. Stroscio, and J.-S. Moon, MRS Bulletin **35**, 296 (2010).

[36] X. Yu, C. Hwang, C. M. Jozwiak, A. Köhl, A. K. Schmid, and A. Lanzara, Journal of Electron Spectroscopy and Related Phenomena **184**, 100 (2011).

[37] M. Naitoh, M. Kitada, S. Nishigaki, N. Toyama, and F. Shoji, Surface Review and Letters **10**, 473 (2003).

[38] F. Varchon, P. Mallet, L. Magaud, and J.-Y. Veuillen, Physical Review B **77**, 165415 (2008).

[39] L. I. Johansson, S. Watcharinyanon, A. Zakharov, T. Iakimov, R. Yakimova, and C. Virojanadara, Physical Review B **84**, 125405 (2011).

[40] J. Hass, R. Feng, J. Millán-Otoya, X. Li, M. Sprinkle, P. N. First, W. De Heer, E. Conrad, and C. Berger, Physical Review B **75**, 214109 (2007).

[41] M. Sprinkle, D. Siegel, Y. Hu, J. Hicks, A. Tejeda, A. Taleb-Ibrahimi, P. Le Fèvre, F. Bertran, S. Vizzini, H. Enriquez, and S. Chiang, Physical Review Letters **103**, 226803 (2009).

[42] D. L. Miller, K. D. Kubista, G. M. Rutter, M. Ruan, W. A. de Heer, P. N. First, and J. A. Stroscio, Physical Review B **81**, 125427 (2010).

[43] T. Yamauchi, T. Ueda, M. Naitoh, S. Nishigaki, and M. Kusunoki, in *Journal of Physics: Conference Series* (IOP Publishing, 2008), vol. 100, p. 082007.

[44] G. Prakash, M. A. Capano, M. L. Bolen, D. Zemlyanov, and R. G. Reifenberger, Carbon **48**, 2383 (2010).

[45] L. B. Biedermann, M. L. Bolen, M. A. Capano, D. Zemlyanov, and R. G. Reifenberger, Physical Review B **79**, 125411 (2009).

[46] W.-Y. Ching and P. Rulis, *Electronic Structure Methods for Complex Materials: The orthogonalized linear combination of atomic orbitals* (Oxford University Press, 2012).

[47] C. Berger, Z. Song, X. Li, X. Wu, N. Brown, C. Naud, D. Mayou, T. Li, J. Hass, A. N. Marchenkov, E. H. Conrad, Science **312**, 1191 (2006).

[48] X. Wu, X. Li, Z. Song, C. Berger, and W. A. de Heer, Physical Review Letters **98**, 136801 (2007).

[49] D. L. Miller, K. D. Kubista, G. M. Rutter, M. Ruan, W. A. de Heer, P. N. First, and J. A. Stroscio, Science **324**, 924 (2009).

[50] J. Hass, F. Varchon, J.-E. Millan-Otoya, M. Sprinkle, N. Sharma, W. A. de Heer, C. Berger, P. N. First, L. Magaud, and E. H. Conrad, Physical Review Letters **100**, 125504 (2008).

[51] Y. J. Song, A. F. Otte, Y. Kuk, Y. Hu, D. B. Torrance, P. N. First, W. A. De Heer, H. Min, S. Adam, M. D. Stiles, and A. H. MacDonald, Nature **467**, 185 (2010).

[52] Y.-M. Lin, C. Dimitrakopoulos, D. B. Farmer, S.-J. Han, Y. Wu, W. Zhu, D. K. Gaskill, J. L. Tedesco, R. L. Myers-Ward, C. R. Eddy Jr, A. Grill, Applied Physics Letters **97**, 112107 (2010).

[53] W. A. De Heer, C. Berger, X. Wu, M. Sprinkle, Y. Hu, M. Ruan, J. A. Stroscio, P. N. First, R. Haddon, B. Piot, and C. Faugeras, Journal of Physics D: Applied Physics **43**, 374007 (2010).

[54] K. V. Emtsev, F. Speck, T. Seyller, L. Ley, and J. D. Riley, Physical Review B **77**, 155303 (2008).

[55] T. Jayasekera, S. Xu, K. W. Kim, and M. B. Nardelli, Physical Review B **84**, 035442 (2011).

[56] P. Lauffer, K. Emtsev, R. Graupner, T. Seyller, L. Ley, S. Reshanov, and H. Weber, Physical Review B **77**, 155426 (2008).

[57] A. Luican, G. Li, and E. Y. Andrei, Physical Review B **83**, 041405 (2011).

[58] A. N. Sidorov, K. Gaskill, M. Buongiorno Nardelli, J. L. Tedesco, R. L. Myers-Ward, C. R. Eddy Jr, T. Jayasekera, K. W. Kim, R. Jayasingha, A. Sherehiy, and A. Stallard, Journal of Applied Physics **111**, 113706 (2012).

[59] G. M. Rutter, N. Guisinger, J. Crain, E. Jarvis, M. D. Stiles, T. Li, P. First, and J. A. Stroscio, Physical Review B **76**, 235416 (2007).

[60] F. Owman and P. Mårtensson, Surface Science **369**, 126 (1996).

[61] P. Mallet, F. Varchon, C. Naud, L. Magaud, C. Berger, and J.-Y. Veuillen, Physical Review B **76**, 041403 (2007).

[62] S. Watcharinyanon, C. Virojanadara, J. Osiecki, A. Zakharov, R. Yakimova, R. Uhrberg, and L. I. Johansson, Surface Science **605**, 1662 (2011).

[63] C. Riedl, C. Coletti, T. Iwasaki, A. Zakharov, and U. Starke, Physical Review Letters **103**, 246804 (2009).

[64] T. Matsui, H. Kambara, Y. Niimi, K. Tagami, M. Tsukada, and H. Fukuyama, Physical Review Letters **94**, 226403 (2005).

[65] S. Ono, Journal of the Physical Society of Japan **40**, 498 (1976).

[66] F. Guinea, A. C. Neto, and N. Peres, Physical Review B **73**, 245426 (2006).

[67] D. Tománek, S. G. Louie, H. J. Mamin, D. W. Abraham, R. E. Thomson, E. Ganz, and J. Clarke, Physical Review B **35**, 7790 (1987).

[68] S. Morozov, K. Novoselov, F. Schedin, D. Jiang, A. Firsov, and A. Geim, Physical Review B **72**, 201401 (2005).

[69] M. M. Ugeda, I. Brihuega, F. Guinea, and J. M. Gómez-Rodríguez, Physical Review Letters **104**, 096804 (2010).

[70] V. M. Pereira, J. M. B. Lopes dos Santos, and A. H. Castro Neto, Physical Review B **77**, 115109 (2008).

[71] J. L. Lado, N. Garcia-Martinez, and J. Fernández-Rossier, Synthetic Metals **210**, 56 (2015).

[72] N. Peres, F. Guinea, and A. C. Neto, Annals of Physics **321**, 1559 (2006).

[73] K. Nakada, M. Fujita, G. Dresselhaus, and M. S. Dresselhaus, Physical Review B **54**, 17954 (1996).

[74] E. V. Castro, N. Peres, and J. L. dos Santos, EPL (Europhysics Letters) **84**, 17001 (2008).

[75] E. C. Stoner, Proceedings of the Royal Society of London. Series A, Mathematical and Physical Sciences pp. 372–414 (1938).

[76] N. D. Mermin and H. Wagner, Physical Review Letters **17**, 1133 (1966).

[77] O. V. Yazyev and M. Katsnelson, Physical Review Letters **100**, 047209 (2008).

[78] P. Esquinazi, A. Setzer, R. Höhne, C. Semmelhack, Y. Kopelevich, D. Spemann, T. Butz, B. Kohlstrunk, and M. Lösche, Physical Review B **66**, 024429 (2002).

[79] Y. Zhang, S.-Y. Li, H. Huang, W.-T. Li, J.-B. Qiao, W.-X. Wang, L.-J. Yin, K.-K. Bai, W. Duan, and L. He, Physical Review Letters **117**, 166801 (2016).

[80] O. V. Yazyev and L. Helm, Physical Review B **75**, 125408 (2007).

[81] W. Jiang, Y.-Y. Yang, and A.-B. Guo, Carbon **95**, 190 (2015).

[82] L. Pisani, J. Chan, B. Montanari, and N. Harrison, Physical Review B **75**, 064418 (2007).

[83] K. Sawada, F. Ishii, M. Saito, S. Okada, and T. Kawai, Nano Letters **9**, 269 (2009).

[84] J. Jung and A. MacDonald, Physical Review B **79**, 235433 (2009).

[85] C. L. Kane and E. J. Mele, Physical Review Letters **95**, 226801 (2005).

[86] J. Jiang, W. Lu, and J. Bernholc, Physical Review Letters **101**, 246803 (2008).

[87] Z. Pan and R. Yang, Journal of Catalysis **123**, 206 (1990).

[88] L. Jiao, X. Wang, G. Diankov, H. Wang, and H. Dai, Nature Nanotechnology **5**, 321 (2010).

[89] H. Sato, Master's thesis, University of Tokyo (2015).

[90] K. Kita, Master's thesis, University of Tokyo (2018).

[91] Rotary pump: GLD-201B, ULVAC KIKO, Inc.

[92] Electrical furnace: Isuzu Seisakusho Ltd.

[93] RF generator: TX03-9001-00, ADTEC Plasma Technology Co., Ltd.

[94] RF matching box: AMV-200HM, ADTEC Plasma Technology CO., LTD.

[95] E. Despiau-Pujo, A. Davydova, G. Cunge, and D. B. Graves, Plasma Chemistry and Plasma Processing **36**, 213 (2016).

[96] A. Harpale, M. Panesi, and H. B. Chew, Physical Review B **93**, 035416 (2016).

[97] Y. Kobayashi, K.-i. Fukui, T. Enoki, and K. Kusakabe, Physical Review B **73**, 125415 (2006).

[98] A. Davydova, E. Despiau-Pujo, G. Cunge, and D. Graves, Journal of Physics D: Applied Physics **48**, 195202 (2015).

[99] B. J. Wood and H. Wise, The Journal of Physical Chemistry **73**, 1348 (1969).

[100] I. Horcas, R. Fernández, J. Gomez-Rodriguez, J. Colchero, J. Gómez-Herrero, and A. Baro, Review of Scientific Instruments **78**, 013705 (2007).

[101] H. Kambara, T. Matsui, Y. Niimi, and H. Fukuyama, Review of Scientific Instruments **78**, 073703 (2007).

[102] A. E. Amend, Master's thesis, The University of Tokyo (2017).

[103] D. C. Kim, D.-Y. Jeon, H.-J. Chung, Y. Woo, J. K. Shin, and S. Seo, Nanotechnology **20**, 375703 (2009).

[104] A. E. Amend, T. Matsui, H. Sato, and H. Fukuyama, e-Journal of Surface Science and Nanotechnology **16**, 72 (2018).

[105] G. Lee and K. Cho, Physical Review B **79**, 165440 (2009).

[106] A. Cresti, F. Ortmann, T. Louvet, D. Van Tuan, and S. Roche, Physical Review Letters **110**, 196601 (2013).

[107] K. Sasaki, S. Murakami, and R. Saito, Applied Physics Letters **88**, 113110 (2006).

[108] M. Y. Han, B. Özyilmaz, Y. Zhang, and P. Kim, Physical Review Letters **98**, 206805 (2007).

[109] X. Li, X. Wang, L. Zhang, S. Lee, and H. Dai, Science **319**, 1229 (2008).

[110] V. Barone, O. Hod, and G. E. Scuseria, Nano Letters **6**, 2748 (2006).

[111] I. G. Ivanov, J. U. Hassan, T. Iakimov, A. A. Zakharov, R. Yakimova, and E. Janzén, Carbon **77**, 492 (2014).

[112] Reflectance maps courtesy of Graphensic AB.

[113] J. Xhie, K. Sattler, M. Ge, and N. Venkateswaran, Physical Review B **47**, 15835 (1993).

[114] D. Sun, J. Rioux, J. Sipe, Y. Zou, M. T. Mihnev, C. Berger, W. A. de Heer, P. N. First, and T. B. Norris, Physical Review B **85**, 165427 (2012).

[115] I. Brihuega, P. Mallet, H. González-Herrero, G. T. De Laissardière, M. Ugeda, L. Magaud, J. Gómez-Rodríguez, F. Ynduráin, and J.-Y. Veuillen, Physical Review Letters **109**, 196802 (2012).

[116] S. Bagchi, H. Johnson, and H. Chew, Physical Review B **101**, 054109 (2020).

[117] A. E. Amend, T. Matsui, H. Hibino, and H. Fukuyama, Japanese Journal of Applied Physics **58**, SIIA13 (2019).

[118] Y. Murata, M. Takamura, H. Kageshima, and H. Hibino, Physical Review B **87**, 165408 (2013).

[119] Y. Murata, T. Cavallucci, V. Tozzini, N. Pavliček, L. Gross, G. Meyer, M. Takamura, H. Hibino, F. Beltram, and S. Heun, Nano Research **11**, 864 (2018).

[120] C. E. Giusca, S. J. Spencer, A. G. Shard, R. Yakimova, and O. Kazakova, Carbon **69**, 221 (2014).

[121] D. Wong, Y. Wang, J. Jung, S. Pezzini, A. M. DaSilva, H.-Z. Tsai, H. S. Jung, R. Khajeh, Y. Kim, J. Lee, and S. Kahn, Physical Review B **92**, 155409 (2015).